UiT
THE ARCTIC
UNIVERSITY
OF NORWAY

Faculty of Science and Technology
Department of Physcics and Technology

On-chip optical nanoscopy: towards high throughput and multi-modality

—

Øystein Ivar Helle

A dissertation for the degree of Philosphiae Doctor - September 2019

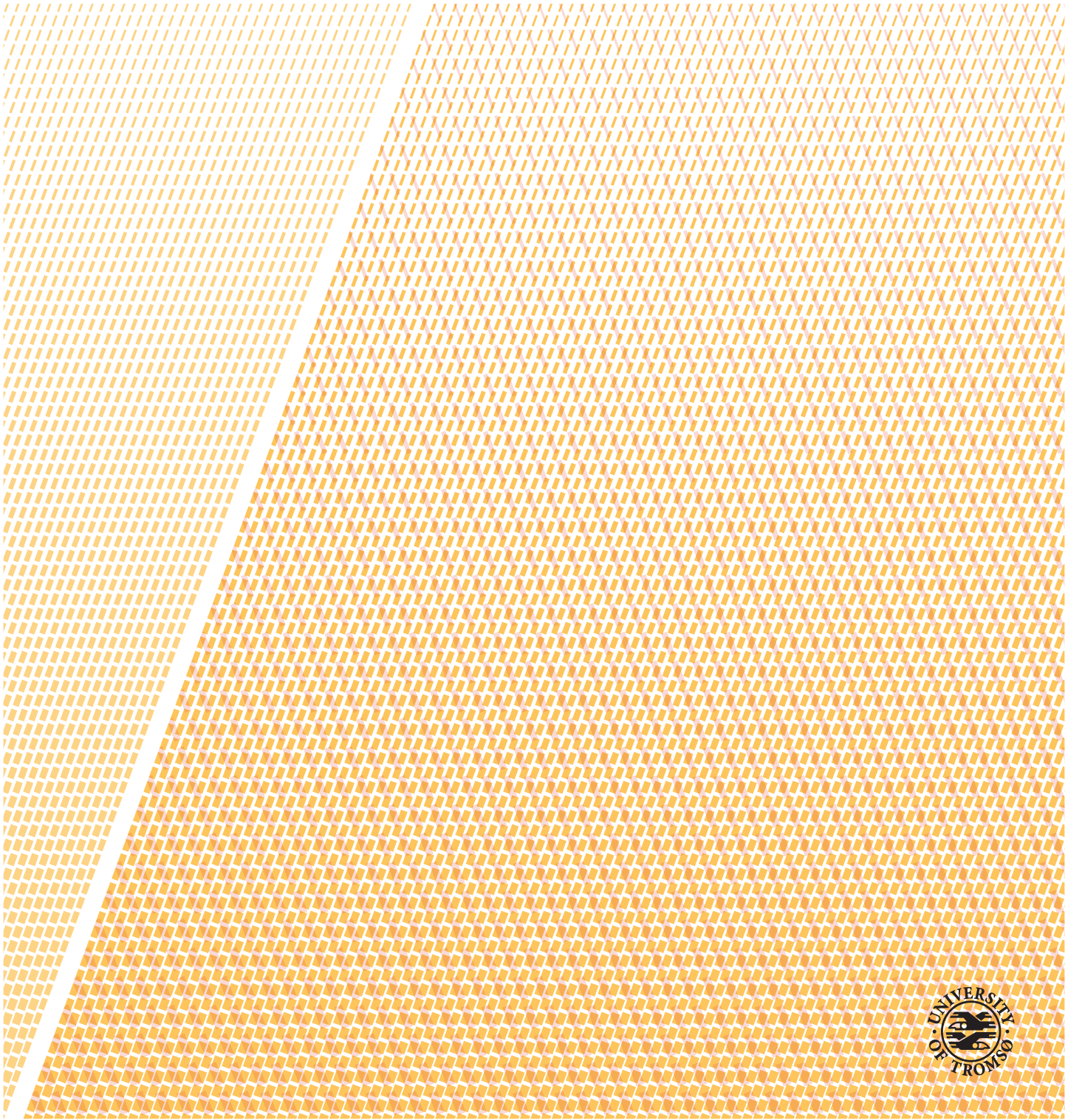

Abstract

Super-resolution microscopy techniques improve the resolution of the optical microscope beyond the diffraction limit of light. A range of different techniques demands different optical configurations and clever illuminating strategies to enhance the resolution. This has led to the development of advanced instrumentation, where the super-resolution mechanisms are adding both cost and bulk to the microscope. Furthermore, super-resolution microscopes are bound by high numerical aperture optics, which produce convincing images, but lack throughput. A common feature of most optical microscopes is the sample glass/coverglass arrangement used to mount samples before and during imaging. These have traditionally been neutral devices where the properties of the glass itself have mostly remained unused. In this thesis, a new direction in super-resolution imaging is introduced, where the sample glass/coverglass is replaced with a photonic integrated circuit chip. The chip supports the sample in the same way as the glass/coverglass, and by using optical waveguides at the chip surface, the chip illuminates the specimen via evanescent fields. By using high refractive index waveguides together with different geometries, the chip can produce the necessary illumination for a range of different super-resolution microscopy techniques. Furthermore, by exploiting the waveguide properties, several of the imaging methods are improved over their conventional implementations. This comes as a consequence of separating the excitation and collection light paths for super-resolution imaging. In this work, chip-based single-molecule localization microscopy is demonstrated with a 100 times increase in the field of view over conventional methods, and chip-based structured illumination microscopy is shown with a resolution beyond that of the objective-based implementation.

Acknowledgements

The work in this thesis was done under the supervision of Balpreet.S. Ahluwalia. I would like to thank him for giving me the chance, and for his dedication. I would also like to thank everyone that has been involved, all the collaborators, team members, technical staff, and all the members of the optics group at UiT.

Finally, I would like to thank my family, particularly my wife Tone and daughter Alva for all the love and support.

Contents

List of Figures

List of Abbreviations

CSIM Chip-based structured illumination microscopy

dSTORM direct stochastic optical reconstruction microscopy

ESI entropy based super-resolution imaging

FOV field-of-view

FRC Fourier ring correlation

FWHM full width at half maximum

HIC high index contrast

HiLO highly inclined laminated optical sheet

IEC Integrated electric circuits

LSEC liver sinusoidal endothelial cell

MMI multi-mode interference

MUSICAL Multiple signal classification algorithm

N.A. numerical aperture

OTF optical transfer function

PALM photo-activated localization microscopy

PBS phosphate buffered saline

PDMS Polydimethylsiloxane

PIC photonic integrated circuit

PSF point-spread function

ROI region of interest

Si_3N_4 silicon nitride

SIM structured illumination microscopy

SMLM single molecule localization microscopy

SNR signal to noise ratio

SOFI Super-resolution optical fluctuation imaging

STED stimulated emission depletion

Ta_2O_5 tantalum pentoxide

TE transverse electric

TIR total internal reflection

TIRF total internal reflection fluorescence

TIRF-SIM total internal reflection fluorescence structured illumination microscopy

TM transverse magnetic

UiT University of Tromsø

1

Background

Fluorescence microscopy is one of the most vital imaging techniques for laboratories working within life sciences. By using fluorescent markers, structures of interest can be imaged with high specificity, creating stunning images with selectivity to show even small-scale intra-cellular structures on a completely dark background. With the growing number of available probes and dyes, this technique is preferred for studying many biological phenomena, in both fixed and living samples. The labeling techniques used in fluorescence microscopy are capable of labeling structures with nano-scale dimensions, however, the obtainable resolution in a light microscope is hindered below 200-250 nm at the diffraction limit of light. For sub-cellular organelles, there is thus a vast resolution gap between what is labeled and the details observed in the microscope, which represents a problem in life sciences as many biological mechanisms have dimensions much smaller than the diffraction limit. Over the last two decades, a new range of techniques has emerged that aim to surpass the diffraction limit in light microscopy. Super-resolution optical microscopy techniques, commonly known as nanoscopy, are a collection of methods that use different tricks, including clever illumination strategies or photo-manipulation of fluorescent molecules, to achieve increased spatial resolution. Most methods heavily rely on shaping the excitation light thus forming a range of intensity profiles such as structured illumination, evanescent fields, intensity zeroes, or light sheets. In a conventional super-resolution microscope, beam shaping is traditionally achieved using free-space optics like lenses, phase/wave-plates, or diffraction gratings. The results are stunning detailed images, but at the cost of a complicated optical setup necessarily hosted in a stable and mechanically rigid

platform, which can be bulky, expensive and inherently prone to misalignment issues thus needing frequent maintenance. Moreover, the cost and complexity of the instrumentation is hindering the throughput of the techniques, with commercially available super-resolution microscopes lacking parallelization and offering small fields-of-view.

Optical nanoscopy is now moving towards extended throughput, increasing the amount of data acquired. At the same time, reducing the complexity of the instrumentation is another bottleneck that laboratories are working on. The main contribution of this thesis is to tackle optical nanoscopy in a slightly different way. By replacing the conventional glass slide as a sample substrate with an advanced photonic integrated circuit (PIC) chip, the excitation light shaping, steering, and delivery can be made on-chip, at the location of the sample by simply coupling light into the photonic chip integrated waveguides. The illumination is delivered to the specimen via an exponentially decaying evanescent field, and the technique is thus a two-dimensional method. Such a system will allow any standard low-cost microscope to be converted into a super-resolution fluorescence microscope, with minimal investment and effort. The chip-based imaging solution inherently has a much larger illuminated area than what is commercially available, which makes large field-of-view (FOV) TIRF super-resolution microscopy possible. With the option of choosing the collection optics, without altering the illumination, the technique allows for scalable fluorescence imaging. Furthermore, by using high index-contrast waveguide materials and on-chip shaping of the excitation light we extend the resolution currently possible for SIM.

1.1 Scope

This thesis covers the experimental realization of fluorescence microscopy and fluorescence super-resolution microscopy using a photonic chip to both hold and illuminate the specimen. Chip-based microscopy is a 2D technique, thus super-resolution in 3D is not covered here. Discussions about resolution within this thesis refer to lateral resolution unless otherwise stated. The waveguide chip production process is not within the scope of the thesis.

2

Introduction

To give the reader some common ground of understanding, in this chapter I will introduce some of the basic concepts laying the ground for the work presented in this thesis. First, the diffraction limit of light and its effect on the resolution of the microscope is introduced, followed by a discussion on the most fundamental super-resolution imaging techniques. Last, a brief introduction on integrated optical waveguides is presented.

2.1 The resolution of a microscope is bound by diffraction

A basic optical microscope is mainly composed of a few elements: a lamp and condenser lens to evenly illuminate the sample, a microscope objective lens to catch the light from the sample plane, and an eyepiece to observe the sample plane via the objective lens. A basic modern fluorescence microscope uses an infinity-corrected objective lens and an additional tube lens to focus light onto a camera. The key element in the microscope is the objective lens, which together with the tube lens (and possibly other magnifying elements) is responsible for the magnification of the system. Using lenses, a high magnification is possible. however, the resolution of the system is governed by the numerical aperture

(N.A.) of the objective lens, given by:

$$N.A. = n \sin(\theta), \tag{2.1}$$

where n is the refractive index of the immersion media and θ is the maximum angle of acceptance for light entering the objective lens. The values of n commonly range from $n_{air} = 1$ to $n_{oil} = 1.49$ (there is also a special oil meant for matching sapphire glass available having $n = 1.7$). The theoretical maximum value of $\theta = 90°$.

2.1.1 The diffraction limit

When light passes through an aperture it undergoes diffraction. For determining the resolution of a microscope, the key diffraction occurs when light passes through the objective lens. If we consider an infinitesimally small point source emitting at the sample plane, the circular aperture of the objective lens causes the detected emission, e.g. what is captured on the camera, to take the form of an Airy disk.

A simplified geometrical explanation of diffraction through the microscope objective lens can be found by observing a point source located in the sample plane as seen in Fig.2.1(a). Two points on the wavefront exiting the objective lens will constructively interfere in the center of the image, while away from the center the phase offset creates destructive interference thus giving rise to the Airy disk.

The size of the diffraction pattern (Fig.2.1(b)) is governed by the N.A. (2.1), which is bound by the optics and the immersion media. The highest N.A currently available is N.A=1.7. This implies that objects which are in reality smaller than the diffraction limit will be observed as having a size determined by the N.A. When the object is a point source, the intensity distribution image, which is commonly referred to as the point-spread function (PSF), describes the imaging capabilities of the system. The image formation in a microscope is thus described as the convolution with the PSF:

$$I(r) = (O(r)E(r)) * p(r), \tag{2.2}$$

where O(r) is the object, E(r) is the excitation light distribution and p(r) is the PSF. In three dimensions the PSF takes the form of an hourglass.

The limit of diffraction thus dictates the spatial resolution of the microscope, which can be measured as the closest distance two objects can come together [1]and still distinguish them as two objects. Different thresholds have been stated over time, with Lord Rayleigh's [2] resolution being the most conservative estimate. Rayleigh resolution considers two point sources as separated

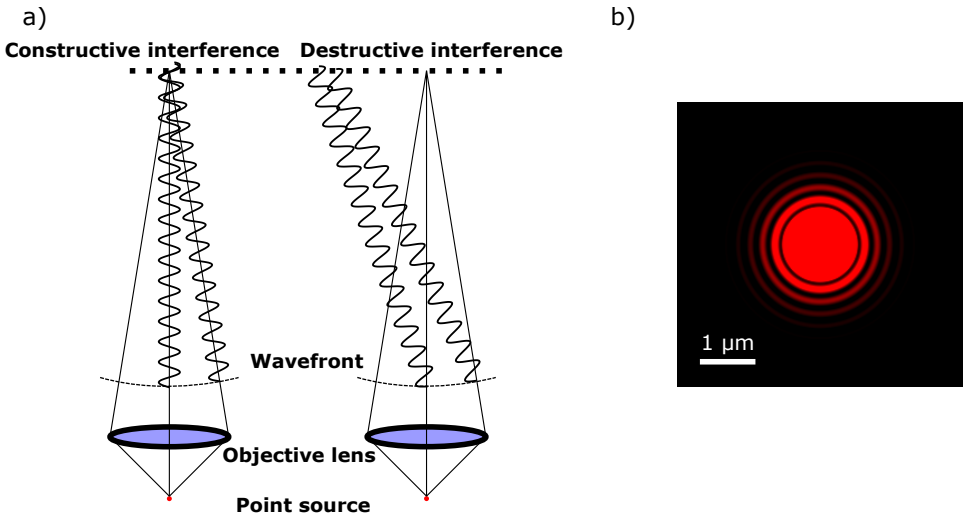

Figure 2.1: (a) When light is diffracted through a lens, most of the light is focused on the center of the image plane. In the periphery of the image plane, destructive interference causes a formation of an Airy pattern. (b) The size of the Airy disc is determined by the N.A. of the lens, where a high N.A. lens can focus the light to a smaller spot than a low N.A. lens.

when they can be observed as two points in a microscope, which is stated to happen when one of the intensity distribution's maximum is located in the first minimum of the other. The distance between the two points is then given by:

$$\Delta_{xy} = 0.61\frac{\lambda}{\text{N.A.}}, \tag{2.3}$$

where λ is the emission wavelength.

Ernst Abbe was the first to describe the diffraction limit of light [3]. Abbe's resolution limit is given by:

$$\Delta_{xy} = 0.5\frac{\lambda}{\text{N.A.}}. \tag{2.4}$$

With the advent of digital imaging and computer algorithms, the resolution could in theory be measured down below the Rayleigh and Abbe limits, and it is thus useful to define the distance where two point-sources are observed with a flat profile across the intensity distribution, given by the Sparrow resolution limit [4]:

$$\Delta_{xy} = 0.47\frac{\lambda}{\text{N.A.}}. \tag{2.5}$$

Figure 2.2 shows a simulation of two point-sources separated by the different resolution thresholds.

It can be seen from the above equations that the resolution of the microscope is limited by the wavelength of light and the numerical aperture of the objective lens. The diffraction limit is thus a fundamental lower limit, where the only way of having increased resolution would be to decrease the wavelength, or increase N.A..

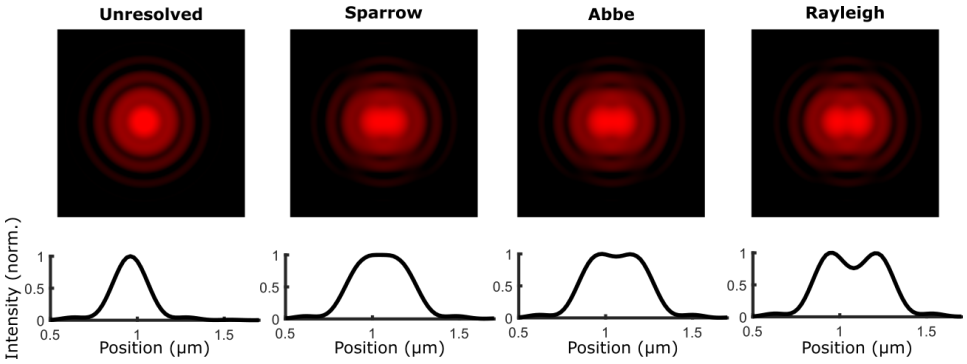

Figure 2.2: Two simulated point-sources are positioned at the different resolution limits from each other. The plots show a line drawn across the middle of each image. The Sparrow limit yields a flat line profile across the intensity distribution, and the two points are thus not observed to be separated. At both the Abbe and Rayleigh limits the two point-sources are clearly resolved. The imaging was simulated using N.A=1.4, with oil immersion n=1.5 and an emission wavelength of 610 nm.

Resolution in Fourier space

When discussing resolution, it can in some cases be useful to visualize the resolution in the Fourier domain. The Fourier transformation of the PSF is called the optical transfer function (OTF) and describes the spatial frequencies that are passed through on to the detector. The microscope objective effectively acts as a low pass filter, so information laying outside the cut-off, i.e the spread of the OTF, is not admitted through the objective lens. Figure 2.3 shows a simulated PSF and OTF, with the colorful rings indicating the cut-off frequencies as stated by Rayleigh, Abbe and Sparrow (i.e the Fourier versions of (2.3),(2.4), (2.5)).

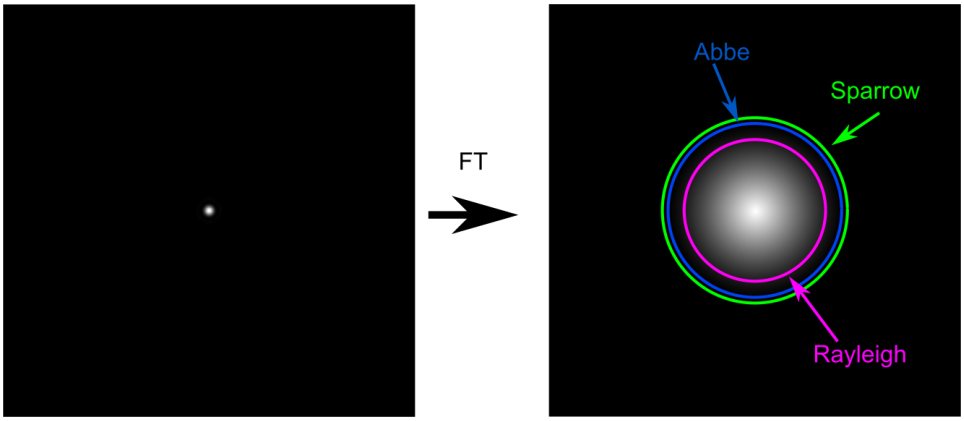

Figure 2.3: In the Fourier domain, the PSF is represented by the OTF. A green ring indicates the sparrow resolution limit, the blue ring indicates Abbe resolution and the magenta ring indicates the Rayleigh resolution limit.

2.2 Fluorescence microscopy

Fluorescence microscopy uses fluorescent molecules to visualize structures of interest at high specificity and exceptional contrast. Fluorescent molecules can be used for immunostaining of samples, i.e. having fluorescent molecules conjugated to a wide range of antibodies that bind to specific cellular structures. Alternatively, specimens can be genetically modified to produce their own fluorescent proteins at specific biological sites of interest, reducing or eliminating the need for staining. By using an emission filter to selectively block elastically-scattered light while transmitting the fluorescence signal, fluorescence microscopy thus allows the internal structures of cells to become visible on a dark background.

Explaining the mechanism of fluorescence is simplified with the use of a Jablonski diagram, which shows the electronic energy transitions of fluorescent molecules. Referring to Fig. 2.4, initially the fluorophore is residing in a dark state, in the lowest energy level S_0. If excitation light is introduced, the fluorophore can absorb a photon and the resulting increase in energy leads to an electron transition to a higher singlet state, e.g. S_1,S_2,S_N. The energy gaps between the higher-order states are smaller than the transitions between S_0 and S_1, and relaxation from the higher states to S_1 are more likely to release energy in the form of heat than the transition from S_1 to S_0. After internal relaxation, the fluorophores which are then residing in S_1 can spontaneously relax to the ground state by releasing a photon. This photon is red-shifted with respect to the absorbed photon, meaning that it has a longer wavelength, and can thus be imaged on a detector if the appropriate emission filters are installed in the microscope. The difference between the wavelengths of the absorbed

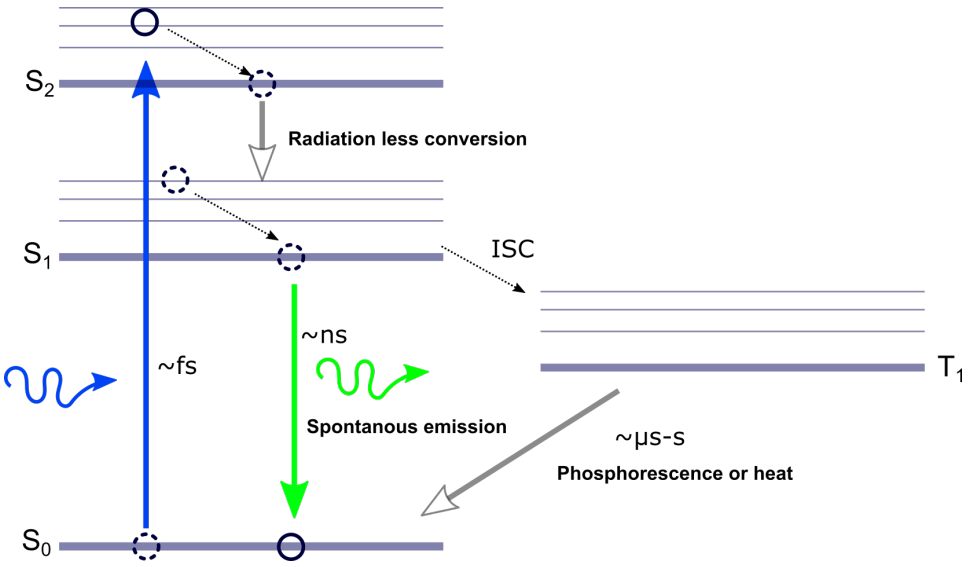

Figure 2.4: When blue excitation light is absorbed by the molecule, the energy increases and the electronic singlet state rises from S_0 to S_N. Following internal relaxation to S_1, the energy is released as the molecule relaxes to the ground state. This release may take the form of a red-shifted photon, which is the observed fluorescence. Alternatively, the molecule may enter a triplet state in which it can come back to the ground state without emission of a photon, or through the release of a photon in a different process called phosphorescence.

and spontaneously emitted photon is referred to as a Stokes shift.

The fluorophore can cycle between the first two states releasing photons or an inter-system crossing to the triplet state can occur. Here, several dark (off) states are possible, the most noticeable of which is photo-bleaching, which leaves the fluorophore in a permanent dark state. Common sources of excitation light for fluorescence microscopy are rather broadband Mercury lamps or more modern LED lamps, both in combination with excitation filters. However, due to the small stokes shift of many popular fluorophores, lasers are becoming more common due to their narrow frequency band and high intensity.

Although fluorescence microscopy has proven to be a very useful technique, the limit in resolution due to diffraction is hindering the study of many important biological problems. Rooted in fluorescence microscopy, a new branch of techniques has emerged, known as super-resolution microscopy, or nanoscopy, which seeks to overcome the limit of diffraction.

2.3 Super-resolution microscopy

Ever since the invention of the modern optical microscope some hundred years ago, the spatial resolution was believed to have a fundamental limitation set by the diffraction of light, limiting the resolution of the microscope to 200-250 nm laterally and 500-600 nm axially. However, in the decade between 1990 and 2000, a branch of methods which claimed to overcome the limitation of diffraction was described. With the understanding that the diffraction of light caused the fundamental lower limit for the resolution of the microscope, the search for super-resolution went away from the optics of the microscope and towards the chemistry of the fluorescent molecules. If the emission of photons from fluorophores within a diffraction-limited spot could be controlled in two states, the fluorescent on-state, and the fluorescent off-state (dark state), a sub-diffraction-limited image could be generated. By the simultaneous works of Hell [5], Betzig [6] and Moerner [7] these ideas were described and experimentally verified from the early 90s up until mid-2000s [8, 9, 10], and the three of them were jointly awarded the Nobel prize in chemistry in 2014 for this achievement.

Several different schemes have since been described which also achieve sub-diffraction-limited resolution. The scope of the thesis covers wide-field nanoscopy-on-chip incorporating a few of the available methods. A brief discussion of the most fundamental methods is included to provide a global overview, and the methods used in this thesis are described more thoroughly.

2.3.1 Super-resolution with intensity-zeros

One of the most well-known methods in optical nanoscopy is stimulated emission depletion (STED) microscopy [5, 8]. In STED, the off-state of the fluorophore is achieved by stimulated emission from the first singlet state using a modified confocal scanning microscope. Figure 2.5(a) shows the Jablonski diagram for STED microscopy. After the fluorophore is excited by the absorption of a photon, it will (after internal relaxation) return to the ground state and release a photon as discussed above. However, by adding a high intensity red-shifted laser striking the excited fluorophore still residing in S_1, the ground-state (which is an off-state) can be achieved through stimulated emission, rather than spontaneous emission. The transition to the ground state releases a photon that is coherent with the depletion laser and can thus be filtered out. This method is used in a confocal scanning microscope setting by overlaying the excitation light with a depletion laser having a hollow, doughnut-shaped intensity distribution as seen in Fig.2.5. In this manner, fluorophores away from the center undergo stimulated emission depletion, while in the center of the diffraction-limited spot the STED beam intensity goes towards

zero, and normal fluorescence occurs. Figure 2.5(b,c) depicts the effect without the depletion laser and with the depletion laser, respectively.

The spatial resolution of STED microscopy is governed by how close to the center of the diffraction-limited spot the depletion reaches. The resolution enhancement of STED can be stated by:

$$d_{STED} = \lambda/(2NA\sqrt{1 + (I/I_S)}), \tag{2.6}$$

where I is the maximum of the depletion laser intensity and I_S is the saturation intensity needed to reduce the probability of fluorescence emission by half, i.e a characteristic of the dye. Effectively the spatial resolution of STED microscopy is around 10-30 nm under optimized conditions. STED microscopy is a point scanning technique where, in the early implementations, the temporal resolution was technically limited by the method used for scanning. However, by using an electro-optical deflector [11], the scan speed could be increased to such an extent that the limiting factor for the temporal resolution became the pixel dwell time, which ultimately affects the image SNR. Thus, a full field of view was acquired over 1 ms, but to build contrast/SNR, the field of view was scanned many times (up to seconds for some structures). Another method showing live cell STED imaging utilized a resonant scanning mirror achieving 0.2 seconds temporal resolution [12]. However also here the field-of-view (FOV) is small, 8 x 12 μm^2. One implementation using thousands of parallel doughnuts has helped in increasing the field of view [13] available for STED.

2.3.2 Super-resolution with single-molecule localization

While the above-mentioned techniques rely on quenching the fluorescence in the periphery of a diffraction-limited spot in a scanning microscope configuration, a slightly different wide-field approach was first described, and experimentally verified by Betzig [6, 10] and Moerner [7, 14, 9]. If the number of active fluorescent molecules can be controlled such that only sparse, non-overlapping intensity distributions are detected, each of which originates from a single-molecule, the microscope image of the resulting intensity distribution, can be used to find the position of those molecules with high precision. To this end, the fluorescent molecules in the FOV of the objective lens can be switched on and off, and sub-sets of spatially separated molecules can be activated. This allows for their precise localization, and the reconstruction of a super-resolved image is possible based on the centroid position of individually located emitters. This is the fundamental idea governing methods collectively termed single molecule localization microscopy (SMLM), which is depicted in Fig. 2.6. These methods offer lateral resolution down towards 20-40 nm in cells, but at the significant cost of temporal resolution as one super-resolved image may include several thousand raw data frames of blinking molecules.

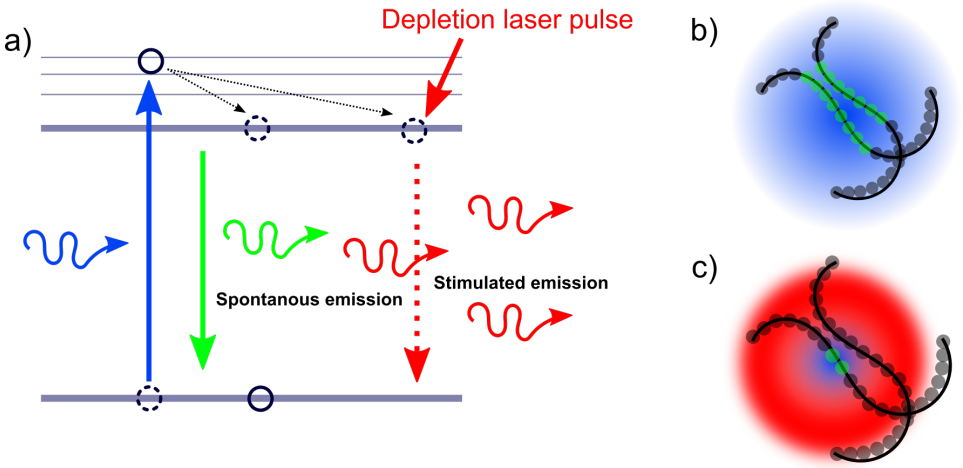

Figure 2.5: (a) A fluorophore is excited by the excitation laser to a higher-order singlet state. The ground state can be achieved by the spontaneous emission a photon, or by stimulated emission using a high-intensity depletion laser. (b) A diffraction-limited point scanning spot without the use of a depletion laser activates all molecules within the spot. (c) Applying the depletion laser with a doughnut shape depletes the fluorescence in the periphery of the spot, but not in the center, where normal fluorescence occurs.

Several methods have been developed to achieve the necessary on/off switching of fluorophores for SMLM. Stochastic optical reconstruction microscopy (STORM) [15] uses a single-molecule switch, which can be photo-switched between on and of states by laser light of two different wavelengths. The single-molecule switch reported in [15] used the two cyanine dyes Cy3 and Cy5, where photo-switching of Cy5 was reported to be much more efficient if a Cy3 molecule was nearby. Another technique, photo-activated localization microscopy (PALM) [10, 16], uses photo-activated fluorescent proteins which can be activated by the absorption of a 405 nm photon, and which relies on photobleaching to achieve the necessary off-state. The fluorescent proteins can be used to genetically modify biological materials to express fluorescence at pre-determined structures.

2.3.3 direct stochastic optical reconstruction microscopy (dSTORM)

While these methods have been used to achieve a resolution approaching molecular levels, the need for dedicated activation lasers and specialized labels complicates the experiments and thus limits their widespread use. To combat these issues, many common fluorophores can be used for SMLM by harnessing the natural states of the fluorescent phenomenon. Fluorescence is achieved

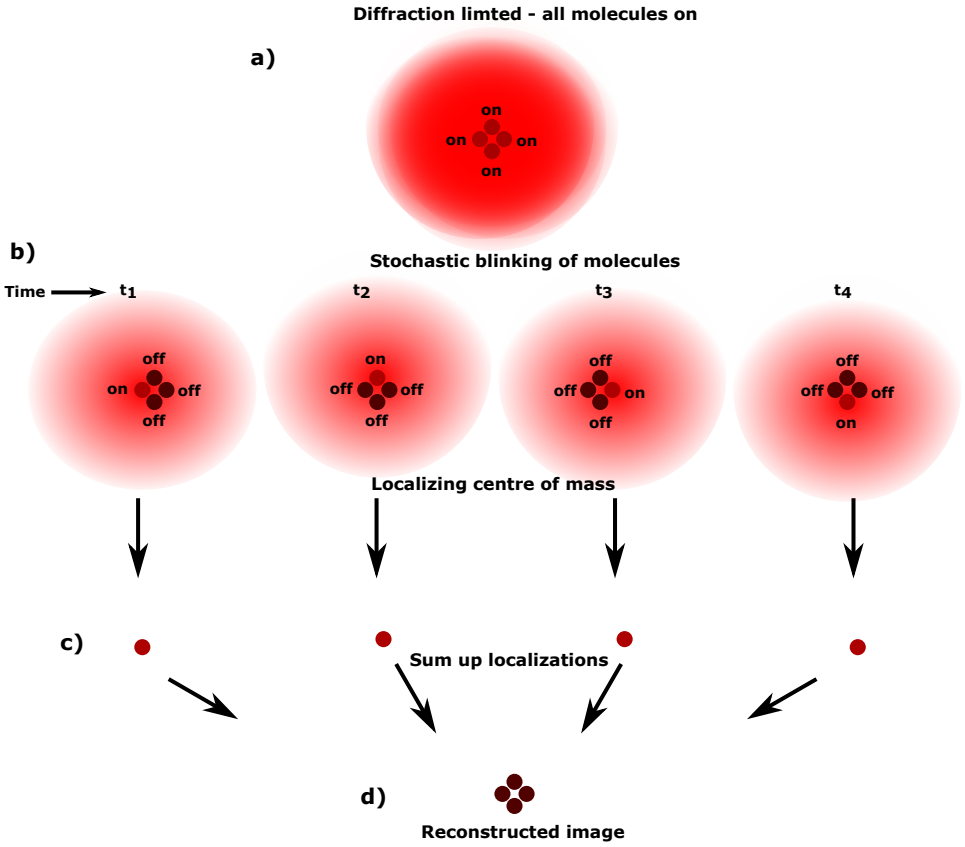

Figure 2.6: Principle of SMLM imaging. (a) If all molecules within a diffraction-limited spot are emitting fluorescence simultaneously they can not be individually localized. (b) With the loss of temporal resolution, some molecules can be brought into a dark state, while others are allowed to emit fluorescence. (c) With the assumption that the detected fluorescence originates from a single-molecule, the localization of the molecule can be found with high precision. (d) A new, super-resolved image can then be built from the list of all of the measured center coordinates.

by circulating between the ground state S_0 and first single state S_1, but fluorophores may also undergo an inter-system crossing thereby populating the first triplet state (T1), with typical transition probabilities around 0.1% [17]. The triplet state represents a fluorescent off-state, with lifetimes on the order of microseconds to milliseconds [18]. Molecules populating the T1 state may return to S_0 or enter even longer-lived dark states. This was harnessed for SMLM, and was simultaneously published as ground state depletion followed by individual molecule return (GDSIM) [17] and as dSTORM [19].

In dSTORM, the on-off switching is achieved by using high intensity laser excitation light and chemical reduction off molecules in the triplet state. The intensity of the excitation light can be used to control the number of emitters residing in T_1, and high intensities up to kW/cm^2 are beneficial for reducing the number of fluorescing emitters, ideally reaching up to 30-50 kW/cm^2 [20]. By removing the oxygen in the sample buffering media, the triplet state lifetime is prolonged since oxygen is known to be an efficient triplet state quencher [21]. Furthermore, a reducing agent is added to chemically reduce the triplet state, which happens when an electron is absorbed from the image buffer by the fluorophores. The reduced triplet state, also known as the radical anion state, is a fluorescent off-state and is very long-lived. The return to S_0 can happen spontaneously [22] with the absorption of oxygen, or with the optional help by stimulating the sample with light with a wavelength around 500 nm [23]. A common buffer, working well with the commonly-used fluorophores Alexa Fluor (AF) 647 and AF 488 , uses an enzymatic oxygen scavenging system made from glucose with the enzymes glucose oxidase and catalase in phosphate buffered saline (PBS) at a pH of approximately 7.5. The buffer is supplemented with millimolar concentrations of a reducing thiol, most commonly β-mercaptoethylamine (MEA) or β-mercaptoethanol (BME).

Image reconstruction of SMLM data

In dSTORM and other SMLM techniques, the sample is brought into a blinking state, where the number of active emitters at any given time is sparse enough to allow for their individual localization, as depicted in Fig. 2.6. In this way, the molecules can be localized in time to build up a reconstructed image consisting of the centroid positions of all the detected fluorescent molecules. One dSTORM reconstruction thus consists of several thousands of individual images of emitter distributions. A detailed protocol on how to acquire and reconstruct dSTORM images can be found in the literature [20, 24].

The resolution enhancement of SMLM is governed by the number of photons collected from the single-molecule event and the noise contribution from the background, which includes Poisson noise and shot noise. The resolution is

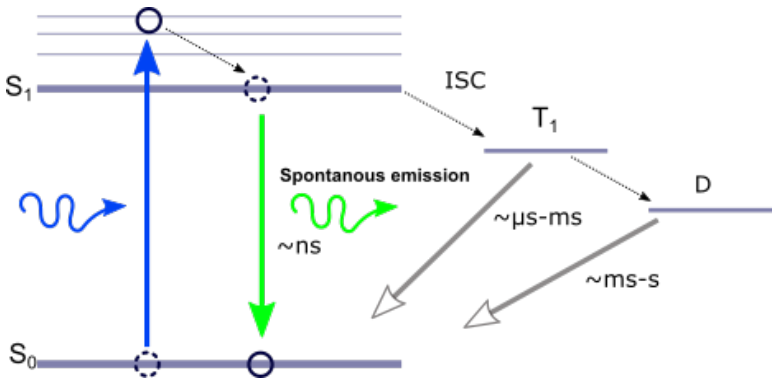

Figure 2.7: Simplified Jablonski diagram showing the on/off switching concepts of GDSIM and dSTORM. A fluorophore cycle naturally between the first two singlet states, but a transition to the triplet state may occur. This is a longer-lived dark-state, with a further probability of entering other dark states, which may have longer lifetimes.

proportional to the localization precision, given by Thompson et.al [25] as:

$$\sigma_x = \sqrt{\frac{s^2}{N} + \frac{\frac{a^2}{12}}{N} + \frac{8\pi s^4 b^2}{a^2 N^2}}, \tag{2.7}$$

where s is the standard deviation of the 2D Gaussian fit, N is the number of detected photons from one molecule, a is the pixel size, and b is the standard deviation of the background (including background fluorescence emission combined with detector noise).

A vast number of software packages have been released over the last years for the reconstruction of SMLM data, and many have been released for use with the open-source image processing platform ImageJ [26]. In this work, we used the open-source reconstruction software Thunderstorm [27], which was available as a Fiji plugin.

Suitable fluorescent molecules for dSTORM should obey two key requirements [28]. First, it is desirable to have a high photon count, since the resolution of SMLM scales with an inverse-square-root dependence (2.7) on the number of photons collected from a single-molecule blinking event. Second, the number of active emitters at each time is desired to be controlled such that the chance of overlapping emitters within a diffraction-limited spot is reduced. Furthermore, the labeling density of the structure must be kept within the Nyquist sampling limit for the emitter density, discussed in [29]. However, an oversampling of at least 5 times was suggested [30] to accurately reconstruct dense structures.

Recently a new method, DNA Points Accumulation for Imaging in Nanoscale Topography (DNA-PAINT) [31], has emerged, where the cause of the blinking events is moved away from energy transitions in the fluorophore, and shifted towards binding and unbinding events of freely-floating, fluorescently labeled DNA strands (image strands). The fluorophore can be localized to a high precision while the image strand is immobilized through temporary binding to a complementary DNA docking strand, which is attached to the structure of interest. In this manner, the fluorophore could potentially yield a brighter signal giving increased resolution over the other SMLM methods. The increased signal is due to less chance of T1 build-up, and controlled docking times allowing for the molecule to fluoresce at the given position over a longer time. Furthermore, the intensity needed for DNA Paint is lower than dSTORM since the blinking is achieved without the need for triplet state shelving.

Experimental setup for dSTORM

A simple microscope configuration for dSTORM (and other SMLM techniques) is an inverted microscope equipped with a high N.A. objective lens and a sensitive camera, either EMCCD or sCMOS (Fig.2.8). Laser excitation light is sent into the microscope via a dichroic mirror that directs the light onto the objective lens. Two lenses, L_1 and L_2, can be used to focus the light on to the back aperture of the objective lens to generate the different light patterns discussed below. The excitation light path described here is tightly linked to the collection light path, and a high N.A objective lens is used for both exciting the sample and collecting the emitted signal, which gives a high resolution. However, the FOV is limited due to the same reason.

The laser excitation light can be focused in the center of the back aperture of the objective lens yielding a collimated output, referred to as EPI-excitation (Fig.2.8(b)). This will excite fluorescence along the beam path through the entire sample axially, which could lead to high background signal and thus reducing the achievable resolution in the dSTORM image reconstruction. This is particularly a problem within SMLM due to the low light levels that are detected when looking at single-molecules.

To combat the problem of high background, researchers are using total internal reflection fluorescence (TIRF) excitation of the fluorescent molecules. Here, the excitation light is focused on the periphery of the back aperture of a high N.A. TIRF objective lens, such that the light is total internal reflected at the coverglass/sample boundary (Fig. 2.8(c)). This creates an evanescent field exponentially decaying to an effective excitation depth of around 150 nm in the sample. This method has low out-of-focus blur due to the thin section of the sample that is illuminated. TIRF excitation is an inherently 2D technique,

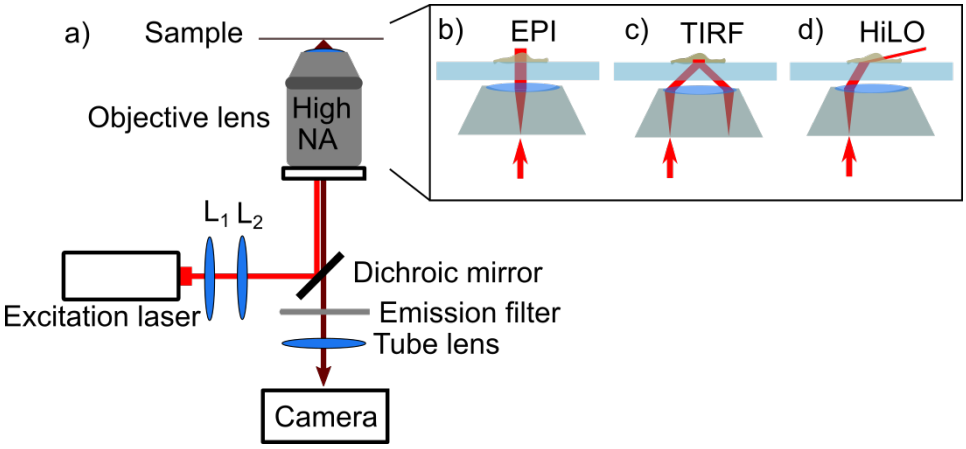

Figure 2.8: (a) The experimental setup for conventional SMLM relies on an inverted setup using the same high N.A objective lens for both excitation and collection. (b) The light can be collimated through the objective in EPI-fluorescence mode. (c) By using a TIRF objective, evanescent field excitation can be achieved with very good optical sectioning, although this results in decreased power density. (d) A compromise between EPI and TIRF can be achieved using highly inclined laminated optical sheet (HiLO) illumination, which excites fluorescence to a depth of around 10 μm.

mostly suited for studying mechanisms at the periphery of the cell near the membrane.

The ability to image deeper without sacrificing the signal to noise ratio (SNR) would thus be beneficial. For this purpose a HiLO [32] (Fig. 2.8(d)) can be used to illuminate the sample. HiLO is achieved by using a TIRF objective lens, and focusing the excitation light in the periphery of the back aperture, but taking care to not reach the angle of total internal reflection. The HiLO light is refracted at the coverglass interface, which results in an inclined ray of light penetrating the sample. The axial reach of the light is around 10 μm. This method maintains some of the high intensity of EPI-excitation but reduces the out-of-focus background due to the inclined excitation light profile. The signal to background ratio achieved using HiLo yields up to eightfold improvement over EPI-excitation [32].

2.3.4 Intensity fluctuation-based methods

Although the above-mentioned methods give extraordinary spatial resolution, the temporal resolution is reduced substantially. In STED, the temporal resolution is decreased when imaging large areas due to the scanning nature of the method, while localization microscopy is inherently slow due to the reconstruction algorithms and the need for a sparse emitter density. One method

has attempted to alleviate this problem by algorithmic means [33], but user adoption of this technique has remained low. The low temporal resolution has driven the need for another group of methods which do not demand separated blinking emitters. Fluctuation-based techniques utilize statistical properties to reconstruct super-resolved images from intensity-fluctuating data. Here, many fluorophores can be emitting within a diffraction-limited spot such that their intensity distributions are overlapping, but with the necessary criteria that the emitted fluorescence is fluctuating in intensity. The fluctuations can be achieved either using fluctuating fluorophores (e.g from blinking and bleaching or quantum dots), or by fluctuating the pattern of the excitation light. The reconstruction of this type of data measures statistical differences on a pixel-to-pixel basis. Super-resolution optical fluctuation imaging (SOFI) [34] uses the calculation of cumulants in a time series to increase resolution. entropy based super-resolution imaging (ESI) [35] calculates entropy and cross-entropy values in a time series stack. Multiple signal classification algorithm (MUSICAL) [36] harnesses the eigenimages in the time series. Although initially, these methods relied on the statistical fluctuation of individual fluorophores, it has been shown to work with stable fluorophores excited with speckled light [37]. In this sense, the fluorescence response is fluctuating due to the randomly changing speckled excitation light, which in [37] was achieved using multi-mode speckles from a fiber. Using this idea, the demand for inducing random fluctuations in the sample is reduced, and this technique should then work with most bright fluorophores.

The fluctuation-based methods do offer resolution enhancement, however not as good as the more brute-force methods like SMLM and STED. However, the temporal resolution is greatly improved as only tens to hundreds of image frames are needed for these approaches to work. Furthermore, with the reduced laser intensity needed to induce fluctuations in the sample, problems with photo-toxicity are also diminished. On the other hand, these methods lack widespread impact, possibly due to the large degree of non-linear intensity amplification in the reconstructed images. For biological questions to be answered, a super-resolution image should ideally be a linear representation of the ground truth, and with minimal or no reconstruction artifacts.

2.3.5 Super-resolution with structured illumination

The fluctuation-based methods somewhat improved the temporal resolution of optical nanoscopy, but still a few hundred frames of data are needed to generate a super-resolved image. One method that also has had a commercial impact is structured illumination microscopy (SIM) [38, 39]. This method offers limited resolution enhancement but at imaging speeds suitable for live-cell imaging. Here, only 9 or 15 images are needed to reconstruct one super-

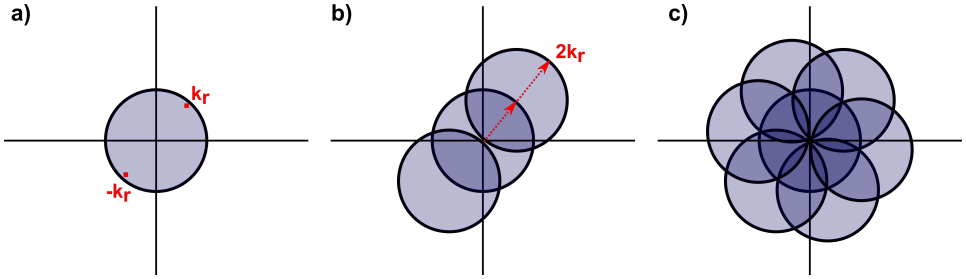

Figure 2.9: SIM imaging is depicted in frequency space. (a) The OTF of the microscope objective is shown. The frequencies accepted by the objective are laying inside the circle. The red dots mark the frequency of the structured illumination. (b) After the reconstruction, the OTF is extended with two new copies, one centered at k_r and one at $-k_r$, with the new image resolution being $2k_r$. (c) To have an isotropic resolution the SIM pattern is rotated and the process is repeated three times to fill the frequency space.

resolved image in 2D or 3D, respectively. Besides, the method needs illumination intensities comparable to diffraction-limited imaging (w/cm^2), which reduces photo-toxicity and bleaching.

SIM is a technique that harnesses structured light to down-convert unresolved frequency content and thus extends the reach of the OTF up to an amount determined by the frequency of the structured light. The approach can be loosely described by looking at the image function. The microscope image I(r) can be described as

$$I(r) = (O(r)E(r)) * p(r),$$

where the object $O(r)$ positioned at r is multiplied with the illumination $E(r)$ and the product is observed through the objective lens via convolution of the point spread function $p(r)$. If E(r) represents planar illumination the image will be that of a conventional, diffraction-limited fluorescence microscope. Contrarily, let $E(r)$ be a sinusoidal illumination pattern such that:

$$E(r) = 1 + \cos(k_r r + \phi), \tag{2.8}$$

where k_r is the spatial frequency of the illumination pattern and ϕ the phase, which gives

$$I(r) = (O(r)(1 + \cos(k_r r + \phi)) * p(r). \tag{2.9}$$

Here, the image detected at the camera will show the modulation caused by the product of $O(r)$ and $E(r)$ as a formation of Moirè fringes. If we study the image function in Fourier space we can have a clearer view of the frequency mixing which happens using structured illumination. Via the Fourier transform, we can write the image function with structured illumination 2.9 as

$$\hat{I}(k) = \hat{O}(k) * [\delta(k) + \frac{m}{2}e^{i\phi}\delta(k - k_r) + \frac{m}{2}e^{-i\phi}\delta(k + k_r)]\hat{p}(k),$$

where we have used Euler's relation and introduced a modulation factor m of the structured illumination. Performing the convolution we observe three copies of the object function:

$$\hat{I}(k) = [\hat{O}(k) + \hat{O}(k - k_r)\frac{m}{2}e^{i\phi} + \hat{O}(k + k_r)\frac{m}{2}e^{-i\phi}]\hat{p}(k), \tag{2.10}$$

located at k, $k - k_r$ and $k + k_r$. In this equation, we see that frequency content having spatial frequencies up to $k_{SIM} = |k + k_r|$ is mixed into the image acquired using structured illumination. Figure 2.9 depicts SIM imaging in Fourier space. Figure 2.9(a) shows the diffraction-limited OTF, where higher spatial frequencies are located away from the center. The ring indicates the OTF cutoff, and the red dots mark the spatial frequency of the structured illumination k_r. By the solution of 2.10 the mixed frequencies can be shifted back to their correct positions, which correspond to the OTF being positioned at $k - k_r$ and $k + k_r$, as shown in Fig. 2.9(b). The resolution is then increased by a maximum factor of 2, due to the structured illumination being generated via the objective lens and thus being diffraction-limited. To get isotropic resolution enhancement, the SIM pattern is rotated three times and the process repeated. The solution to (2.10) can be acquired if we consider that there are three unknowns, ($\hat{O}(k)$, $\hat{O}(k - k_r)$ and $\hat{O}(k + k_r)$. Thus we need three equations to solve it, which is done by shifting the phase of the SIM pattern three times. This implies taking a total of 9 images for one 2D SIM image, 3 images with different phases for each orientation of the SIM pattern. SIM can also be performed in 3D, which would need 3 interfering beams and a total of 15 images.

The 2D SIM imaging process in real space is depicted in Fig. 2.10, where Fig. 2.10(a) shows the object. For comparison, a diffraction-limited image (Fig. 2.10(c)) is acquired by the multiplication with planar illumination (2.10(b)) convolved with the PSF. For the SIM image, the object is multiplied with the structured light(Fig. 2.10(d-f)), which yields 9 images of a Moirè pattern (Fig. 2.10(g-f)). The SIM reconstruction is shown in Fig. 2.10(j).

2.3.6 Resolution of SIM

By using the Abbe limit (2.4) as the cutoff for the OTF support, the highest spatial frequencies accepted by the objective lens are given by:

$$k_{diff.lim} = \frac{2NA}{\lambda}, \tag{2.11}$$

while for SIM the extent of the OTF is increased up to twice the Abbe limit

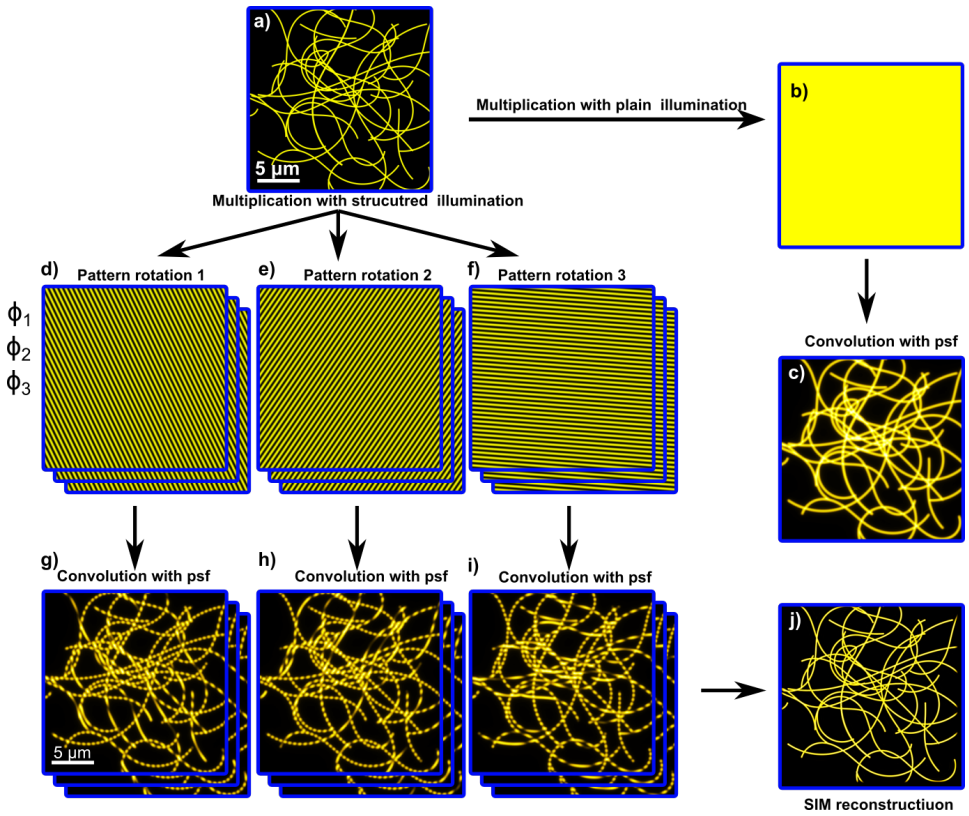

Figure 2.10: (a-c) In a diffraction-limited fluorescence image, the detected image can be described as the multiplication of the object with planar illumination, and the diffraction-limited image is formed via the convolution of the objective lens. (d-j) SIM imaging can be described similarly. The object is multiplied with structured illumination with three rotational angles of the SIM pattern, and three phase-steps for each rotational angle. The nine resulting diffraction-limited images (g-i) express Moirè fringes due to the structured illumination. The SIM reconstruction (j) yields an image with improved resolution over the diffraction-limited image (c).

(Fig.2.9(b,c)):

$$k_{SIM} = \frac{4NA}{\lambda} = 2k_{diff.lim}. \tag{2.12}$$

As can be seen from (2.11) and (2.12), the maximum resolution enhancement of SIM is 2x the diffraction-limited resolution. Several methods have worked towards increasing the resolution of SIM. Plasmonic SIM [40, 41] utilizes surface-enhanced plasmons to achieve reduced fringe spacing and thus increased resolution. Another method, non-linear SIM [42], provides 50 nm resolution by depletion of the fluorophore combined with structured illumination. These methods come at the cost of photo-toxicity, compatibility with dyes and ease of use. By the combination of TIRF and SIM (total internal reflection fluorescence structured illumination microscopy (TIRF-SIM)), the resolution of SIM can be pushed below 100 nm when using high numerical aperture TIRF lenses [43, 39, 44].

2.3.7 Summary of nanoscopy techniques

A wide range of nanoscopy techniques have been developed over the last two decades, and attempting to choose a "best" method is difficult. It is perhaps more viable to choose the imaging method based on the application. The nanoscopy methods differ in their illumination schemes, types of dyes available, achievable resolution and live cell compatibility. Although some very useful instruments have been released over the last years, the price and the lack of throughput combined have kept the wide-spread penetration of the methods slow.

Here, we propose a method to acquire TIRF nanoscopy images using photonic integrated circuits, which comes with the possibility of being retrofitted onto the most basic microscope configuration, offering a TIRF nanoscopy platform at an affordable price, without sacrificing the image quality. It further adds the possibility of multi-modal TIRF nanoscopy using different imaging techniques. Using waveguide-based illumination, large areas can be illuminated for high-throughput nanoscopic imaging, e.g by increasing the FOV for dSTORM by 100 times over the conventional approach

2.4 Integrated photonics

Integrated electric circuits (IEC) have played a vital role in the evolution of today's technologies. From computers and smartphones to the electric piano in your living room, information is digitized and processed using IEC devices consisting of transistors, resistors, amplifiers and more. However, IEC rely on the flow of electrons through a conductive material like copper. When

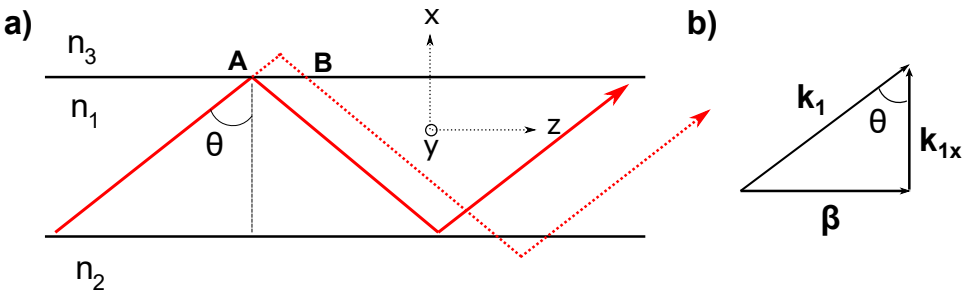

Figure 2.11: (a) Geometric explanation of light guided in an asymmetric slab waveguide with refractive indices $n_3 < n_2 < n_1$. The light (red arrows) is confined in the x-direction, and propagating towards z. When the light is reflected at the interface between the different materials, a lateral displacement (e.g between A and B) of the reflected light is observed due to the Goos-Häncen shift (which is attributed to the evanescent field formation), and the reflected light takes the dotted path out from the interface. (b) The wavevector k points along the wavefront and can be decomposed to give the transverse and longitudinal propagation constants.

the sub-atomic electrons travel in a conducting wire, interactions with other particles will occur. This resistance to the flow of electrons causes the amount of information that can be transmitted on the electric circuit to be limited, and energy to be lost as heat.

On the other hand, a photonic integrated circuit (PIC) uses photons to transmit information. Photons are mass-less quanta of light traveling at the speed of light, and have little interaction with other photons to slow them down. The bandwidth of a PIC is thus greatly enlarged over the electric counterpart, and due to low-loss optical guiding, these devices offer better power efficiency. The fundamental component of a PIC is the dielectric waveguide. The waveguide is the analog of the copper wire in the IEC, and is responsible for the propagation of photons from A to B.

2.4.1 Confining light by total internal reflection

Apart from the ability to transmit large amounts of data, the presence of evanescent fields on the outside of waveguides open for a different exploitation of PICs.

When light is introduced into a medium of a higher refractive index than the surrounding medium, it can be guided by total internal reflection. In Fig. 2.11(a), an asymmetric waveguide is depicted which corresponds to light being guided in medium 1, with refractive index n_1, and where $n_3 < n_2 < n_1$. In this situation, the light is only confined along the x-direction.

If we consider Snell's law of reflection on the boundaries of the structure depicted in Fig. 2.11(a), we find the critical angles to be:

$$\theta_{c2} = \sin^{-1}\left(\frac{n_2}{n_1}\right) \quad \text{and} \quad \theta_{c3} = \sin^{-1}\left(\frac{n_3}{n_1}\right)$$

where $\theta_{c2} > \theta_{c3}$ when $n_3 < n_2$. If the angle of incidence towards the two materials is larger than the critical angles, i.e $\theta > \theta_{c2} > \theta_{c3}$, the wave undergoes total internal reflection and is thus confined to the waveguide core.

The wave vector in material 1, k_1 is pointing in the direction of the wavefront, and can be decomposed as shown in Fig. 2.11(b). The two components are:

$$k_{1x} = k_1 \cos\theta \quad \text{and} \quad \beta = k_1 \sin\theta$$

where the wavenumber can be written as $k_1 = k_0 n_1$. The longitudinal propagation constant can be written as:

$$\beta = k_0 n_1 \sin\theta,$$

where $k_0 = \frac{2\pi}{\lambda}$ is the free-space wavenumber. It is useful to define the effective refractive index of the waveguide:

$$n_f = n_1 \sin\theta, \tag{2.13}$$

where $n_f = \frac{\beta}{k_0}$.

For the trapped light to propagate in the waveguide, the reflected wave must constructively interfere with itself to be self-consistent (i.e to not die out). This implies that the total phase shift that the wave experiences over a round-trip (bouncing at 2 boundaries) must be an integer multiple of 2π. If the waveguide core thickness is d, the phase change for one complete round-trip is $2dk_{1x} = 2dk_1 \cos(\theta)$.

Moreover, when a beam of finite size is total internal reflected at the boundaries it will experience an additional phase shift $\Phi(\theta)$. This phase shift is related to the wave interaction time with the boundary, and the consequence is that the light striking the boundary at point A in Fig.2.11(a) takes the dotted path B after the reflection. This is known as the Goos-Häncen effect, which can be visualized as the reflection point being shifted out of the waveguide core, as

seen in the figure. Thus, for the guided wave to be self-consistent we have that the total phase change must obey:

$$2k_1 d\cos(\theta) + \Phi_2(\theta) + \Phi_3(\theta) = 2m\pi, \tag{2.14}$$

where $m = 0, 1, 2...$ is an integer. $\Phi_2(\theta)$ and $\Phi_3(\theta)$ are the phase shifts related to the Goos-Häncen effect, which are dependent on the polarization state of the light. There thus exists a discrete set of solutions of (2.14) for each of the two polarization states, transverse electric (TE) and transverse magnetic (TM). These solutions are referred to as waveguide modes with mode number m.

The outcome of (2.14) is that for every m, there is an associated β_m, and thus n_{fm}, where $n_{f0} > n_{f1} > n_{f02}...$ When $m = 0$, the mode is called the fundamental mode. Waveguides only supporting the fundamental mode are termed singlemode waveguides. For $m > 0$ there is more than one solution to (2.14), and the waveguide is multimode.

Evanescent field

Owing to the Goos-Häncen effect, the wave appears to have its point of reflection a distance away from the waveguide core, inside the materials of lower refractive index. There is thus a corresponding wave vector k_i with propagation constant β_m outside the waveguide core. By the same trigonometry as shown in Fig. 2.11(b) we can write it as

$$k_i^2 = \alpha_i^2 + \beta^2$$

where α_i is the transverse propagation constant in materials 2 and 3 (i.e $i = 2, 3$) surrounding the waveguide core. By dividing the equation with k_0^2 and rearranging it we have that:

$$\alpha_i = k_0\sqrt{n_f^2 - n_1^2}, \tag{2.15}$$

which is often referred to as the attenuation coefficient. The light that is present in materials 2 and 3 experience an exponential decay where the penetration

depth d is given by:

$$d_i = \frac{1}{\alpha_i} = \frac{1}{k_0\sqrt{n_f^2 - n_i^2}}, \tag{2.16}$$

where $i = 1, 2$ for material 1 and 2, respectively. The exponentially decaying field outside the waveguide core is called the evanescent field.

In a waveguide, light is guided by total internal reflection. When light is totally reflected at a refractive index boundary it gives an evanescent wave. Many on-chip integrated optics technologies rely on harnessing these evanescent fields, which is also the case for the technology presented in this thesis. The evanescent field formation in dielectric waveguides is briefly described here, while a full theoretical explanation can be found in literature [45, 46, 47].

3

Chip-based microscopy

3.1 Introduction

TIRF microscopy [48] is a technique that illuminates the sample with an exponentially decaying evanescent wave originating from a total internal reflection between a high and low refractive index material (Fig.2.11). In TIRF microscopy the penetration depth is typically around 100-200 nm (2.16), which is substantially smaller than what can be achieved using an objective lens; i.e the focal depth of a high N.A.(N.A.=1.4) objective lens is around 500 nm. TIRF microscopy thus provides an exceptional signal-to-noise ratio owing to the thin optical sectioning that is achieved using evanescent fields to excite fluorescence. This dramatically reduces the out-of-focus blur, as can be seen in Fig.3.1 where a cell (liver sinusoidal endothelial cell (LSEC)) is imaged under both EPI-illumination and TIRF. TIRF microscopy has found broad application within life science for studying different biological mechanisms, e.g. receptors at the cell membrane [49, 50], exocytosis [51, 52] or cell-substrate interactions [53]. Traditional implementations of TIRF microscopy includes prism-based TIRF and objective-based TIRF. In prism TIRF (Fig.3.2(a)), a prism is used to direct light towards the coverglass/sample boundary, thus reaching the angle of incidence needed for total internal reflection. Prism-based systems are fairly easy to set up and can be used in both upright and inverted microscope setups. However, the commercial impact of TIRF microscopy came with objective-based TIRF (Fig.3.2(b)). Here, a high N.A objective lens ensures the angle of incidence needed for TIRF at the coverglass/sample boundary. Objective-based TIRF benefits from easily changing between TIRF, HILO and EPI-illumination

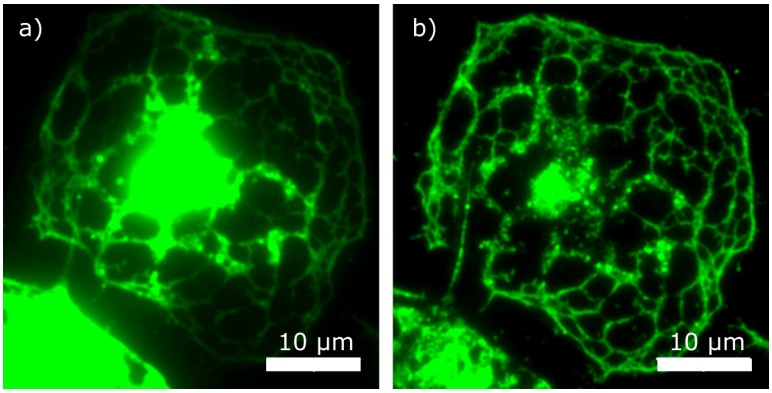

Figure 3.1: (a) EPI-fluorescence microscopy sends the excitation light straight through the sample, causing out-of-focus blur. (b) TIRF microscopy provides excellent optical sectioning with high SNR, here shown using chip-based TIRF illumination (tantalum pentoxide (Ta_2O_5) strip waveguide, width=60 μm). The sample is a LSEC stained with Cellmask Orange plasma membrane stain.

by shifting the laser beam position on the back aperture of the objective lens (Fig. 2.8). Another way of performing TIRF microscopy is using planar on-chip waveguides (Fig.3.2(c)). First reported in [54] and later in [55, 56, 57], chip-based TIRF illumination offers evanescent field excitation over pre-determined paths. Light is coupled into a chip and guided in planar optical waveguides by total internal reflection (Fig. 2.11, Fig. 3.2(c)). The result is an evanescent field present on the surface of the entire waveguide layout. An easy way to achieve this kind of illumination is to use the coverglass itself as a waveguide, coupling light into the coverglass side facet [58]. However, to achieve a high evanescent field intensity, shallow waveguides of a high refractive index material are required, which especially becomes important when moving towards super-resolution imaging techniques, where some techniques require intensities in the range of kW/cm^2. The approach outlined in [55, 56, 57] utilized polymethylmethacrylate (PMMA) waveguides with a refractive index $n \approx 1.49$, which was shown to produce decent diffraction-limited TIRF images. Grandin et. al. [54] used the high index material Ta_2O_5 in their work, which is also one of the two materials used in this thesis.

3.2 Waveguides for chip-based TIRF imaging

A successful waveguide platform can be developed with materials having low propagation loss, low absorption and low auto-fluorescence for optical microscopy/nanoscopy at visible wavelengths (400-700 nm). These wavelengths are of interest as the most commonly used fluorophores operate within this

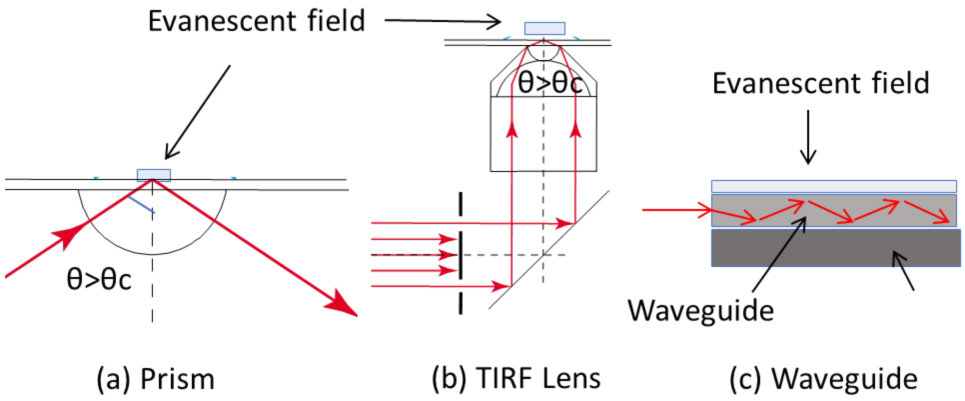

Figure 3.2: TIRF microscopy can be achieved using either (a) a prism or (b) an objective lens, with the latter being the most used due to availability commercially. (c) In this work, an integrated photonic chip was used, creating an evanescent field over arbitrarily large fields-of-view, only limited by waveguide geometry. This method allows for a simple optical setup.

span. In this work, two materials were investigated, silicon nitride (Si_3N_4), n = 2.03 @ 633 nm) and tantalum pentoxide (Ta_2O_5, n=2.12) due to their high refractive index and their availability within our group. Moreover, the CMOS compatibility of the Si_3N_4 platform makes it highly relevant for large scale and low-cost fabrication.

Experiments using both the materials showed that Ta_2O_5 waveguides were more suited towards shorter wavelengths than Si_3N_4, due to autofluorescence of Si_3N_4. However, this autofluorescence could potentially be reduced by developing suitable fabrication parameters for Si_3N_4 for the low visible wavelengths, although this is not a topic for this thesis.

Both materials are used throughout this thesis. In the future, materials with even higher refractive indices (e.g titanium oxide) will be explored, as these would benefit the super-resolution methods needing either high evanescent field intensity or high spatial frequency illumination patterns.

3.2.1 Waveguide designs for chip-based microscopy

When optimizing designs for chip-based microscopy one consideration is the evanescent field strength. Adequate field strength is a compromise between coupling loss and propagation loss. The coupling loss could be minimized when the modal overlap between the input laser and the waveguide mode is good, which for the waveguide structures used here led us to use coupling

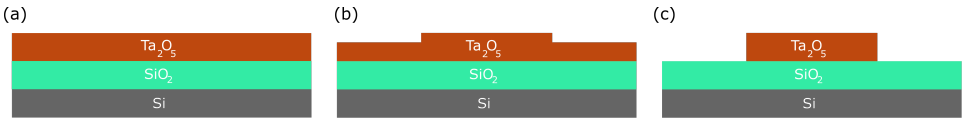

Figure 3.3: Three different waveguide cross-sections. The waveguides are made with a silicon wafer as a base, with an oxidized layer just above. The waveguide layers are made from either Ta_2O_5 or Si_3N_4. (a) The slab waveguide: A guiding layer all over the chip without confinement in the lateral direction. (b) The rib waveguide: Partially etched slab allowing singlemode operation for dimensions of around 1 μm width and 4 nm rib height. Rib waveguides have a low propagating loss due to the reduced sidewalls, but have higher bending losses than strip waveguides. (c) Strip waveguides have fully etched channels that allow for highly multimode waveguides. Strips have higher propagation loss due to the fully etched sidewalls, but lower bending loss. Thus light can propagate through sharper bends in strip compared to rib waveguides.

optics with N.A. = 0.5. Once the light is coupled in the waveguide, the main loss contribution in a straight waveguide stems from sidewall roughness. The number of guided modes (2.14) must be considered, since larger waveguide cross-sections will allow higher-order modes to propagate.

Three different waveguide structures were investigated. A slab waveguide (Fig .3.3(a)) confines light along the axial direction only, and light thus freely diverges along the lateral dimensions. This structure can be used for fluorescence excitation but lacks some of the control over the mode-profiles that you can have by using etched waveguides. Furthermore, the power density will be lower due to the light diverging over the chip. For the work within this thesis, strip and rib waveguides were used.

A rib waveguide (Fig .3.3(b)) is a slab with a partially etched channel. In a rib, light is confined laterally, but owing to the reduced sidewalls, the propagation losses are small (less sidewall interaction). Rib waveguides, however, are more prone to bending losses due to weaker lateral confinement of the light. Due to the shallow rib, singlemode condition can be more easily achieved for visible wavelengths down to waveguide widths of around 1 um (for slab thickness of 150 nm), which is also at the lower limit of the chip fabrication methods used by our collaborators.

Strip waveguides (Fig .3.3(c) have fully etched sidewalls. This will allow light to be more efficiently guided in sharp bends, but the sidewall roughness adds to the propagation loss. Strip waveguides show multimode behavior in the visible wavelengths for all the structures used here.

In this work, the waveguide core height for Si_3N_4 waveguides was chosen to be 150 nm and the rib height was 4 nm, which in simulations have been shown

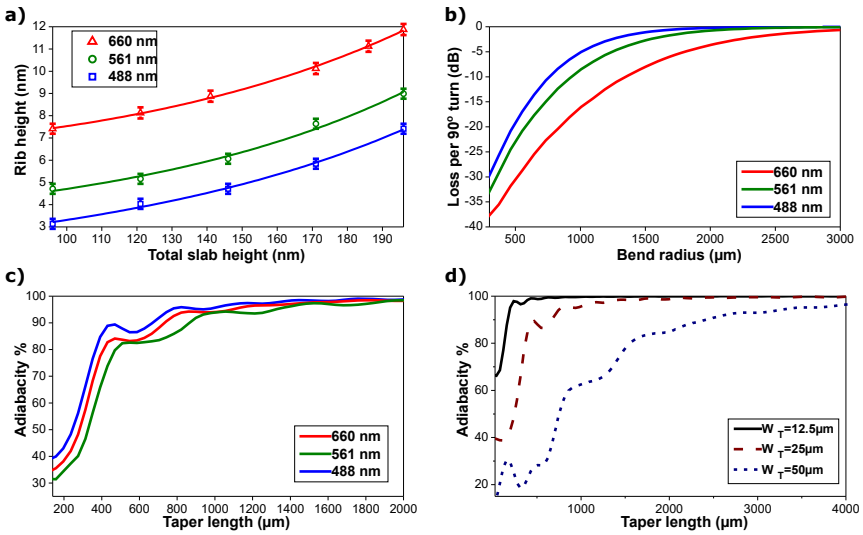

Figure 3.4: (a) Simulation of rib heights as a function of slab height for singlemode condition. (b) Bend loss per 90° waveguide bend is simulated as a function of the bend radius for three different wavelengths. (c) The adiabaticity of singlemode waveguides as a function of the tapering length, for three different wavelengths. (d) To decide the final width of the waveguide after the taper, the adiabaticity was simulated as a function of taper length for three different waveguide widths (i.e width after the taper) for 660 nm wavelength. TE-polarization was used for the simulation. Simulations by J.C. Tinguely.

to give singlemode conditions for the desired wavelengths 488 nm, 561 nm and 660 nm (Fig. 3.4(a)). These wavelengths were chosen due to their match with popular fluorophores. The waveguide core height for the Ta_2O_5 waveguides used in paper 1 and paper 3 were 200-220 nm, albeit singlemode conditions was not a topic for these papers and fully etched strip waveguides were used.

When incorporating waveguide bends (used in paper 2 and paper 5), the sharpness of the turn will add to radiation loss for the guided mode. By using rib waveguides, the radiation loss increases (compared with strip waveguides) due to the low transverse confinement. In Fig. 3.4(b), the bend loss is simulated for different bend radii for visible wavelengths. It is observed that the bend radius needs to be relatively large to minimize bend loss. In this work, we chose to use a 2 mm bend radius. Furthermore, higher-order modes will be less confined in bends than the fundamental modes. Thus a waveguide bend can be used as a mode reduction filter, which is further discussed in paper 2.

Adiabatic tapering was used in papers 2 and 5, which allows singlemode waveg-

uides to be expanded in the transverse direction while maintaining the single-mode condition. The tapering length and final width were chosen based on Fig. 3.4(c,d) as 2 mm and 25 μm, respectively.

Biological samples, such as cells or tissue sections, are typically stretching from 10 um and upwards laterally. This means that the desired waveguides for fluorescence microscopy should have widths of at least 10 um to cover any structure of interest, and ideally larger than this. In this work, biological samples were imaged using waveguide widths up to 600 μm successfully.

3.2.2 Chip fabrication

The fabrication of chips is beyond the scope of this thesis, and for this work the chip fabrication was outsourced. All additional components on top of the chip, such as PDMS sample wells and thermo-optics (chapter 5) were fabricated in-house.

Si_3N_4 chips were made at Centro Nacional de Microelectrónica IMB-CNM, Barcelona. The Ta_2O_5 waveguides were produced at Optoelectronics Research Centre, University of Southampton. A brief description of the fabrication process follows, but more detail can be found in the literature [59, 60].

Ta_2O_5 waveguides were made by first sputtering a (200 nm-220 nm) layer of Ta_2O_5 onto an oxidized silicon substrate using magnetron sputtering. The parameters were iteratively optimized to 200°C (substrate temperature), 300 W (magnetron power) and 5/20 s.c.c.m. O_2/Ar. The waveguides were realized using photolithography and ion beam milling. Plasma ashing was used to remove any remaining photoresist before the wafers were annealed for 5h at 600°C.

For Si_3N_4 waveguides, the silica layer was thermally grown and the Si_3N_4 was deposited using low-pressure chemical vapor deposition (LPCVD) at 800°C. The waveguide geometries were laid out using photo-lithography and realized using reactive ion etching (RIE). An additional protective top cladding was deposited using plasma-enhanced chemical vapor deposition at 300°C to a thickness of 1.5 μm.

3.3 Chip-based microscopy - the concept

In this section, the chip-based microscopy concept is outlined and some of the benefits over existing methods are discussed. In a conventional fluorescence

microscope, the sample is mounted on a coverglass and typically sealed onto a thicker glass slide before being mounted on the microscope. Alternatively, specialized coverglasses with sample wells are used. The excitation light is introduced onto the sample using a lens, typically the same objective lens used for acquiring the image. Contrarily, chip-based microscopy uses PIC chips to both hold and illuminate the sample, and the image is acquired via an independent objective lens (Fig. 3.5). A silicon chip with a high refractive index waveguide layer on an oxidized substrate is used to guide light from the input facet of the chip and towards the center. The light in the high index material is guided by total internal reflection, and thus acts as the source of an exponentially decaying evanescent wave, which penetrates the surrounding materials with a depth given by (2.16). At the top surface of the waveguide, fluorescently labeled samples are placed in direct contact with the evanescent field, and embedded in an aqueous imaging buffer. The fluorescent molecules are excited by the evanescent field, and the emitted fluorescence is captured using a microscope with an objective lens and a camera (Fig. 3.5(c,d)). By illuminating the sample with evanescent fields (TIRF), a high degree of optical sectioning is achieved which gives excellent SNR due to the low evanescent field penetration depth.

The experimental setup (Fig. 3.5(a)) consists of a basic upright microscope equipped with fluorescent filters and a high-end sCMOS camera connected to a computer. The PIC is placed on a xyz translation stage with a vacuum chuck to prevent lateral movement. Excitation light from a laser is coupled onto the input side facets using either an objective lens or a fiber. Many waveguides can be placed side by side on one chip to allow several imaging cycles per sample preparation (Fig. 3.5(b)). A sample chamber was made from PDMS, which is transparent at visible wavelengths, and thus can be stuck directly on top of the waveguides. The PDMS is open in the center allowing for the sample to be embedded in aqueous buffers. A coverglass is used to seal the sample (Fig. 3.5(d)).

Decoupling of illumination and collection light paths

Illuminating the sample using waveguides completely separates the excitation and collection light paths. This allows the user to freely choose the imaging objective lens, to not be limited by the high N.A. objective of conventional TIRF. This offers scalable TIRF imaging, where the size of the FOV and the image resolution can be determined based on the needs of the investigator, and not permanently fixed by the imaging system. Imaging using different magnification/N.A. objectives are demonstrated in Fig. 3.6. Here, the waveguide-based illumination remains unchanged while images using different objective lenses are acquired. The figure shows a 50 μm wide waveguide with cells (LSECs)

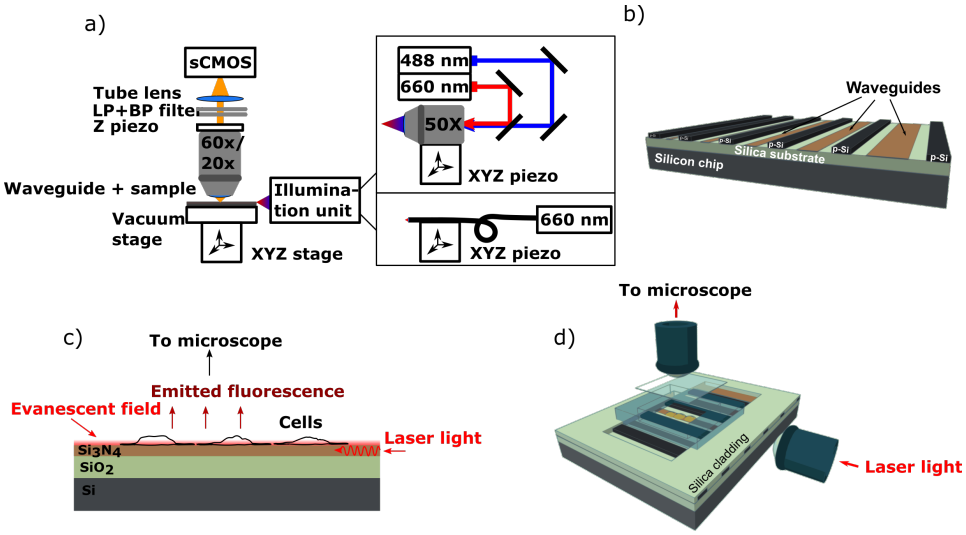

Figure 3.5: (a) Chip-based microscopy uses an upright microscope configuration. The chip is resting on a vacuum stage, and laser light can be coupled on to the side facet of the chip using an objective lens or a fiber. (b) high index contrast (HIC) waveguides are arranged side-by-side on the chip, allowing for multiple image cycles per sample preparation. A layer of polysilicon is added to block unwanted coupling between adjacent waveguides. (c) When laser light propagates in the waveguide layer, the resulting evanescent field excites fluorescence in the sample. (d) The chip can have protective silica cladding around the periphery, with an opening in the center of the chip to access the evanescent field. A Polydimethylsiloxane (PDMS) sample well is used to hold the aqueous image buffers, and a coverglass seals the sample. The chip size is around 3 x 3 cm^2.

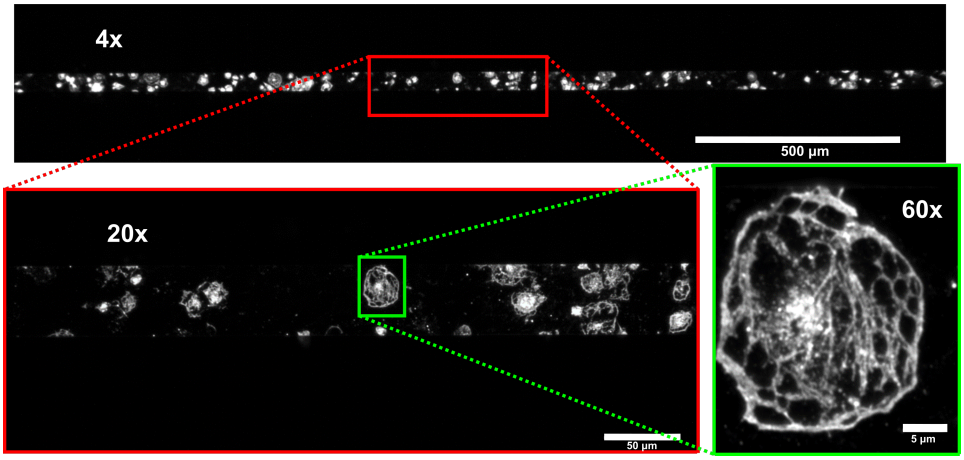

Figure 3.6: Chip-based microscopy separates the excitation and collection light paths. This allows imaging with different imaging objectives, without interfering with the TIRF illumination. This can be useful for observing a large population in a low magnification objective, e.g looking for rare events. Higher resolution images can be acquired by changing to objectives with higher N.A.. The decreasing FOV size is observed when higher magnification (and higher N.A.) objectives are used, but with increased resolution.

attached to the surface. The cells have been labeled with a fluorescent dye (CellMask Orange plasma membrane stain) and the waveguide is guiding light from a 561 nm laser (from left to right in the image). The 4x image shows that the length of the waveguide is illuminated and the cells are excited over the whole geometry. By rotating the microscope objective revolver, a compromise between FOV and resolution can be made, here shown with 4x, 20x and 60x objective lenses, with the 60x having N.A. = 1.2 and thus giving the best resolution but smallest FOV. In objective-based TIRF, low N.A. TIRF objectives are not available, and thus this remains a largely unexplored direction.

Furthermore, it is observed from Fig. 3.6 the transverse confinement that the waveguide is providing: The FOV is completely covered with cells, but nothing other than the waveguide is illuminated. This can be harnessed e.g if the user wants several imaging cycles on the same sample chip. The waveguides can be arranged side-by-side and the adjacent waveguide can be made active by moving the position of the objective used for coupling the light (Fig. 3.5(b)). For high throughput imaging the width of the waveguide can be chosen to match the FOV available for the objective lens, e.g using a 600 μm wide waveguide with a 25x/0.8 N.A objective, which allows a FOV of 500 x 500 μm^2 as seen in Fig. 3.7, where a sample of LSECs labeled for tubulin is shown. Simultaneous imaging of a large sample population could increase the chance of spotting rare events or increasing the statistical relevance of a finding. To image such a large FOV using objective-based TIRF would involve image stitching of sequentially

acquired images with smaller FOV (FOV size indicated with a white box in Fig. 3.7).

Uniform TIRF illumination over a large field-of-view

While all the methods reported in [54, 55, 56, 57] showed working chip-based TIRF imaging, some of their results suffer from non-homogeneity in the illumination intensity distribution [54]. The authors explain the cause of the inhomogeneity to be stemming from rough facets used for coupling the light onto the waveguides (in this case using grating coupling). Agnarsson et. al. [55] show a more uniform excitation intensity distribution, without arguing on the reason. An understated difference between the two groups' approaches is the choice of illumination light source. Grandin et. al. [54] used a laser and experienced inhomogeneous illumination, while Agnarsson et. al [55] used a white light source and had more planar illumination, with less intensity modulation. We believe that the differences here stem from multi-mode interference (MMI), an effect more obvious when using a highly coherent light source (such as a laser). By using a thin waveguide layer, singlemode conditions can be fulfilled in the vertical direction; however, wide waveguide geometries allow transverse modes to propagate causing MMI patterns. The MMI patterns can be avoided using low-coherence light or coherent light with singlemode waveguides. Alternatively the MMI patterns can be scrambled as will be shown here. To illustrate this, an example image of the intensity distribution used in this thesis is shown in Fig. 3.8. Figure 3.8(a) shows the MMI pattern, which would excite the specimen unevenly, while Fig. 3.8(b) shows the same experiment but using scrambling of the MMI pattern (method shown later in the chapter). Thus, the fluorescence excitation light should ideally have a planar/flat intensity profile, as shown in Fig. 3.8(b), to give a correct representation of the sample. This is demonstrated in Fig. 3.8(c,d) where the effect of imaging cells with the MMI pattern, and with the MMI pattern scrambled are shown, respectively.

In the case of SMLM techniques such as dSTORM (which will be shown in chapter 4), the temporary dark state lifetimes are directly affected by the excitation light intensity, where regions flooded with excitation light give longer-lived dark states, allowing for efficient localization of the emitters. In less-illuminated regions there could potentially be overlapping emitters due to the low intensity (low dark-state accumulation). Thus, MMI patterns in SMLM are affecting the image negatively.

In either case, MMI excitation patterns should be avoided. To alleviate problems of non-homogeneous illumination, two approaches were followed. We investigated adiabatic tapering to expand singlemode waveguides from widths

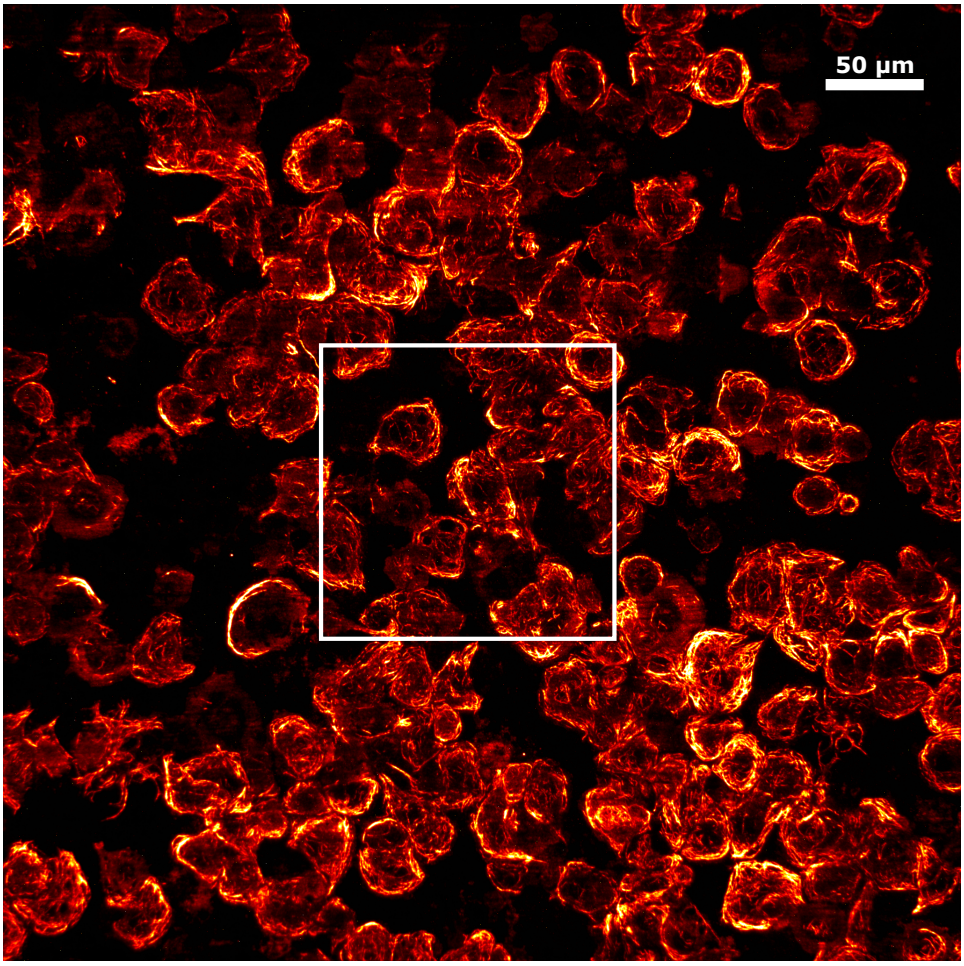

Figure 3.7: Chip-based TIRF imaging over a 500 x 500 μm^2 large field of view, showing a sample of LSECs with the tubulin network labeled. The FOV that could be expected in conventional objective-based TIRF is marked with a white square (150 x 150 μm^2). Here, a 600 μm strip Si_3N_4 waveguide was used, with excitation wavelength of 660 nm.

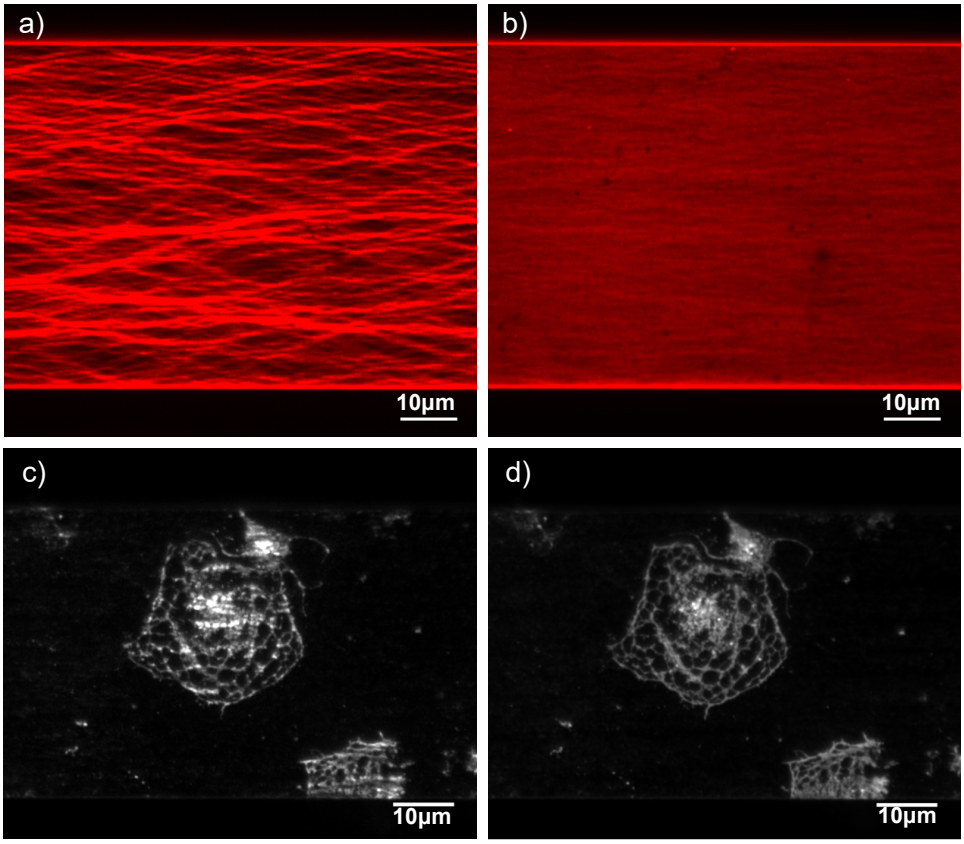

Figure 3.8: (a) A MMI is formed using a strip waveguide. The pattern is observed in the microscope by staining the surface of the waveguide with a fluorescent marker (Alexa-647 in poly-l-lysine). (b) The MMI pattern is greatly damped by averaging it out over time using sub-sets of different mode patterns like the one shown in a). The method is explained in Fig. 3.9. (c) The fluorescence image quality of a cell is reduced by the MMI strip patterns. (d) By scrambling the modes the image quality is restored.

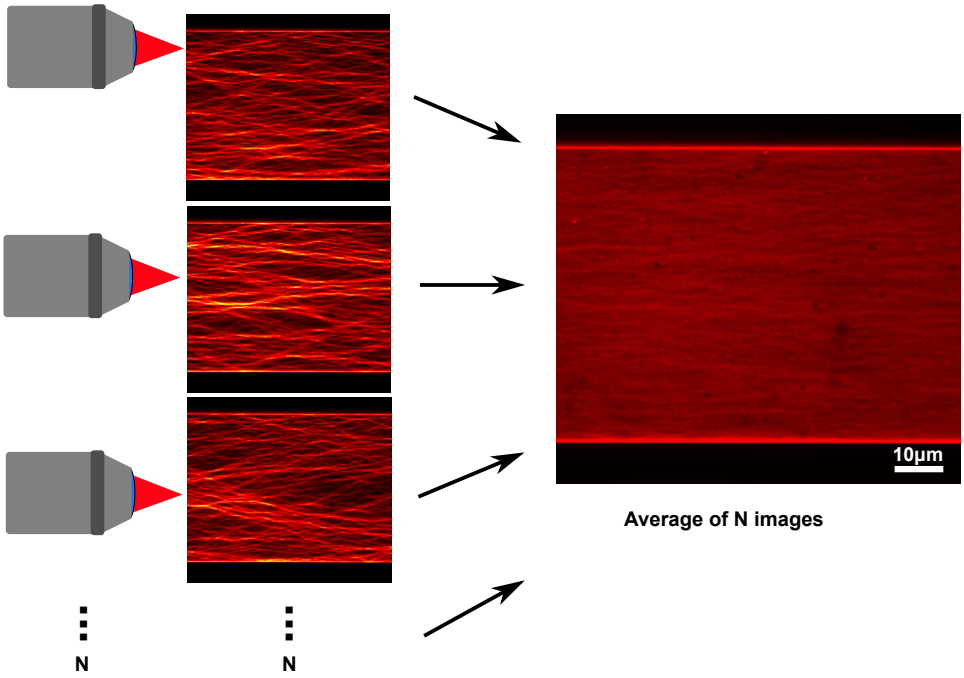

Figure 3.9: MMI scrambling is achieved by shifting the MMI pattern in time by moving the input coupling objective. The mode patterns can then be averaged out.

of 1-1.5 μm up to a width of 25 μm. Using adiabatic tapering the singlemode condition is kept, and the illumination profile is free from multimode interference patterns. Adiabatic tapering is utilized for on-chip nanoscopy techniques relying on singlemode operation, preferably SIM (ch. 5, paper 5), but is here also investigated for diffraction-limited chip-based TIRF microscopy (paper 2). A recent publication explored adiabatic tapering up to 100 μm for SMLM imaging [61].

Another method of achieving uniform excitation light using wide waveguides was developed without the need for adiabatic tapering. Here, very wide (up to 1 mm) multimode waveguides having constant widths throughout the chip were used. To even out the MMI patterns, the coupling objective lens was translated across the input facet while maintaining coupling as seen in Fig. 3.9. This makes the MMI pattern shift its spatial distribution in time according to the position of the coupling objective. In this manner, the multimode interference patterns could be averaged out, leaving a nearly flat excitation profile. Using a piezo actuator on the xyz stage holding the coupling objective lens (Fig. 3.5(a)), small incremental movements in the input coupling were used, and around 200 images needed to be acquired to achieve even illumination. This method was used when acquiring the images in Fig. 3.8.

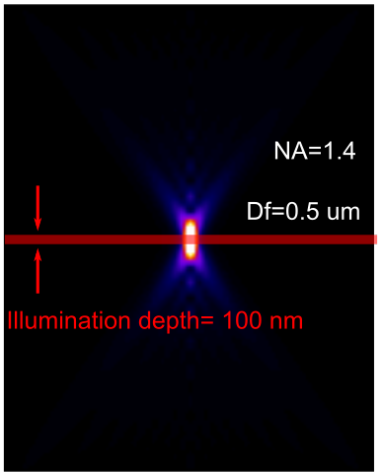

Figure 3.10: Using a waveguide, the illumination is more confined axially than when using an objective lens. Here a high N.A. objective lens is simulated giving a 500 nm depth of field, while the waveguides used in this thesis have a penetration depth of around 100 nm (for 660 nm excitation light).

High index waveguides shape the excitation light

By focusing light using lenses, the smallest spot possible is given by the N.A. of the lens used for focusing, which can be stated by the Abbe diffraction limit (2.4). The light is thus confined by $\lambda/N.A.$, while for the waveguide, light is confined by λ/n_f. This implies tighter confinement for waveguides since n_f is in the range of $1.7 - 1.8$ for Si_3N_4 and Ta_2O_5, while common high N.A. objectives have N.A.=1.4 (Fig. 3.10). This property for waveguides was used in chapter 4 and 5 for ESI and Chip-based structured illumination microscopy (CSIM), where high spatial frequency (due to n_f) interference fringes are used for super-resolution imaging.

Furthermore, by altering waveguide geometries, different light patterns can be generated. Different light patterns can be used to aid multi-modal imaging on the chip, since the nanoscopy methods require everything from planar illumination for SMLM (ch. 4, paper 3 and paper 4), to strictly controlled illumination patterns for SIM (ch. 5, paper 5) and to highly chaotic illumination for fluctuation-based methods (ch.4, paper 3). All of these can be generated using fundamental waveguide designs such as straight waveguides, waveguide bends, waveguide y-branches and waveguide loops (Fig. 3.11). Furthermore, using different wavelengths is effortless using waveguides (paper 2, figure 5 in paper 3). This is not the case for objective-based TIRF, where the critical angle must be adjusted for when changing excitation wavelengths.

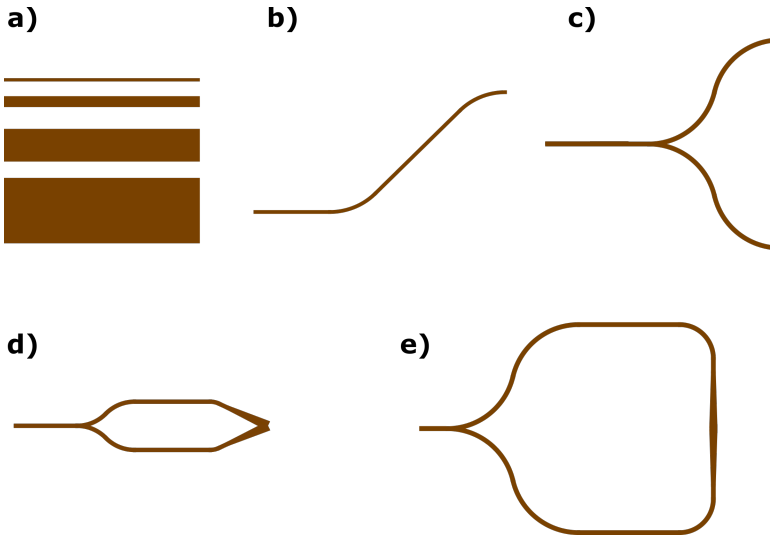

Figure 3.11: The different excitation light pattern used in this work can be generated using different basic waveguide elements such as (a) straight waveguides of different widths, (b) bends, (c) y-branches and (d,e) loops.

3.4 Results and discussion

The outcome of the experiments leading to paper 1 gave a first impression on the viability of using Ta_2O_5 waveguides for TIRF imaging. Bio-compatibility of biological material on-chip was investigated, and the setup was tested for imaging at different wavelengths and using different fluorescent stains. The results show that Ta_2O_5 is a useful material for chip-based microscopy, compatible with wavelength multiplexing, and can be used in a bio-lab much the same way as the traditional sample glass/coverglass slide is used for sample preparation of fixed cells. The benefits of having a PDMS sample chamber is both to hold the sample and imaging buffers, but also helps to lift the coverglass from the waveguide, thus hindering light from uncladded waveguides or non-guided light from coupling onto the coverglass, which could lead to increased background.

In paper 2, Si_3N_4 was investigated for use as a waveguide layer. The benefit of this material over Ta_2O_5 is mainly its availability in common CMOS foundries, as the refractive index is nearly as high as Ta_2O_5. Also, Si_3N_4 has been seen to exhibit autofluorescence at lower wavelengths, a property not wanted in TIRF microscopy. The Si_3N_4 platform was investigated for bio-compatibility of both live and fixed cells, with results showing again that the chip can be used under the same conditions as conventional microscopy when preparing the sample. To perform a thorough investigation of live-cell compatibility is beyond the scope of the thesis. Emphasis on live-cell imaging was mostly regarding

the compatibility in chip handling. For living cells, the chips were left in an incubator allowing cells to attach, demonstrating the non-toxic environment provided by the chip. In this work, adiabatic tapering was used to expand the fundamental mode up to dimensions useful for bio-imaging: 1.5 μm wide waveguides expanded up to 25 μm, to have a more uniform illumination than what can be seen in previous work [54]. The results show that singlemode was maintained for 660 nm wavelength. For 488 nm and 561 nm the waveguides are not singlemode from the start, leading to higher-order modes visible after the taper. This is seen as dark areas in scattered light or using fluorescence. It was found that by filtering the light in a bend, the fundamental mode could be achieved. This is possible due to the low confinement of higher-order modes in bends on a rib waveguide. The effective refractive index of the higher-order modes are less than the fundamental mode, leading to higher bend loss, effectively filtering the modes. The experiments were compared with simulations.

Although singlemode waveguides yield a more uniform excitation pattern than multimode waveguides, the adiabatic tapering makes for rather large waveguides structures, especially if high throughput is needed using wide waveguides. Singlemode waveguides are used for the work on chip-based SIM in chapter 5. In the following chapter, mode-scrambling will be emphasized for the implementation of dSTORM on-chip, allowing for very large areas to be illuminated.

3.5 Paper 1: Chip-based optical microscopy for imaging membrane sieve plates of liver scavenger cells.

Published in Spie proceedings, 2015.

Authors: Øystein I. Helle, Cristina I. Øie, Peter McCourt and Balpreet S. Ahluwalia.

Author contributions: Ø.I.H. did the experiments, analyzed the data and wrote the first draft of the paper. C.I.Ø. did the sample preparation and staining. B.S.A. and P.MC. supervised and guided the project All authors reviewed the paper.

Chip-based optical microscopy for imaging membrane sieve plates of liver scavenger cells

Øystein Ivar Helle[1], Cristina Ionica Øie[2], Peter McCourt[2], Balpreet Singh Ahluwalia*[1]

UiT-The Arctic University of Norway
Department of Physics and Technology[1], Department of Medical Biology[2]
9037 TROMSØ, NORWAY

E-mail*: Balpreet.singh.ahluwalia@uit.no

ABSTRACT

The evanescent field on top of optical waveguides is used to image membrane network and sieve-plates of liver endothelial cells. In waveguide excitation, the evanescent field is dominant only near the surface (~100-150 nm) providing a default optical sectioning by illuminating fluorophores in close proximity to the surface and thus benefiting higher signal-to-noise ratio. The sieve plates of liver sinusoidal endothelial cells are present on the cell membrane, thus near-field waveguide chip-based microscopy configuration is preferred over epi-fluorescence. The waveguide chip is compatible with optical fiber components allowing easy multiplexing to different wavelengths. In this paper, we will discuss the challenges and opportunities provided by integrated optical microscopy for imaging cell membranes.

1. INTRODUCTION TO WAVEGUIDE CHIP-BASED MICROSCOPY

Fluorescence microscopy has emerged as a vital tool in modern bio-medical imaging and diagnosis. Different fluorescent stains (dyes) that bind specifically to sub-cellular organelles, membrane, proteins, allow optical microscopy to provide specific intra-cellular level information. In total internal reflection fluorescence microscopy (TIRF), the surface evanescent field is used to illuminate the sample [1-5]. The evanescent field decays exponentially above the surface and is used to illuminate thin section of the sample (typically 150-200 nm). Unlike epi-fluorescence where the entire sample is illuminated, TIRF microscopy illuminates only a thin section of the cell providing a high signal-to-noise ratio by reducing the background signal and low photo-toxicity. TIRF microscopy is a preferred methodology for imaging targets or biological phenomena in close proximity to the cell membrane, such as cell membrane trafficking, cell adhesion points or structures present on cell membrane.

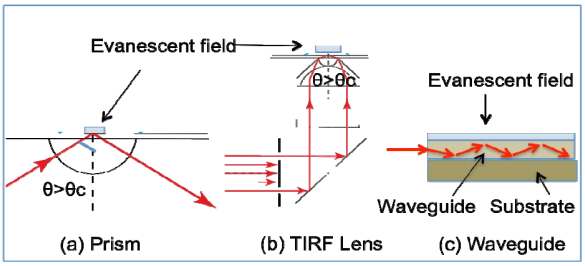

Figure 1: Different techniques to generate an evanescent field. a) Prism with angle of incidence greater than the critical angle, θ >θc. b) TIRF objective. c) Evanescent field on top of a waveguide.

Different techniques can be used to generate the evanescent field as shown in Fig. 1. The most commonly used method is a total internal reflection (TIR) objective lens. The TIR lens is used to generate the evanescent field at the surface of the cover slip, and illuminates the samples residing directly on top of cover slips. As shown in Fig. 1c, the light can be confined inside an optical waveguide and guided along a pre-fabricated pattern. On the surface of a waveguide, an evanescent field is present along the entire length of the waveguide (Fig 3c). The surface evanescent field of a waveguide can also be used for TIRF microscopy, in the same way as a TIR objective lens (Fig 1) [3-5]. In

Nanoimaging and Nanospectroscopy III, edited by Prabhat Verma, Alexander Egner, Proc. of SPIE
Vol. 9554, 95540O · © 2015 SPIE · CCC code: 0277-786X/15/$18 · doi: 10.1117/12.2187277

conventional TIR objective lens based microscopy both the illumination and the collection light path are guided thorough the TIR objective lens. Here, a waveguide-chip provides the illumination to the sample and any standard objective lens can be used to collect the signal, thus decoupling the illumination and the collection light path.

2. LIVER SINUSOIDAL ENDOTHELIAL CELLS

The liver cells such as Kupffer cells (KCs) and liver sinusoidal endothelial cells (LSECs) are engaged in blood clearance activity [6-9]. The LSECs, which line the very small blood vessels (sinusoids) of the liver, possess unique morphological characteristics called "fenestrations" (small holes grouped in sieve plates) with a mean diameter of approximately 100 nm. Together these cell types make up the body's most powerful scavenger system. In mammals, the KCs directly engulf and remove larger targets (>200 nm) whereas LSECs eliminate smaller targets (<200 nm) via clathrin mediated endocytosis. LSECs are uniquely characterized structurally with fenestrations (nano-holes of ~50-200 nm diameter) grouped in sieve plates (Figure 2), which allow small soluble material, but not larger particles to pass across the sinusoidal wall to the underlying parenchymal cells. As fenestrations and sieve plates are present only on the cell membrane, TIRF (total internal reflection microscopy) configuration is preferred over epi-fluorescence.

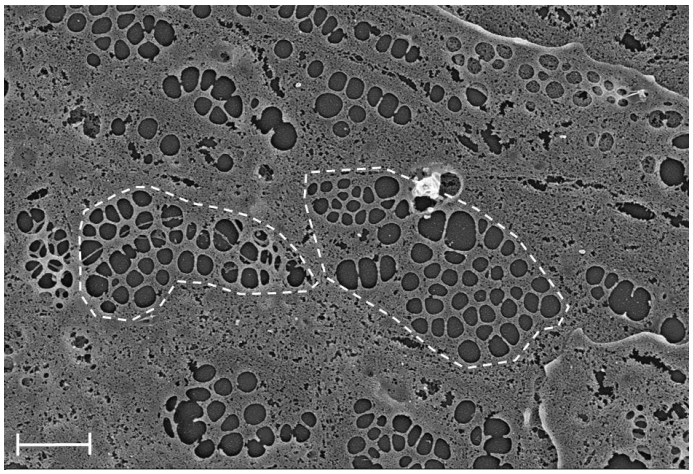

Figure 2. Scanning electron micrograph of rat LSEC plasma membrane showing fenestrations clustered in sieve plates (dotted line). Scale bar = 1 μm.

3. METHODOLOGY

Waveguide material: Low loss, low auto-fluorescence optical waveguides for visible light (532nm) are required for waveguide-chip based microscopy. Waveguides made of a material with a high refractive index, e.g. tantalum pentoxide (Ta_2O_5) or silicon nitride (Si_3N_4), give high intensity in the evanescent field and a smaller penetration depth. In this work we used optical waveguides made of tantalum pentoxide (Ta_2O_5), n =2.1 and high refractive index contract (Δn) of 0.75 when compared with SiO_2 (n= 1.45). We have previously optimized the fabrication process for Ta_2O_5 waveguides [10-11] and have used them for waveguide trapping application [12-15]. Strip waveguides with a strip height of 110 nm on silcon dioxide substrates were used for imaging. A 5 μm thick SiO_2 was present below the waveguide layer as a cladding layer. Due to the large size of the imaged cells, the width of the waveguides used are either 50μm or 100 μm. This ensures that the imaging region will be suited for the rathter large stretch of the LSECs.

Cell isolation staining: Rat LSECs were prepared by collagenase perfusion of the liver, low speed differential centrifugation and Percoll gradient sedimentation [16], followed by KCs depletion by seeding the nonparenchymal fraction onto plastic culture dishes. This resulted in a cell suspension enriched in LSECs. Human LSECs were also isolated from patients undergoing liver resections based on immunomagnetic selection. The cells were seeded on waveguides pre-coated with fibronectin and allowed attachment for 1h. Non attached cells and debris were removed, and after another 1h of incubation, the cell were fixed with 4 % PFA for 10 minutes at RT. Following a 30 min incubation with 1% BSA to minimize unspecific binding of the dyes, the cells were stained for actin filaments by incubating the

cells for 20 min at 37°C with Alexa Fluor 647 Phalloidin (1:40 dilution in PBS). After extensive washes with PBS, the plasma membrane was stained by incubating the cells for 10 min at RT with Cell Mask Orange (working concentration of 1.25 ng/ml in PBS).

Experimental set-up: The experimental set-up employed is shown in Figure 3. The two lasers beams 532 nm and 638 nm were used for TIRF excitation and were combined and coupled into the waveguides using an 50X 0.5 NA objective lens. The input coupling objective lens was kept on a translation stage to optimize the coupling efficiency on to the waveguide chip. An upright microscope (Olympus) with adequate emission filter sets was used, also this mounted on a translation stage allowing freedom to move the field of view around on the waveguide chip. The images were captured using a sensitive sCMOS camera (Hamamatsu Orca Flash 4). For epi-fluorescence imaging, another 532 nm laser was introduced from the top of the microscope as shown in Fig. 3. The sample chamber was made using thin PDMS layer (110 nm thickness), with an opening at the center to introduce the cells and image buffer. The thickness of the PDMS chamber was matched to the shortest working distance of the objective lenses used for imaging, to ensure the best possible image quality. The PDMS opening was sealed by a cover slip and different N.A. objective lens were used to acquire images. The cells were placed on top of the waveguide and were illuminated by the evanescent field of the waveguide for 2D imaging and by the propagating laser beam for epi-fluorescence mode.

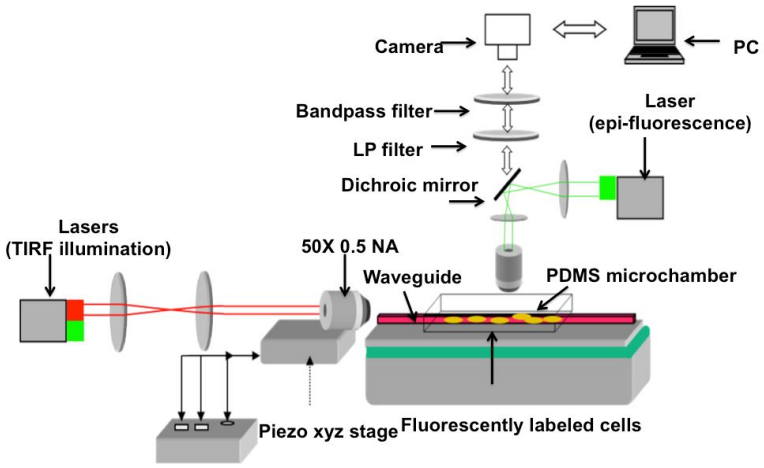

Figure 3 Experimental set-up of waveguide-chip based microscopy. Lasers (532 nm/638 nm) were used for 2D chip-based imaging and another 532 nm laser was used for epi-fluorescence from the top of an upright microscope.

4. WAVEGUIDE CHIP-BASED IMAGING OF LIVER CELLS

The primary LSECs were immobilized directly on top of waveguides, fixed within 3 hours after the isolation and stained. The waveguide is coated with a thin layer of fibronectin to help immobilization of LSECs on the waveguide surface. Figure 4a shows a bright field image of LSECs and Figure 3c shows the cells imaged using the evanescent field of the waveguide. The cell membrane network and sieve-plates (dark areas in the membrane) are imaged, while Fig. 3b shows an epi-fluorescence image of the same cell. In epi-fluorescence excitation the cell nucleus become emphasized as a consequence of the top-illumination, and as illumination power increases the signals from the nucleus saturates the image before the membrane sieve plates can be imaged. The images were acquired using a 50X 0.8NA objective lens. The 532 nm excitation laser was operated in the range of 200-300 mW for waveguide imaging, with exposure time of 300 ms. The fairly high power is needed due to high losses associated with the coupling loss and the propagation loss. The estimated guided power inside the waveguide is less than 5mW. For epi-illumination considerably less power is needed to achieve the appropriate illumination of the fluoreophores (in the range of 10-20 mW). In separate experiments, human LSECs were stained with Alexa 647 Phalloidin and imaged using waveguide excitation (laser 638 nm). The images of actin in human LSEC are shown in Figure 5. The images were acquired by a water immersion objective lens (60X 1.2NA). The actin filaments are used to measure the resolution of the method, and found to be 295nm at full width

half maximum (FWHM) after a deconvolution algorithm is employed on the acquired image. Due to rapid decay of the evanescent field from the waveguide surface, low background noise is obtained in chip-based microscopy.

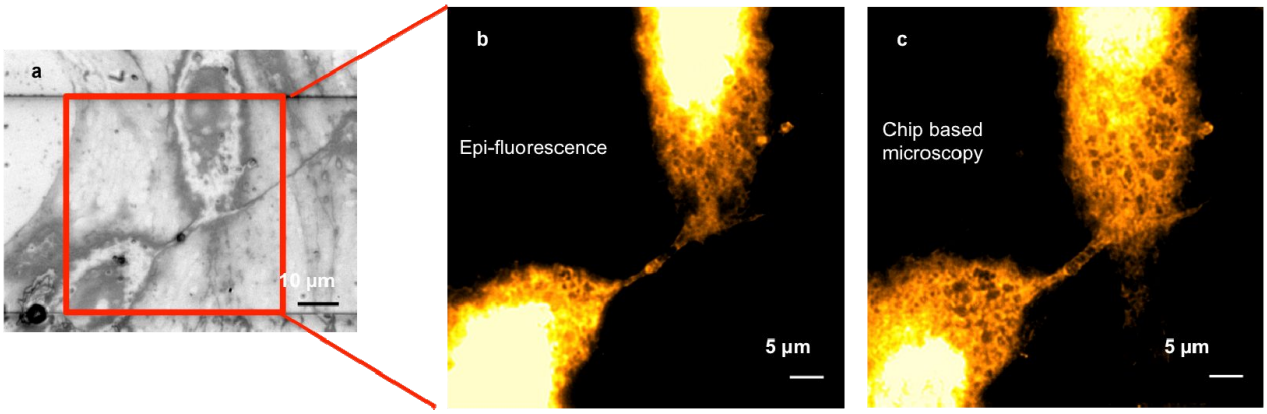

Figure 4: a) Bright field image of rat LSECs located on top of the waveguide surface. b) Waveguide TIRF image of cell region. The sieve plates present on cell membrane are imaged (dark areas present on cell membrane),c) Epi-fluorescence image of same cells.

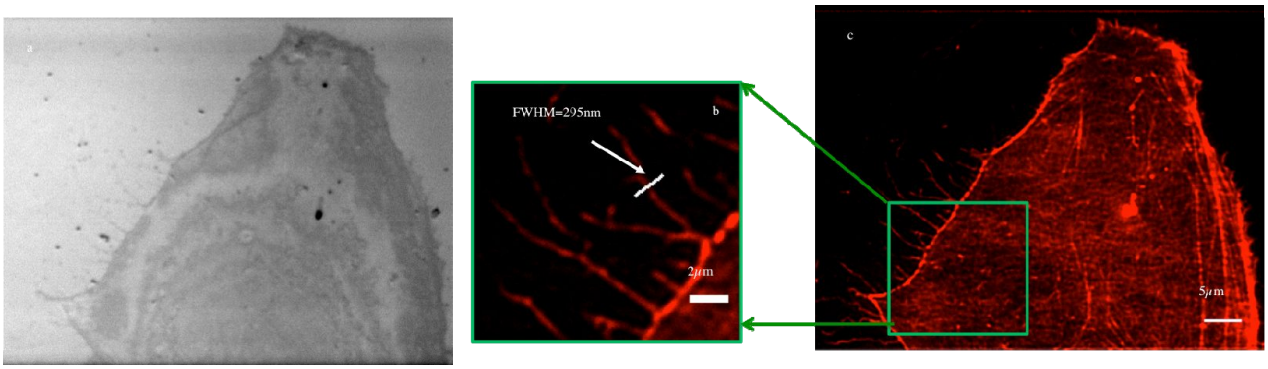

Figure 5: a) Bright field image of human LSEC on top of waveguide. b-c) Waveguide TRIF image of the same cell. The cell is stained with Alexa 647-phalloidin exposing cell actin. The FWHM is 295 nm.

5. CONCLUSION

We have used waveguide-chips made of high-refractive index contrast material (Ta_2O_5) for imaging membrane sieve plates and actins present in rat and human LSECs, respectively. In waveguide excitation, the evanescent field is dominant only near the surface (~100-150 nm) providing default optical sectioning and illuminating fluorophores that are in close proximity to the surface and thus benefiting higher signal-to-noise ratio. Optical waveguides provide a uniform excitation over large sample area and the method represents an integrated, on-chip approach for fluorescent imaging, with a possible extension towards super-resolution imaging methods. Waveguide-chip generates evanescent field along the entire length of the waveguide, when combined with low magnification, a large field-of-view can be imaged under TIR illumination. While, in conventional TIRF microscopy both imaging and excitation are coupled thus the field-of-view is limited by TIR lens (usually high magnification). For fluorescence microscopy, it is an advantage to stain different parts of a cell with different dyes and excite each dye with a different wavelength. The integrated chip-platform is compatible with optical fiber components which would allow easy multiplexing of different wavelengths for multi-color imaging. Combining waveguide imaging with planar waveguide trapping opens for the possibility of trapping particles (cells, bacteria etc.) on the waveguide, while aquiring TIRF images of the particles [12].

ACKNOWLEDGEMENTS

This work was supported by the European Union, European Research Council (ERC) Starting Grant "Nanoscopy" (No. 336716) and the FP7-HEALTH-2010-Alternative-Testing "Hepatic Microfluidic Bioreactor" (AOR 266777). The authors acknowledge valuable assistance from Olav G Helleso, Deanna L.Wolfson and Jean C Tinguely.

REFERENCES

[1] H. Schneckenburger, "Total internal reflection fluorescence microscopy: technical innovations and novel applications", Current Opinion in Biotechnology 16: 13-18 (2005).

[2] Beck, M., Aschwanden, M., Stemmer, A. "Sub-100-nanometre resolution in total internal reflection fluorescence microscopy", Journal of Microscopy 232: 99-105 (2008).

[3] B. Agnarsson, S. Ingthorsson, T. Gudjonsson, and K. Leosson, "Evanescent-wave fluorescence microscopy using symmetric planar waveguides," Opt. Express 17(7), 5075–5082 (2009).

[4] B. Agnarsson, J. Halldorsson, N. Arnfinnsdottir, S. Ingthorsson, T. Gudjonsson, and K. Leosson, "Fabrication of planar polymer waveguides for evanescent-wave sensing in aqueous environments," Microelectron. Eng. 87(1), 56–61 (2010).

[5] B. Agnarsson, A.B. Jonsdottir, N.B. Arnfinnsdottir, K. Leosson, On-chip modulation of evanescent illumination and live-cell imaging with polymer waveguides, Optics Express 19, 22929-22935 (2011)

[6] Cogger V, McNerney G, Nyunt T, DeLeve L, McCourt P, Smedsrød B, Le Couteur D, Huser TR "Three-dimensional structured illumination microscopy of liver sinusoidal endothelial cell fenestrations", Journal of Structural Biology 171:382-388 (2010).

[7] Braet F, "How molecular microscopy revealed new insights in the dynamics of hepatic endothelial fenestrae in the past decade", Liver Int 24:532–539, (2004).

[8] R. Fraser, V.C. Cogger, B. Dobbs, H. Jamieson, A. Warren, S.N. Hilmer, and D.G. Le Couteur, "The liver sieve and atherosclerosis", Pathology 44:181-186, (2012)

[9] D.G. Le Couteur, R. Fraser, S.N. Hilmer, L.P. Rivory and A.J. McLean, "The hepatic sinusoid in aging and cirrhosis: effects on hepatic substrate deposition and drug clearance", Clin Pharmacokinet 44:187-200 (2005)

[10] Ahluwalia, B., S, Subramanian, A., Z., Hellesø, O., G., Perney, N., M., B., Sessions, N., P., Wilkinson, J., S., "Fabrication of sub-micron high refractive index tantalum pentoxide waveguides for optical propulsion of microparticles," Photon. Tech. Lett. 21, 1408-1410 (2009).

[11] B. P. S. Ahluwalia, Olav Gaute Hellesø; Ananth Z. Subramanian; James S. Wilkinson; Jie Chen; Xuyuan Chen., "Integrated platform based on high refractive index contrast waveguide for optical guiding and sorting", Proc. SPIE 7613, 76130R (2010).

[12] Øystein, Ivar Helle, Balpreet Singh Ahluwalia, Olav Gaute, Hellesø, "Optical transport, lifting and trapping of micro-particles by planar waveguides", Opt Exp., 23(5), (2015).

[13] Balpreet S Ahluwalia, Peter McCourt, Ana Oteiza, James S. Wilkinson, Thomas R. Huser and Olav G Hellesø, "Squeezing red blood cells with the evanescent field of an optical waveguide to monitor cell deformability during blood storage", Analyst, 140, 223-229, (2015).

[14] B. S. Ahluwalia, Peter McCourt, Thomas Huser and Olav Gaute Hellesø, "Optical Trapping and propulsion of red blood cells on waveguide surfaces", Optics Express, 18, 21053 (2010).

[15] Hellesø, O., G., Løvhaugen, P., Subramanian, A., Z., Wilkinson, J., S., Ahluwalia, B., S., "Surface transport and stable trapping of particles and cells by an optical waveguide loop," Lab-on-a-chip, 12(18), 3436-40 (2012).

[16] Smedsrod, B. and H. Pertoft, "Preparation of pure hepatocytes and reticuloendothelial cells in high yield from a single rat liver by means of Percoll centrifugation and selective adherence", J Leukoc. Biol, **38**(2), 213-30, (1985).

3.6 Paper 2: Silicon nitride waveguide platform for fluorescence microscopy of living cells.

Published in Optics express, 2017.

Authors: Øystein I. Helle*, Jean-Claude Tinguely*
and Balpreet S. Ahluwalia

*Shared first-authorship/Authors of equal contribution.

Author contributions: Ø.I.H. build the setup, did the experiments and analyzed the data. J.C.T. did the simulations with analysis. B.S.A. supervised and guided the project. Ø.I.H. and J.C.T. wrote the first draft of the paper. All authors reviewed the paper.

Research Article | Vol. 25, No. 22 | 30 Oct 2017 | OPTICS EXPRESS 27678
Optics EXPRESS

Silicon nitride waveguide platform for fluorescence microscopy of living cells

JEAN-CLAUDE TINGUELY,[1,2] ØYSTEIN IVAR HELLE,[1,2] AND BALPREET SINGH AHLUWALIA[1,*]

[1]*Department of Physics and Technology, UiT-The Arctic University of Norway, 9037 Tromsø, Norway*
[2]*Authors with equal contribution to the paper*
**balpreet.singh.ahluwalia@uit.no*

Abstract: Waveguide chip-based microscopy reduces the complexity of total internal reflection fluorescence (TIRF) microscopy, and adds features like large field of view illumination, decoupling of illumination and collection path and easy multimodal imaging. However, for the technique to become widespread there is a need of low-loss and affordable waveguides made of high-refractive index material. Here, we develop and report a low-loss silicon nitride (Si_3N_4) waveguide platform for multi-color TIRF microscopy. Single mode conditions at visible wavelengths (488-660 nm) were achieved using shallow rib geometry. To generate uniform excitation over appropriate dimensions waveguide bends were used to filter-out higher modes followed by adiabatic tapering. Si_3N_4 material is finally shown to be biocompatible for growing and imaging living cells.

OCIS codes: (180.4243) Near-field microscopy; (130.0130) Integrated optics; (180.2520) Fluorescence microscopy; (170.3880) Medical and biological imaging.

References and links

1. A. Dhakal, P. Wuytens, F. Peyskens, A. Z. Subramanian, N. Le Thomas, and R. Baets, "Silicon-nitride waveguides for on-chip Raman spectroscopy," Proc. SPIE **9141**, 91410 (2014).
2. G. Yurtsever, P. Dumon, W. Bogaerts, and R. Baets, "Integrated photonic circuit in silicon on insulator for Fourier domain optical coherence tomography," Proc. SPIE **7554**, 75514B (2010).
3. F. T. Dullo, S. Lindecrantz, J. Jágerská, J. H. Hansen, M. Engqvist, S. A. Solbø, and O. G. Hellesø, "Sensitive on-chip methane detection with a cryptophane-A cladded Mach-Zehnder interferometer," Opt. Express **23**(24), 31564–31573 (2015).
4. P. Muellner, E. Melnik, G. Koppitsch, J. Kraft, F. Schrank, and R. Hainberger, "CMOS-compatible Si3N4 waveguides for optical biosensing," Procedia Eng. **120**, 578–581 (2015).
5. A. Gorin, A. Jaouad, E. Grondin, V. Aimez, and P. Charette, "Fabrication of silicon nitride waveguides for visible-light using PECVD: a study of the effect of plasma frequency on optical properties," Opt. Express **16**(18), 13509–13516 (2008).
6. A. Z. Subramanian, P. Neutens, A. Dhakal, R. Jansen, T. Claes, X. Rottenberg, F. Peyskens, S. Selvaraja, P. Helin, B. Du Bois, K. Leyssens, S. Severi, P. Deshpande, R. Baets, and P. Van Dorpe, "Low-Loss Singlemode PECVD Silicon Nitride Photonic Wire Waveguides for 532-900 nm Wavelength Window Fabricated Within a CMOS Pilot Line," IEEE Photonics J. **5**, 220809 (2013).
7. D. J. Moss, R. Morandotti, A. L. Gaeta, and M. Lipson, "New CMOS-compatible platforms based on silicon nitride and Hydex for nonlinear optics," Nat. Photonics **7**, 597–607 (2013).
8. J. Riemensberger, K. Hartinger, T. Herr, V. Brasch, R. Holzwarth, and T. J. Kippenberg, "Dispersion engineering of thick high-Q silicon nitride ring-resonators via atomic layer deposition," Opt. Express **20**(25), 27661–27669 (2012).
9. W. Zeru, C. Yujie, Z. Tianyou, S. Zengkai, W. Yuanhui, X. Pengfei, Z. Yanfeng, and Y. Siyuan, "Design and optimization of optical modulators based on graphene-on-silicon nitride microring resonators," J. Opt. **19**, 045801 (2017).
10. A. Z. Subramanian, E. Ryckeboer, A. Dhakal, F. Peyskens, A. Malik, B. Kuyken, H. L. Zhao, S. Pathak, A. Ruocco, A. De Groote, P. Wuytens, D. Martens, F. Leo, W. Q. Xie, U. D. Dave, M. Muneeb, P. Van Dorpe, J. Van Campenhout, W. Bogaerts, P. Bienstman, N. Le Thomas, D. Van Thourhout, Z. Hens, G. Roelkens, and R. Baets, "Silicon and silicon nitride photonic circuits for spectroscopic sensing on-a-chip," Photon. Res. **3**, B47–B59 (2015).
11. F. T. Dullo and O. G. Hellesø, "On-chip phase measurement for microparticles trapped on a waveguide," Lab Chip **15**(19), 3918–3924 (2015).
12. B. Agnarsson, S. Ingthorsson, T. Gudjonsson, and K. Leosson, "Evanescent-wave fluorescence microscopy using symmetric planar waveguides," Opt. Express **17**(7), 5075–5082 (2009).

#303400 https://doi.org/10.1364/OE.25.027678
Journal © 2017 Received 21 Aug 2017; revised 21 Sep 2017; accepted 29 Sep 2017; published 25 Oct 2017

Optics EXPRESS

13. B. Agnarsson, A. B. Jonsdottir, N. B. Arnfinnsdottir, and K. Leosson, "On-chip modulation of evanescent illumination and live-cell imaging with polymer waveguides," Opt. Express **19**(23), 22929–22935 (2011).
14. H. M. Grandin, B. Städler, M. Textor, and J. Vörös, "Waveguide excitation fluorescence microscopy: A new tool for sensing and imaging the biointerface," Biosens. Bioelectron. **21**(8), 1476–1482 (2006).
15. A. Hassanzadeh, M. Nitsche, S. Mittler, S. Armstrong, J. Dixon, and U. Langbein, "Waveguide evanescent field fluorescence microscopy: Thin film fluorescence intensities and its application in cell biology," Appl. Phys. Lett. **92**, 233503 (2008).
16. B. Agnarsson, A. Lundgren, A. Gunnarsson, M. Rabe, A. Kunze, M. Mapar, L. Simonsson, M. Bally, V. P. Zhdanov, and F. Höök, "Evanescent Light-Scattering Microscopy for Label-Free Interfacial Imaging: From Single Sub-100 nm Vesicles to Live Cells," ACS Nano **9**(12), 11849–11862 (2015).
17. M. J. Levene, J. Korlach, S. W. Turner, M. Foquet, H. G. Craighead, and W. W. Webb, "Zero-mode waveguides for single-molecule analysis at high concentrations," Science **299**(5607), 682–686 (2003).
18. R. Diekmann, O. I. Helle, C. I. Oie, P. McCourt, T. R. Huser, M. Schuttpelz, and B. S. Ahluwalia, "Chip-based wide field-of-view nanoscopy," Nat Photonics **11**, 322 (2017).
19. F. T. Dullo, J. C. Tinguely, S. A. Solbo, and O. G. Helleso, "Single-Mode Limit and Bending Losses for Shallow Rib Si3N4 Waveguides," IEEE Photonics J. **7**, 1–11 (2015).
20. H. R. Philipp, "Optical Properties of Silicon-Nitride," J. Electrochem. Soc. **120**, 295–300 (1973).
21. C. Guo, M. Kong, W. Gao, and B. Li, "Simultaneous determination of optical constants, thickness, and surface roughness of thin film from spectrophotometric measurements," Opt. Lett. **38**(1), 40–42 (2013).
22. D. F. G. Gallagher and T. P. Felici, "Eigenmode expansion methods for simulation of optical propagation in photonics - Pros and cons," Integrated Optics: Devices, Materials, and Technologies VII **4987**, 69–82 (2003).
23. Y. Fu, T. Ye, W. Tang, and T. Chu, "Efficient adiabatic silicon-on-insulator waveguide taper," Photon. Res. **2**, A41–A44 (2014).
24. F. Prieto, B. Sepulveda, A. Calle, A. Llobera, C. Domínguez, A. Abad, A. Montoya, and L. M. Lechuga, "An integrated optical interferometric nanodevice based on silicon technology for biosensor applications," Nanotechnology **14**, 907 (2003).
25. C. E. Aitken, R. A. Marshall, and J. D. Puglisi, "An oxygen scavenging system for improvement of dye stability in single-molecule fluorescence experiments," Biophys. J. **94**(5), 1826–1835 (2008).

1. Introduction

Photonics integrated circuits (PICs) based on high refractive index contrast (HIC) between the core and the cladding has attracted significant research attention during the last decade [1–10]. The HIC enables tight confinement of the light inside the waveguide, enabling ultra-compact waveguide structures with small bend radii. These properties of HIC are used to fabricate high-density PICs and integrated optical functions such as optical modulators, switches, and arrayed waveguides with a small footprint. Spiral waveguide geometries in HIC waveguides are used to significantly increase the interaction length between the sample and the evanescent field of the waveguide [1] opening opportunities to develop, e.g., on-chip Raman spectroscopy [1] and on-chip optical coherence tomography (OCT) [2]. In addition, by fabricating HIC waveguides with a core thickness of 100-200 nm, the intensity of the evanescent field can be greatly increased. Consequently, HIC waveguide platforms provide high sensitivity when used for optical sensors (chemical, gas and biological) [3, 4]

Different materials have been explored to fabricate HIC waveguide platforms. For infrared wavelengths, silicon waveguides (n = 3.5) using silicon-on-insulator technology are commonly used. For the visible regime, materials such as tantalum pentoxide (Ta_2O_5), titanium pentoxide (TiO_2) and silicon nitride (Si_3N_4) have been utilized. Among the explored HIC materials within visible wavelengths, Si_3N_4 has attracted the maximum attention due to its suitable material properties and the compatibility of Si_3N_4 fabrication process with standard CMOS fabrication line. The suitable material property includes transparency in visible wavelength, low absorption and high refractive index contrast. Exhibiting a refractive index of around 2 at the visible regime, the HIC with the substrate/cladding (typically SiO_2, n = 1.46) enables integrated functions with a small footprint, which is not possible with materials exhibiting lower refractive index contrasts. Various applications have been developed both in linear [4, 6] and non-linear optics [7] using Si_3N_4 platform. The Si_3N_4 waveguide has been employed to develop different integrated optical functions such as ring resonators [8], modulators [9], switches [9], sensors [3], spectroscopy [10] and waveguide trapping [11]. Being transparent with low auto-fluorescence and low absorption in the visible range further makes Si_3N_4 compatible with fluorescence techniques for bio-imaging. In

Optics EXPRESS

addition, the compatibility of Si_3N_4 with standard CMOS fabrication lines is able to deliver high volume production of photonic chips, decreasing production costs. Low-loss Si_3N_4 waveguide platforms have been reported using CMOS fabrication compatible process [4–6] and the foundry services for Si_3N_4 platforms became commercially available in recent years.

In this work, we report the usage of Si_3N_4 waveguide platform for integrated optical microscopy for live cell imaging applications. The previous reports [12–18] on integrated optical microscopy employed different core materials including both high and low refractive index contrast materials. Si_3N_4 platform has not been explored for fluorescence microscopy of living cells. As Si_3N_4 is turning out to be a preferred HIC material at visible wavelengths, a systematic investigation of the suitability of Si_3N_4 waveguide platforms for bio-imaging applications is beneficial. In this paper we designed, fabricated and characterized Si_3N_4 rib waveguides to possess single mode behaviour at visible wavelengths that are used in fluorescence imaging (488-660 nm). We also simulated the bend loss and adiabatic tapering length of shallow Si_3N_4 rib waveguides (2-8 nm rib height) for visible wavelengths. The simulation parameters are compared to experimental measurements. Finally, the low-loss Si_3N_4 waveguide platform is shown to be biocompatible with the imaging of living cells.

2. Si_3N_4 waveguide platform for TIRF microscopy

High-specificity, high-resolution and live-cell compatibility made fluorescence microscopy a vital tool in modern bio-medical imaging and diagnosis. The fluorophores specifically bind to the biological target providing high-contrast imaging of the intra-cellular structures with low background. To further reduce the background signal, total internal reflection fluorescence (TIRF) microscopy can be used. Contrary to epi-fluorescence where the entire cell is illuminated, TIRF microscopy exposes only a thin section of the cells through the evanescent field. As the evanescent field decays exponentially at the interface, only a thin, typically 100-200nm section away from the surface is illuminated. Consequently, TIRF microscopy provides a high signal-to-noise ratio by reducing the background signal. TIRF microscopy has found applications for imaging targets in close proximity to the cell membrane, such as cell membrane trafficking and focal adhesion points.

The evanescent field is commonly generated using a specialized high numerical aperture (N.A.) and high magnification TIRF objective lens. By this method, the dimension of the illuminated region is given by the magnification of the objective lens, which also collects the emitted fluorescence. This limits the field-of-view down to around 100 x 100 μm^2. Another way of setting up an evanescent field for TIRF microscopy is by using optical waveguides [12, 14, 15, 17,18]. In waveguide chip-based microscopy, the illumination and collection light paths are efficiently decoupled, opening several opportunities for bio-imaging. As the evanescent field is generated along the entire length of the waveguide, a low magnification objective lens can be employed to acquire TIRF images over a large field-of-view of even millimetre range [18]. Waveguide-based TIRF exhibits thus many advantages compared to conventional TIRF systems, such as a compact and user-friendly set-up (e.g. in-coupling can be provided by optical fiber), low cost as mass produced chips circumvent the expensive TIRF lens, the aforementioned flexibility at the collection path for large field of view imaging, and easy multi-color TIRF imaging at multiple wavelengths without additional optical alignment and mechanical adjustments.

Recently it was shown that the light intensities generated by the waveguide chip made of HIC material enable blinking of single molecules for super-resolution microscopy techniques [18]. The high intensity in the evanescent field was generated by fabricating thin waveguides (150 nm in thickness) made of high refractive index contrast (HIC) material such as Si_3N_4. A Si_3N_4 waveguide chip was used to demonstrate two different optical nanoscopy techniques, one based on *d*STORM (direct stochastic optical reconstruction microscopy) and another based on ESI (entropy-based super-resolution imaging). Waveguide chip-based nanoscopy displayed an optical resolution of 47 nm using a 60x/1.2NA objective, and by simply

Optics EXPRESS

changing the collection objective lens to 20x, super-resolution imaging (with a resolution of 139 nm) was obtained over an extra-ordinary large f-o-v of 0.5 x 0.5 mm^2 [18]. Multi-color waveguide chip-based *d*STORM visualized the connection of the actin cytoskeleton and plasma membrane fenestrations on liver sinusoidal endothelial cells. As compared to chip-based *d*STORM, chip-based ESI provides higher temporal resolution but lower spatial resolution. Waveguide based ESI was performed by modulating multi-mode interference (MMI) patterns of the guided light within the waveguide..MMI are typically known as an issue at waveguide-based illumination, especially when using waveguides with dimensions to accommodate cells (10-50 μm wide). The interference pattern provides then an uneven illumination of the surface with dark regions within the imaging field. A reduction in the effect of the MMI patterns was demonstrated by subsequently exciting sub-sets of modes by scanning the input coupling objective along the input facet of wide waveguides, and then averaging the mode patterns out [18]. A drawback of this approach, in addition to the need for delicate equipment for mode averaging, is the obvious reduction in temporal resolution associated with the mode averaging procedure, limiting the technique to fixed cells. Here, we show a different approach to achieve single mode (and thus uniform) illumination, by using both waveguide bends to filter out higher order modes and then adiabatically tapering of single mode waveguides up to dimensions suitable for fluorescence imaging. This strategy further strengthens advantages of waveguide-TIRF previously mentioned in this section.

2.1 Simulations

Simulations were performed to optimize the waveguide parameters such that uniformity and high intensity in the evanescent field is obtained. In fluorescence microscopy, laser lines spanning the whole visible spectrum are commonly used. We based the waveguide simulations on the most typical excitation wavelengths 488 nm, 561 nm and 660 nm. In order to achieve uniform illumination, the waveguide geometry was optimized to guide only the fundamental mode at the wavelengths of interest. The HIC of Si_3N_4 together with the requirement of visible wavelengths puts stringent conditions on the waveguide geometry to achieve the single mode condition. Compared to slab waveguides, challenged waveguide geometries (strip and rib) provide higher intensity in the evanescent field. Figure 1(a) shows the schematic diagram of a strip and rib waveguide. For the strip geometry, the single mode condition for Si_3N_4 is achieved with a sub-micron wide waveguide [6], which would require the need of projection exposure systems as steppers, electron-beam lithography or deep-UV lithography. However, the rib geometry should maintain single mode behaviour for wider waveguide geometry, e.g., 1-1.5 μm, making the fabrication process feasible with conventional photolithography and thus less demanding. Moreover, as cells are 10-25 μm in size, it is preferred to fabricate wide waveguides (>25 μm) with single mode condition. A single mode rib waveguide is therefore adiabatically tapered to provide uniform excitation over large areas. Two different designs are proposed (design A and B, as depicted in Fig. 1(b), one being a straight geometry (A) and the other including a bend section (B). As higher order modes have much higher bend losses, bend section was used to filter out higher order modes and thus ensuring single mode condition.

Simulations to determine the single mode geometry were performed using the film mode-matching (FMM) solver of the commercial software Fimmwave (Photon Design, UK). The FMM solver, a numerical technique, divides a waveguide geometry into vertical slices which are uniform laterally but multi-layered vertically. A 2D model is then composed of the Maxwell solutions found for the 1D TE (transverse electric) and TM (transverse magnetic) polarization modes of each vertical slice, with the mode amplitude obtained through the continuity of the tangential fields at the slice interface and boundary conditions. By using the FMM solver, single mode conditions were determined by calculating the largest rib height for a given width and slab height where no solution for the first-order mode could be found. As the single mode condition geometry is polarization dependent, the results differ depending on

Optics EXPRESS

the electric field's orientation. TM modes of shallow rib waveguides exhibit a hybrid polarization character with the strength of the resulting minority fields varying with geometry. Approximations to this character mostly result in erroneous results. This work will only discuss results for transverse electric (TE) modes, which do not present such behaviour. Leakage losses of TM modes and their influence on, e.g., bending losses have been discussed previously [19].

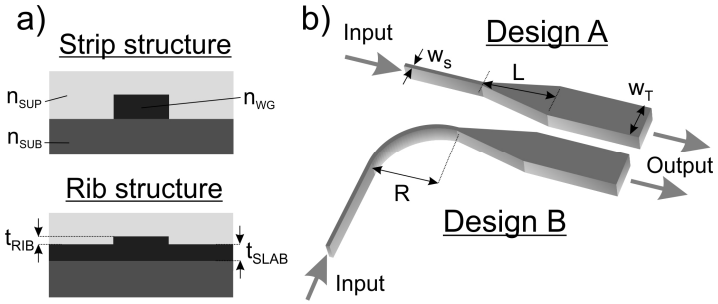

Fig. 1. a) Cross-section scheme of strip vs. rib waveguide geometry. n_{SUP}, n_{WG}, n_{SUB}: refractive indexes of superstrate, guiding material and substrate, respectively. t_{RIB}, t_{SLAB}: thicknesses of rib and slab regions. b) Top view scheme of waveguide designs demonstrating tapering of the waveguide width (design A and B) and bend structure (design B). w_S: start width, w_T: tapered width, L: taper length, R: bend radius.

As start parameters, a waveguide width of 1.5 µm was taken as a lower reproducible limit of the contact photolithography process, avoiding the more demanding scanning/stepping or e-beam processing techniques. Simulations suggested that a Si_3N_4 thickness of 150 nm (rib and slab thickness, $t_{RIB} + t_{SLAB}$) leads to an evanescent field of around 150 nm penetration depth. The curves in Fig. 2(a) display the results for single mode condition calculations for waveguides with a SiO_2 cladding at 488 nm, 561 nm and 660 nm. Refractive indexes taken for Si_3N_4 were 2.037, 2.021 and 2.007 [20], and for SiO_2 1.482, 1.479 and 1.475 at 488 nm, 561 nm and 660 nm, respectively [21]. Single mode condition simulations in Fig. 2(a) display that as the total thickness of the waveguide decreases, a smaller rib height t_{RIB} is required to keep the single mode condition. Intuitively, the rib height to maintain the single mode condition will also decrease with decreasing wavelengths. A core thickness ($t_{RIB} + t_{SLAB}$) of 150 nm was chosen for the fabrication. The simulation results indicate that for this total thickness of 150 nm, a rib height of 4 nm (t_{RIB}) and slab height of 146 nm (t_{SLAB}) would provide single mode condition for a 1.5µm wide, SiO_2 cladded waveguide at the three considered wavelengths. These dimensions will be taken into consideration for the rest of this work.

Adiabatic taper length

After simulating the parameters for single mode condition for a 1.5 µm wide waveguide, further simulations were carried to determine the adiabatic tapering length. An increase in the width of the waveguide will typically enable higher order modes to be guided. By tapering the waveguide slowly and adiabatically, the guidance of only the fundamental mode is preserved. The adiabaticity is a function of the initial and the final waveguide widths (w_S and w_T), the taper length (L), and the taper shape, as schematically represented in Fig. 1(b). The commercial software Fimmprop™, a 3D modelling expansion to the Fimmwave software, was used for the taper simulations. Fimmprop™ is based on the EigenMode Expansion Method, a fully vectorial, bi-directional algorithm where the main approximation is the chosen number of propagating and radiation modes for a given geometry [22]. The adiabaticity parameter shown in Figs. 2(b) and 2(c) is defined as the percentage of the guided light present at the zero-order mode. A tapered single mode waveguide requires adiabaticity values close to 100%. The adiabaticity was determined by computing a number of modes

Optics EXPRESS

accepted at the end width of the waveguide and analysing the power distribution among them according to a taper length L. The taper profile can assume different shapes, e.g., linear, exponential or Gaussian. A linear shape was chosen based on published literature [23] pointing towards a better efficiency compared to the Gaussian and exponential shapes and better stability compared to the parabolic shapes. Convergence tests were performed for the considered number of modes. Figure 2(b) displays the results for the three different end widths at 660 nm. Results suggest 99% adiabacity from a start width w_S = 1.5 µm to an end width w_T = 12.5 µm with a taper length around L = 500 µm. The same efficiency for the end width w_T = 25 µm was achieved with the taper length L = 2000 µm and a taper length of over 4000 µm was required for the end width w_T = 50 µm. In order to undergo a compromise with the propagation losses and the structure size, the taper parameters for the experiments were set as w_T = 25 µm and L = 2000 µm. Figure 2(c) displays the minor difference in the taper efficiency for the three utilized wavelengths (over 98% for all wavelengths at L = 2000 µm) at the set parameters.

Bend losses

A Fimmprop model was used to estimate bend losses for a rib waveguide as a function of the bend radius (R). The model first considers a lossless straight section, which is then bent 90°. The power loss is estimated at the structure's output. Figure 2(d) displays the simulation results, where a significant difference in the bend losses between the three wavelengths is evident. For a bend radius of R = 2000 µm, the bend losses are below 1 dB at 561 nm and 488 nm while being around 3.5 dB at 660 nm. Transition losses are also strongest at longer wavelengths, with a model at 660 nm estimating them to be less than 0.1dB at R = 3000 µm and below 0.25dB at R = 500 µm.

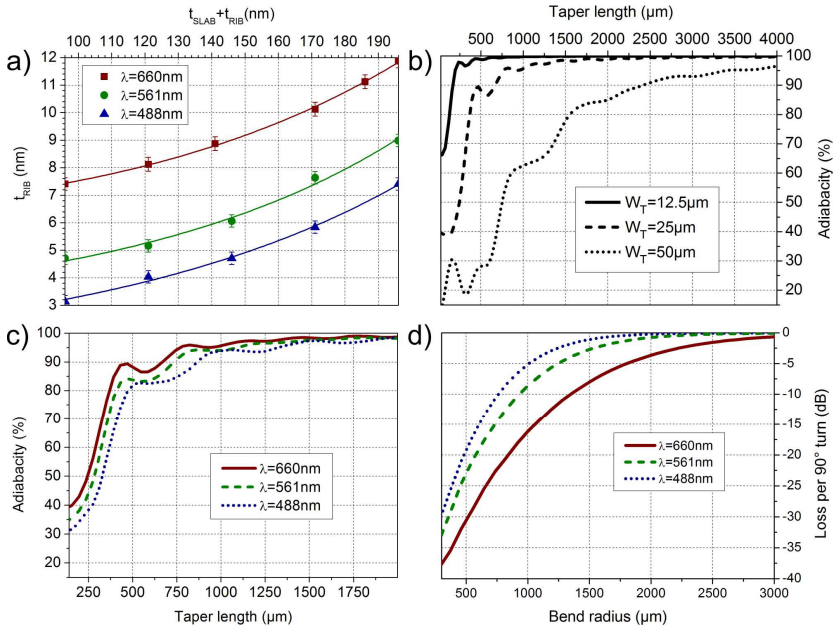

Fig. 2. a) Single mode condition simulations for TE polarized modes, 1.5µm rib width, 1.5µm SiO_2 cladding. Single mode behaviour expected below the fitted line for the given wavelength and geometry. b) Taper adiabaticity simulation, w_S = 1.5 µm to different end widths, λ = 660nm. c) Taper adiabaticity simulations, w_S = 1.5 µm to w_T = 25 µm. d) Simulation of power loss after a 90° bend as a function of bend radius.

Optics EXPRESS

2.2 Fabrication and characterization of the waveguides

Fabrication

Waveguide chips were produced at the Institute of Microelectronics Barcelona (IMB-CNM, Spain). Silica layer with a thickness of 2 µm was first grown thermally on a silicon chip, followed by the deposition of Si_3N_4 layer using low-pressure chemical vapor deposition (LPCVD) at 800°C. Standard photolithography was employed to define the waveguide geometry using photoresist, and reactive ion etching (RIE) used to fabricate a waveguide rib of given height. The remaining photoresist was removed, and finally a 1.5-2 µm thick top cladding layer deposited by plasma-enhanced chemical vapor deposition (PECVD) at 300°C. To seed the cells at specific imaging areas, the top cladding was removed using RIE and wet etching. The details of the fabrication optimization and process can be found elsewhere [24]. ·All waveguides were fabricated with a total Si_3N_4 thickness of 150 nm and 4 nm rib height. The initial width of the waveguide was 1.5 µm, later adiabatically tapered out to 25 µm. The bend radius was set to 2 mm.

Characterization

The manufactured parameters were characterized using scanning electron microscopy and a surface profiler. The surface profiler measurements verified an average rib height of 4.0 nm within the noise level of the system (0.6 nm). Scanning electron microscopy measurements indicated a possible variation of ± 0.1 µm over the specified 1.5 µm wide width.

Single mode conditions

Optical waveguides of 1.5µm width were characterized for single mode behaviour at the three wavelengths considered for the simulations. When the fundamental mode is excited in a waveguide, the resulting scattered light will appear homogenous and stationary for all possible coupling positions. If higher order modes are present, multi-mode interference (MMI) can be observed, and the scattered light along the waveguide will be modulated. To investigate this, the input coupling objective lens was scanned along the width of the waveguide using a piezo translation stage and image sequences of the scattered light were captured using an upright microscope. The experimental set-up is shown in Fig. 3. For waveguides only supporting the fundamental mode, only a straight pattern can be observed (Visualization 1). For waveguides that support higher order modes, MMI as an undulated pattern is visible (Visualization 2). Figures 4(a) to 4(c) shows scattered light from a waveguide designed for 1.5 µm width at three different wavelengths. These geometries indicate single mode behaviour at λ = 660 nm, while λ = 561nm and λ = 488 nm appear to be supporting higher order modes. This is particularly visible at λ = 488 nm, Fig. 4(c), where the undulation pattern in the guided light can be observed. Despite being in disagreement with the simulation results, the multimode behaviour at shorter wavelengths might be explained due to slight variation in the parameters of the fabricated waveguides (width and effective refractive index).

Waveguides were adiabatically tapered using both designs A and B as represented in Fig. 1(b) (w_S = 1.5 µm, w_T = 25 µm, L = 2 mm, R = 2 mm). The tapered waveguides following design A, Figs. 4(d)-4(f), and design B, Figs. 4(g)-4(i), were inspected for single mode condition at the three wavelengths. Figure 4(d) shows that 25 µm wide waveguide is still single moded at λ = 660 nm as the scattered light appears uniform. However, at λ = 561nm, Fig. 4(e), a dark band caused by multi-mode interference is visible in the scattered image. As expected, Fig. 4(f) shows that decrease of the wavelength to 488 nm results in even stronger MMI patterns.

Optics EXPRESS

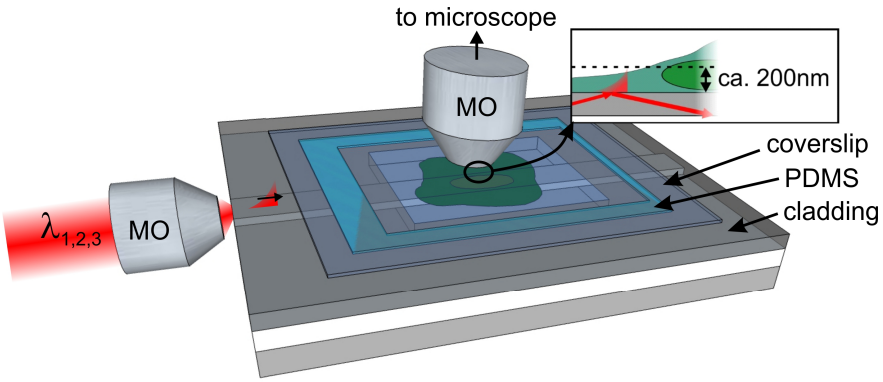

Fig. 3. Schematic diagram of the experimental setup. Imaging area at cladding is opening allowing for specimen contact to waveguide surface. Inset: approximate penetration depth of evanescent field. λ_1, λ_2, λ_3: guiding/excitation wavelengths, MO: microscope objective.

Higher order modes have several orders of magnitude higher bend losses as compared to the fundamental mode. This can be taken advantage of to filter out guided higher order modes by adding bend sections as schematized in Fig. 1(b), design B. Structures were designed where a straight 1.5 µm wide waveguide was first bend (R = 2 mm) and then tapered to 25 µm. While Visualization 3 exhibits the scattered light from a 488 nm laser in the straight 1.5 µm wide waveguide where multimode interference is clearly visible, Visualization 4 shows scattered light from the same waveguide after a bend with 2 mm radius suggesting single mode behaviour. Figures 4(g)-4(i) depict the scattered light from a 25 µm wide waveguide having the taper after a bend with a radius of 2 mm for the three different wavelengths. Comparing Figs. 4(e)-4(f) to Figs. 4(h)-4(i), it is evident that the previously observed interference patterns are removed by the bend structures (i.e by design B).

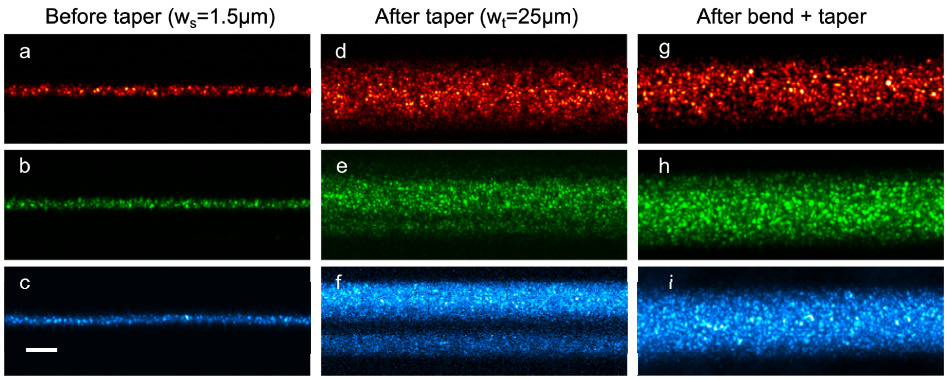

Fig. 4. Optical image of the scattered light from a waveguide at three wavelengths, (a, d, g): 660nm; (b, e, h): 561 nm and (c, f, i): 488 nm. a) to c) straight 1.5 µm wide waveguide. Multimode behaviour is observed for b) and c). d) to f): Adiabatic tapering to 25 µm width observed at d) while multimode behaviour was carried on at e) and f). g) to i): Bend section with 2mm radius preceding the taper structure removing multimode interference. Scalebar: 5 µm. Associated Visualization 1, Visualization 2, Visualization 3, and Visualization 4.

Loss measurement

The propagation losses of the waveguide for three wavelengths were measured using scattering analysis. Images of scattering from guided light were captured with subsequent translation of an upright microscope and post-processed to remove saturated pixels. Saturated pixels originate from strongly scattered light representing fabrication imperfections. An average value for each scattered image was used to track the decaying intensity of the

Optics EXPRESS

propagating light as a function of the waveguide length. The result was plotted on a log-scale with the linear fit decay as the estimate for the propagation loss. Four different measurements for each wavelength and polarization state were performed for waveguides with lengths between 1 and 2 cm, the weighted averages being shown in Table 1. The propagation loss of the Si_3N_4 was less than 1 dB/cm at 660 nm wavelength (both polarizations) and still reasonably low at 561 nm (2-2.5 dB/cm). However, the propagation loss at 488 nm was very high for both polarizations (10 dB/cm). It is very likely that the high loss at shorter wavelengths (i.e. 488 nm) is related to material absorption, visible as autofluorescence. The autofluorescence has a similar exponential increase of its intensity if moving from 660 nm to 488 nm.

Table 1. Propagation loss for 1.5 µm wide Si_3N_4 waveguides. Single values averaged from four different waveguides. The measurement uncertainty is estimated to one digit.

	TM	TE
488 nm	10.5	10.2
561 nm	1.9	2.6
660 nm	0.7	0.5

Bend losses were measured by comparing the intensity at the output facet of different waveguides. To minimize systematic errors, only waveguides on the same chip were compared. The structures contain both straight waveguides (no bends) and bend designs of different radii as shown in Fig. 5(a). The bend designs were shaped as a composite of two + 60° and two −60° curvatures. The straight waveguide acts as a reference for comparing the bend losses associated with the different bend radii, assuming the excess loss measured from the bending itself and the extra propagation loss associated with the extra arc-length of the bend sections. The output light was coupled out of the waveguides and captured by a 20x NA0.4 objective lens. An iris was placed at the objective focal point to filter out any unguided light, and finally the light was directed to an optical power meter. Figure 5(a) plots the simulated and the measured bend losses for the bend geometries in Fig. 5(b). For a bend radius of 2 mm at 561 nm and 660 nm wavelengths, the bend losses measured experimentally were similar to the values predicted by the simulation. Discrepancies on the measured and the simulated bend losses were obtained for the short bend radius, i.e. (500 µm) at all wavelengths. For a rib waveguide, the Si_3N_4 slab beneath can still guide light leaking out from the waveguide. For shallow rib waveguides as used in this work, part of the light leaking out at the sharp bends (e.g. 500 µm) is being guided by the slab beneath and eventually re-coupled onto the straight section after the bend. This effect was prominent for sharp bends and also at 488 nm wavelength, thus accounting for the higher discrepancies at 488 nm.

Optics EXPRESS

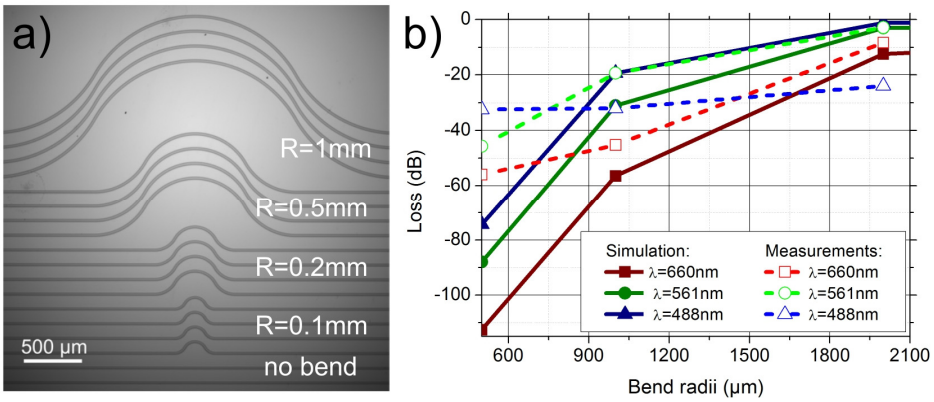

Fig. 5. a) Waveguide design for measurement of bend losses. Microscope image shows the different waveguide test structures with no bend and increasing bend radii. b) Measurements vs. simulations for a bend loss structure as represented in a).

3. Chip based fluorescence imaging of fixed and live cells

3.1 Experimental set-up

The setup was built around a modular upright microscope from Olympus (BXFM), see Fig. 3. The microscope body was mounted on two linear motorized translation stages, providing freedom to move the microscope. The waveguide chip was held by a vacuum chuck mounted on a multi-axis flexure stage (Thorlabs, RBL 13D). Light from three lasers sources (660 nm Cobolt Flamenco, 561 nm Cobolt Jive and 488 nm Oxxious LBX 488) was combined and coupled into the waveguide chip. The laser beams were individually expanded and collimated to fit the back aperture of the coupling objective lens (Olympus NPlan 50x NA0.5), which focussed the light onto the input facet of the waveguide. The coupling objective lens was mounted on a piezo stage (Melles Griot, NanoMax-HS) to allow for fine-tuning of the input coupling. The light coupled into the waveguide is guided to the imaging region. The cladding on the imaging area was removed to allow the specimen to come in direct contact with the waveguide surface and thus the evanescent field. The fluorescence is excited by the evanescent field and the emitted signal is captured by a high N.A. objective lens (Olympus 60x NA1.2) and filtered through lowpass (AHF660, AHF561, Edmund 488) and bandpass filters before the signal is imaged onto a sCMOS camera (Hamamatsu Orca flash v3). Post processing of the image data was done using the open source software ImageJ.

3.2 Sample preparation

Waveguide chips were fitted with a custom made micro-chamber to host cells and aqueous image buffer. The micro-chambers were fabricated using polydimethylsiloxane (PDMS) which was spin coated on the bottom of a petri dish to achieve an approximately 130 µm thick homogeneous layer. After curing, the micro-chambers were cut to size with a scalpel and placed on the chip using a tweezer. PDMS will adhere to both the waveguide and cover glass coming on top of it, creating a hermetic chamber.

Human Merkel carcinoma cells (MCC13) were seeded directly on the waveguide surface and left to grow for 48 hours inside an incubator. The cells were fixed using 4% paraformaldehyde (PFA) for 10 minutes at room temperature (RT). Cell membrane permeabilization was performed using 0.1% Trition X-100 at RT. To reduce unspecific binding of fluorophores on the waveguide surface, the chip was incubated with 5% bovine serum albumin (BSA) for 20 minutes at RT. The microtubules network was stained for 45 minutes with Alexa488 a-tubulin (Termofisher, #MA138000A488) at a concentration of 1/400 in 5% BSA at RT. The plasma membrane was stained for 20 minutes at RT using

Optics EXPRESS

CellMask deep red (Termofisher, #C10046) (CMDR), the stock solution diluted to 1/1000 in phosphate buffered saline (PBS). Each step in this protocol was followed by three gentle rinsing steps using PBS buffer. The PBS-based imaging media contained an enzymatic oxygen scavenging system [25] to reduce photobleaching of the fluorophores.For live cell imaging, human trophoblast cells (HTR-8) were grown on the waveguide inside an incubator for 48 hours. The plasma membrane was stained using CellMask green (Termofisher, #H32714) at a concentration of 1/1000 in PBS for 20 minutes. The chip was gently washed with live cell buffer media (Termofisher, #21875091). The chambers were filled with live cell imaging buffer (Termofisher, #A14291DJ) and imaged within 30 minutes after staining.

3.3 Imaging of fixed and live cells

The tapered waveguide (25 μm) using design B, Fig. 1(b), was used for bio-imaging experiments. Fixed MCC13 cells were imaged sequentially for the red (660 nm) and green (561 nm) wavelengths. To image the plasma membrane stain, 0.3 mW laser power at 660 nm was measured on the back aperture of the objective lens used for coupling light into the waveguide chip. After consideration of the different loss contributions from coupling, bending and propagation, the guided power at the imaging region was roughly estimated to be in the order of 4-10 μW. Similarly, the microtubules were imaged using 5 mW of the 488 nm laser at the back aperture, leaving roughly around 0.5-1 μW of this wavelength at the imaging region. Given the high refractive index material, we estimate that around 10% of the guided power is available in the evanescent field. For each channel, 100 images were acquired with an integration time of 10 ms. An average of these images was used to further improve the image contrast, which can be seen in Figs. 6(a)-6(d). The position of the waveguide edges is indicated with white dashes in Figs. 6(a)-6(b), and zoomed regions indicated by white squares are shown in Figs. 6(c)-6(d). The evanescent field excitation of the waveguide gives high optical sectioning, generating images with high contrast and low background. The effects of shadows stemming from waveguide imperfections are minimal, but can be barely seen towards the right side of Fig. 6(a).

For live cell imaging, the HTR-8 cells were seeded and grown on the Si_3N_4 chip. The chip seeded with cells was placed inside the incubator for 48 hours. Live HTR-8 cells were imaged within 30 minutes after staining was completed. Input power of 60 mW of 488 nm laser was used at the back aperture of the coupling objective lens, which leaves around 15-30 μW guided power at the imaging region. A stack of images was acquired under continuous illumination for 3.6 minutes with 100 ms exposure time. The resulting movie, shown at Fig. 7 and Visualization 5, indicates a healthy environment for cell movement on the waveguide surface. Slight photobleaching was observed corresponding to around 25% decrease of the fluorescence intensity after 3.6 minutes of continuous illumination.

Optics EXPRESS

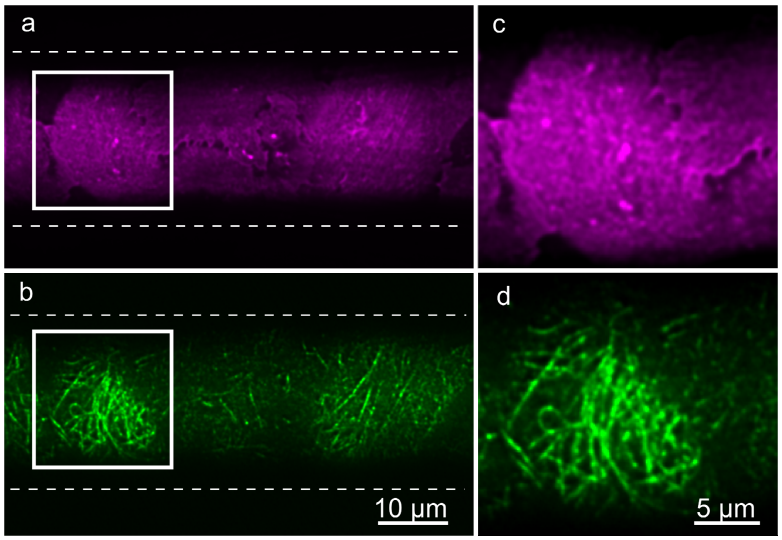

Fig. 6. a), b) MCC13 cells stained for plasma membrane (CellMask deep red) and tubulin (Alexa 488 anti-Tubulin), fluorescence excited through a 25 µm wide waveguide. The cells are distributed homogeneously on the chip, the center of the waveguide being indicated with dotted lines. c), d) are the regions indicated with a white box in a) and b). The cells are evenly illuminated at this position on the waveguide.

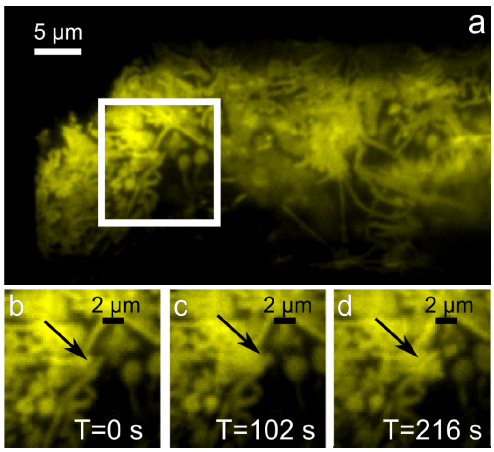

Fig. 7. HTR-8 cells stained for plasma membrane and kept alive in live-cell imaging media during the measurement. a) A frame from the movie (Visualization 5) shows several cells clustered together on the 25 µm wide waveguide. b) to d) Movement in the cell membrane can be seen over 3.6 minutes.

4. Conclusion and discussion

In this work we have systematically studied, developed and characterized a Si_3N_4 waveguide platform for bio-imaging applications. The fabrication of the Si_3N_4 platform is compatible with standard CMOS fabrication pilot lines. The high refractive index of the Si_3N_4 waveguide platform was exploited to generate a high intensity in the evanescent field by fabricating thin waveguides (150 nm). It was shown that Si_3N_4 waveguides provide biocompatible substrates where live cells can be grown and continuously imaged with low photo-toxicity, similar to the conventional glass cover slip approach.

Simulations backed up by experimental results studied the waveguide geometry to provide uniform illumination over wider widths (25 µm). A narrow (1.5 µm) and shallow rib

Optics EXPRESS

waveguide (4 nm) was adiabatically tapered to a wider width (25 μm) at the imaging region. To ensure single mode behavior at the imaging area, bend geometry was used. As higher order modes have much higher bend losses than the fundamental mode, it was demonstrated by bending the waveguide that higher order modes can be filtered out ensuring uniform illumination over wide waveguides (25 μm) at all studied wavelengths (488, 561 and 660 nm). In order to provide a uniform excitation, single mode waveguides are not always sufficient. Waveguide imperfections, dust particles, or other highly scattering or absorbing elements interfering with the guided mode may appear in the images as dark band shadows. The fabrication steps can be further optimized to reduce such artifacts. This effect is less prominent if the objects interfering the guided mode offer a less refractive index contrast, e.g., cells as shown in this work.

Propagation losses were measured for straight and bend sections, being low at longer wavelengths but showing a strong increase towards shorter wavelengths (488 nm). The propagation loss of less than 1 db/cm at 660 nm while it is around 10 db/cm at 488 nm. The high propagation losses at 488 nm seem to correlate with stronger auto-fluorescence at 488 nm wavelengths. Future optimization of the fabrication steps to reduce the auto-fluorescence at 488 nm will be carried out.

To fully exploit the capabilities of chip-based microscopy to provide large field of view TIRF illumination, future work will focus on extending the waveguide geometry laterally even further to accommodate uniform TIRF illumination suitable for imaging with low NA objectives. This will open up the possibility to study enormous populations of cells in TIRF mode in real-time enabling high-throughput TIRF imaging. Development of on-chip TIRF microscopy is also flexible towards implementations with other integrated systems, such as microfluidics and on-chip sensing, particle tracking and trapping and super-resolution microscopy.

Funding

European Research Council, project number 336716.

Acknowledgments

Authors acknowledge Martin Ingvaldsen for the code at scattering analysis and Rajwinder Singh for the assistance with sample preparations. This work has made use of the Spanish ICTS Network MICRONANOFABS partially supported by MEINCOM.

4

On-chip localization microscopy

In chapter 2, TIRF diffraction-limited imaging was explored using chip-based illumination. The waveguide platform was tested for bio-applications for both fixed and living samples. Furthermore, different strategies to achieve uniform illumination was discussed.

In this chapter, the application of waveguide-based imaging is extended towards super-resolution TIRF microscopy, using the SMLM technique dSTORM [19, 20]. Also, the intrinsic MMI patterns are used together with a statistical reconstruction algorithm to perform on-chip fluctuation nanoscopy using ESI [35].

4.1 Introduction

The working concepts of dSTORM were discussed in section 2.3.3. For brevity, the dSTORM principle utilizes the natural occurring dark-states of the fluorophore. During normal fluorescence, the electronic energy states are circulating between the ground state and the excited singlet states. However a transition to the triplet state is also likely to occur, and from here the chance of entering long-lived dark states can be increased. dSTORM utilize a chemical

reduction of the triplet state, i.e. an electron is absorbed by the fluorescent molecule from the image buffer. The result is a temporary dark state having a lifetime of seconds to minutes. The return to the ground state can happen spontaneously with the absorption of oxygen, or with UV radiation. If enough fluorophores recite in the dark state, the sample can be observed to be blinking with separable emitters, allowing for the precise localization of the single-molecule.

Signal to noise ratio is a key consideration in localization microscopy such as dSTORM. Since the signal that is detected on the camera is coming from a single-molecule it is dim, and any background signal will reduce the localization precision and thus the resolution of the reconstructed image, as can be seen in (2.7). In a conventional dSTORM microscope, the SNR is maintained by either using TIRF illumination or HiLO illumination [32]. HiLO illumination is achieved when the total internal reflection (TIR) angle is nearly met so that an inclined sheet of light is illuminating the sample with a depth of around 10 μm (as discussed in 2.3.3). Chip-based TIRF illumination benefits form the high index contrast materials giving very good optical sectioning (2.16), thus ideal for maintaining adequate SNR.

dSTORM is an intensity consuming technique, requiring up towards 1-10 kW/cm^2 for blinking of the most popular fluorophores such as Alexa Fluor 647, with some implementations reporting up to 50 kW/cm^2 being used [20]. In a conventional setup, the benefit of HiLO over TIRF is the increased intensity it provides (not relying on evanescent field excitation). To achieve high excitation intensities using waveguides, HIC materials are beneficial.

Furthermore, the excitation light distribution for SMLM should ideally have a flat intensity profile. The dark-state formation in dSTORM is an intensity requiring process, which means that fluorophores under high-intensity illumination have a greater chance of entering a long-lived dark state. If the excitation light profile used for dSTORM is uneven, the on/off rate is also affected, where regions receiving high intensity may have more molecules in the dark state and vice-versa. For TIRF methods, the evanescent field intensity can be low, and artifacts due to uneven intensity profiles might occur. In a conventional objective-based TIRF microscope the excitation profile is Gaussian and the FOV used for SMLM imaging is typically limited to only the center region of the Gaussian profile, due to the reasons above. Furthermore, some commercial super-resolution microscopes such as the OMX blaze from GE healthcare (available at our lab) have a beam concentrator, directing more intensity towards the central region of the FOV further reducing the usable FOV size. A method by the Manley group made efforts into expanding the excitation light profile provided by the high N.A. objective lens, using a system of micros-lenses and diffusers [62]. Additionally, methods using multimode fiber with a diffuser to scramble

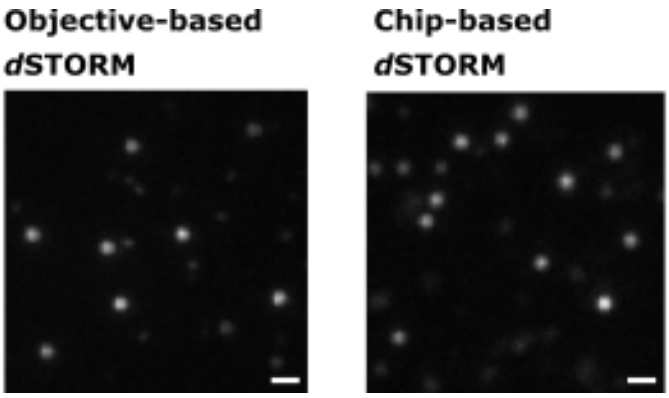

Figure 4.1: Objective-based dSTORM and chip-based **d**STORM achieves similar results for the blinking of Alexa-Fluor 647 dye molecules.

the modes [63] have been implemented. Both of these methods successfully increased the illuminated area for dSTORM, but still have a limited FOV due to the collection optics high N.A.

On the other hand, by using waveguides to steer the light towards the sample, the excitation pattern is not Gaussian but rather determined by the waveguide material and geometry. By using wide waveguides of HIC materials the illumination can be available over large regions but at the cost of highly disruptive MMI patterns. As discussed and the last chapter, the presence of higher-order MMI pattern can be reduced using tapering or multimode scrambling. For large width, the latter is the most efficient to implement due to the very long tapering lengths needed to expand singlemode waveguides adiabatically to several hundred micrometers, as was shown in [61].

4.2 Results and discussion

To achieve the required evanescent field intensity, high refractive index materials Ta_2O_5 and Si_3N_4 were used. Strip waveguides with a core height between 150-220 nm were used. Strip waveguides were used having widths up to 600 μm. The strip waveguides offer higher-order modes than rib waveguides, which is more effective for removing stripe artifacts caused by MMI.

The evanescent field intensity was measured indirectly by using a layer of fluorescent beads. The fluorescence response of the beads was detected on the camera, and compared with objective-based illumination with a known intensity. These measurements gave a field intensity adequately strong for dSTORM, reaching up to 12 kW/cm^2 in some cases. See supplementary table

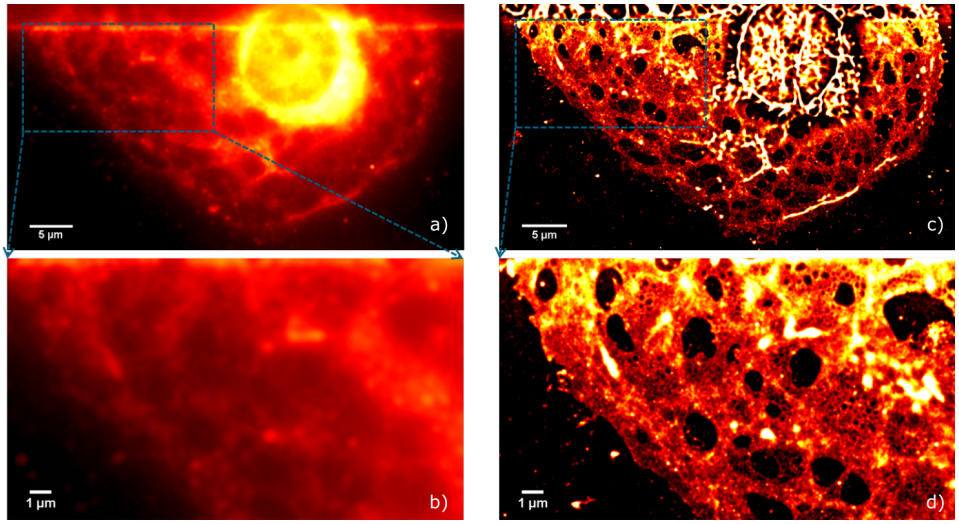

Figure 4.2: a,b) Chip based diffraction-limited image of LSEC stained for the plasma membrane. c) Using dSTORM, membrane fenestration becomes visible, as better seen in the zoomed image (d).

from paper 3.

The coupling mechanism for coupling on to the waveguides was explored using both objective and fiber-based coupling. Using fibers is possible for both diffraction-limited imaging and dSTORM, however, we only experienced efficient blinking for dSTORM at fairly low waveguide widths (25 um, figure 2(a) in paper 3) using a lensed fiber. Additionally, the fiber-based coupling would suffer from burning fibers due to high power (300 mW-500 mW) laser being coupled in free space on to the fibers. For most of the imaging, we thus used an objective lens with N.A.=0.5 to couple the light from free-space on to the waveguides.

To confirm that single-molecule switching and imaging is possible using the chip-based setup, a comparison between chip-based and objective-based TIRF illumination for dSTORM was carried out. A fluorescent dye-surface was prepared using Alexa-647 molecules in Poly-L-Lysine (PLL). The surface was brought into a blinking state using the common MEA buffer reported in [20]. Figure 4.1 shows two frames from the acquired image stacks, where both methods show separated emitters. This measurement was also performed using a lower N.A. objective lens, which can be seen in the supplementary information of paper 3.

A similar experiment was performed to show that single-molecule switching could be achieved over large waveguide widths. Each waveguide was imaged

using different power settings to settle the minimum power needed for the blinking of fluorophores on a fluorescent dye layer. This result is presented in paper 4, figure 2. Blinking of fluorophores was confirmed for all the tested waveguides having widths up to 1 mm.

Chip-based dSTORM imaging was demonstrated by imaging samples of LSECs directly mounted on the waveguide surface. Figures 4.2(a,b) show the diffraction-limited image of a cell labeled with Cellmask deep red plasma membrane stain. The dye was excited using a 660 nm laser. Figures 4.2(c,d) show the same cell in dSTORM mode with 50 nm resolution. The comparison with (a,b) clearly shows the resolution enhancement, wherein the dSTORM image, liver fenestration become visible as a network of holes. The liver fenestrations have dimensions around 100-150 nm [64]. A resolution of 50 nm was quantified using both Fourier ring correlation and data statistics in addition to direct measure in the images, as seen in figure 2 in paper 3.

The illumination profiles of the waveguide were compared with the illumination profile of a commercial system. The surface of the waveguide was stained with a fluorescent dye and imaged with diffraction-limited resolution, with MMI scrambling engaged. The same sample was prepared and imaged in the OMX blaze system using ring TIRF [65] and with the beam concentrator activated. The result is shown in Fig. 4.3, where Figs. 4.3(a-c) show the illumination profile of the waveguide with line-profiles at the indicated region. The residual mode-pattern has 16 % modulation over the width of the waveguide (ignoring the edge artifacts) (Fig. 4.3(b)). The GE healthcare OMX blaze system illumination profile is shown in Fig. 4.3(d-f), where the Gaussian nature of objective-based illumination is obvious with some added strength to the center of the distribution due to the beam concentrator.

For a maximum of 16 % intensity modulation (as for the waveguide), the OMX blaze system would be limited to a field of view of 18 x 18 μm^2, due to the Gaussian envelope as seen in Fig. 4.3(d-f). As discussed in [62], illumination variations are not a big problem for dSTORM as long as the required illumination intensities are met. However, when illumination intensities drop below 1-10 kW/cm^2 the number of multiple emitters, i.e overlapping blinking events, may increase and the reconstruction will show clustering artifacts [66]. The residual ripples in the waveguide-based illumination were measured for waveguides having widths up to 1mm (figure 3 in paper 4), and found to increase up towards 25 % for wide waveguides.

The use of MMI scrambling for real biology samples was investigated using a sample of LSECs stained with Cellmask deep red, targeting the plasma membrane. Two time-points of the diffraction-limited stack (Fig. 4.4(a,b) shows the presence of dark areas shifting in time, due to the mode scanning

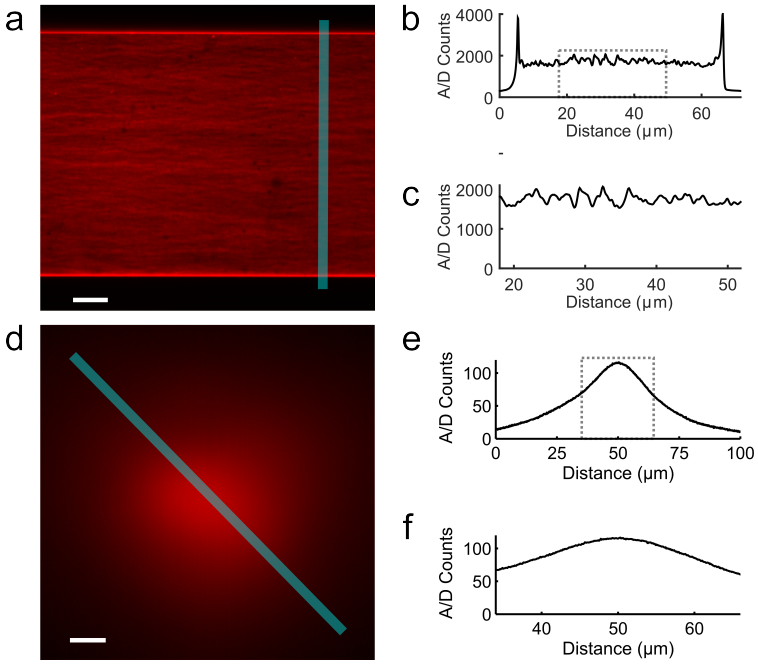

Figure 4.3: (a) The illumination profile of the waveguide is visualized using a fluorescent dye layer. (b,c) The residual intensity modulation due to MMI is around 16% over the width of the waveguide as shown from the line profile indicated with a blue line in (a). (d) In a commercial microscope like the OMX blaze V4, the illumination is Gaussian where if we restrict the field of view allowing 16 % modulation yields a field of view of 18 x 18 μm^2, which is shown in the line profile (e) and the zoomed line profile (f).

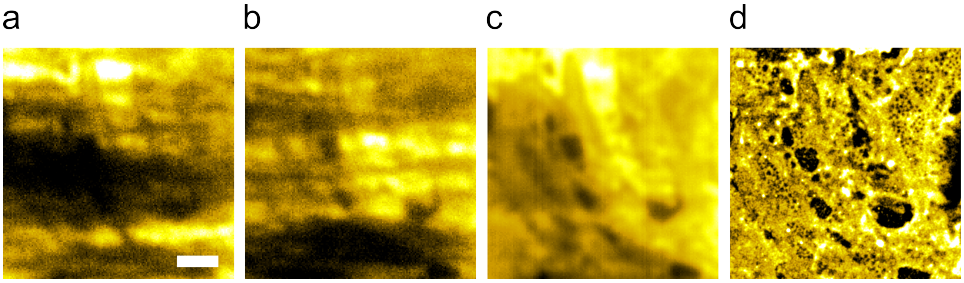

Figure 4.4: Effect of MMI scrambling. (a,b) show two frames from a stack of diffraction-limited images while the coupling objective lens is scanning the input facet of the waveguide. Dark areas are seen shifting over the images. (c) Averaging 200 frames yields a near-uniform excitation pattern. d) A dSTORM image reconstruction of the same area is free from MMI patters, and super-resolved details are visible, here liver fenestrations are observed as tiny holes in the membrane of the cell.

(Fig. 3.9). The average of 200 frames can be seen in Fig. 4.4(c) almost with no MMI pattern. The effect of scrambling the modes under the dSTORM acquisition, consisting of several thousands of frames is seen if Fig. 4.4(d), where the reconstructed dSTORM image is free from MMI artifacts.

4.2.1 Large field-of-view chip-based dSTORM

The possibility of having TIRF illumination over extraordinary large fields of view is one of the main arguments in favor of chip-based microscopy. We investigated the possibility of generating large FOV super-resolved images using wide waveguides to acquire FOV dimensions on the millimeter scale. To utilize the large area illumination it was necessary to use objectives with a low magnification (and lower N.A.) than the high N.A objectives commonly used for collection. The change in N.A yields less efficient detection of single-molecules, and thus a decrease in resolution for SMLM.

In a conventional objective-based system, SMLM imaging is done with high N.A objectives. This is due to the locking of excitation and collection light paths as seen in Fig. 2.8. Using low N.A. EPI-illumination is possible but would render images of high background noise. While a high N.A. objective lens has good optical sectioning capabilities, a low N.A. objective will not show this characteristic. The axial resolution of the objective lens scales with $n/N.A.^2$, which for a typical 20x (having N.A.=0.4) objective means that the focal volume (the depth of field) of the objective lens spans around 4 μm axially. This further means that everything within those 4 μm will be interpreted as coming from the same plane. For dSTORM, if one uses an N.A.=0.4 objective lens for illumination, then it will lead to background fluorescence from the

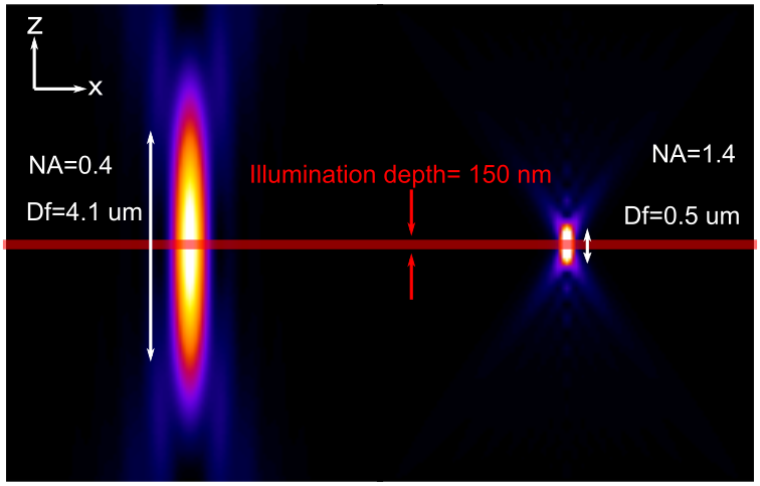

Figure 4.5: The depth of field of a low N.A. objective, and a high N.A. objective visualized by the axial point spread function. The N.A. =0.4 lens show an axial resolution of 4 μm, while the N.A. =1.4 oil immersion lens has an axial resolution of around 500 nm. The evanescent field penetration depth generated by waveguide remains unchanged when changing imaging objective lens.

entire focal volume. Contrary to this, chip-based TIRF illumination is a perfect match for utilizing a low N.A. objective lens for dSTORM since it comes with intrinsic optical sectioning, not limited by the N.A. of the objective lens. Figure 4.5 visualize how the depth of field changes with the imaging objective lens, while the penetration depth of the evanescent field generated by the waveguide remains constant as it is independent of the objective lens.

The results of using different objectives in a dSTORM measurement are shown in Fig. 4.6 for a sample of LSECs stained for the tubulin network with Alexa 647. Figure 4.6(a) shows the high N.A. case, achieving a resolution around 47 nm. The diffraction-limited image is included in the corner. Figures 4.6(b,c) show that it is possible to acquire SMLM images using low N.A objective lenses, e.g N.A.=0.8 and N.A.=0.45. The FOV dimension and the achievable resolution are affected by switching to these lenses. The best compromise we found was using a lens with 25x/0.8NA. This gave a large FOV with a resolution of 75 nm (Fig. 4.6(b)), while the N.A.=0.45 objective gave around 140 nm resolution on a comparable FOV (Fig. 4.6(c)).

Large FOV dSTORM imaging was demonstrated over a field of view of 500 x 500 μm^2. A sample of LSECs was mounted directly on the chip surface following standard protocols. The cells were stained with Alexa 647 for tubulin. A microscope objective lens from Zeiss having N.A.=0.8 and 25x magnification was used. Using this configuration the measured resolution from the dSTORM reconstruction was around 75 nm, which was confirmed by the localization

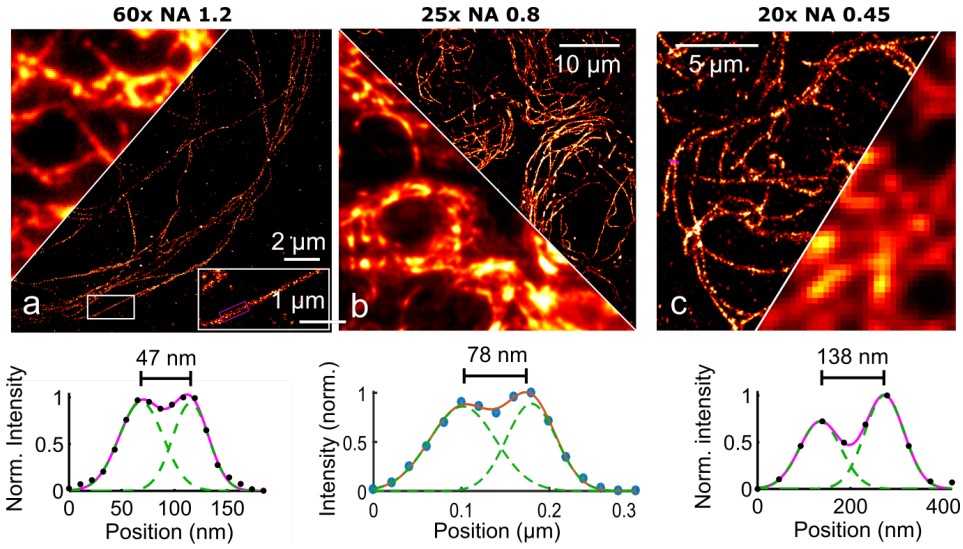

Figure 4.6: Comparison between different objectives for chip-based SMLM imaging. (a) Using N.A =1.2 yields a resolution in the dSTORM reconstruction of around 47 nm, (b) N.A=0.8 gives around 75 nm resolution, while N.A 0.45 gives around 140 nm resolution (c). The sample is LSECs labeled with Alexa 647 for the microtubules.

precision data and Fourier ring correlation (FRC) [67]. The reconstruction is shown in Fig. 4.7(a). Here, some hundred cells are imaged simultaneously at sub-100 nm resolution, not possible in other nanoscopy imaging techniques. Fig. 4.7(b) show the zoom indicated with a magenta box in Fig. 4.7(a), with a comparison with the diffraction-limited image showcasing the resolution enhancement. Figure 4.7(c) shows a closer zoom (marked with a green box in Fig. 4.7(a)), with a blue line indicating the position for the line-profile plotted in Fig. 4.7(d). The line-profile (Fig. 4.7(d)) measures 78 nm separation distance between two tubulin filaments. Fig. 4.7(e) shows the localization precision data indicating a lower bound for the resolution of around 70 nm, while FRC (Fig. 4.7(f)) yields around 72 nm.

4.2.2 Fluctuation nanoscopy using multimode interference fluctuations

MMI patterns were initially thought to be a drawback of the chip-based illumination that needed to be fixed. Since strip waveguides were used, the MMI patterns were highly chaotic with randomly looking speckles, most varying in the transverse direction of wave propagation, as seen in Fig. 3.8(a). The fluorescence response was equally speckled. Speckle illumination has been shown for SOFI imaging [37] where the speckles were generated with a multimode fiber, and the pattern was projected on the sample via an objective.

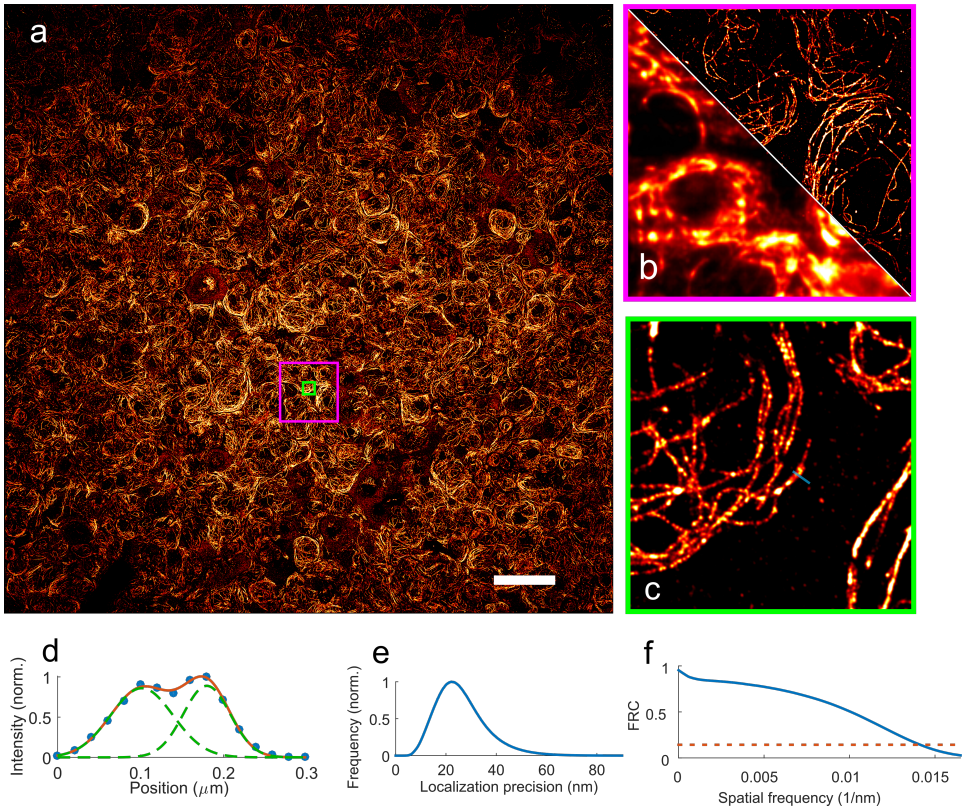

Figure 4.7: (a) Chip-based dSTORM is demonstrated over an extraordinary large field of view. Here, several hundred cells are imaged simultaneously at a resolution of 75 nm. (b) The diffraction-limited image is compared against the dSTORM reconstruction from the magenta box indicated in (a). (c) The zoom is marked with a green box in (a), with the position of the line plot in (d) marked with a blue line. (d) The line-plot shows two filaments separating with a distance of 78 nm, which can still be resolved in the dSTORM image. (e) The dSTORM reconstruction software provides the localization precision for all included localizations shown in (a), having a peak at around 21 nm. (f) Fourier ring correlation suggests a lower bound for the resolution in the image to be 72 nm.

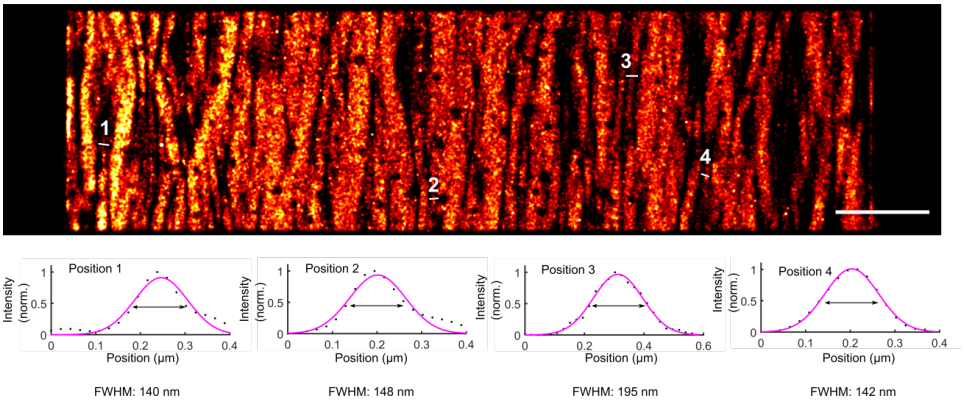

Figure 4.8: The MMI pattern was imaged using dSTORM to visualize the sub-diffraction-limit constituents of the intensity distribution. full width at half maximum (FWHM) reaching down to 142 nm was measured in the resulting reconstruction as seen from the different line-plots marked with numbers in the image.

Using speckle illumination, the expected resolution enhancement is dictated by the MMI pattern spatial frequencies. Using HIC materials, here Ta_2O_5, the expected fringe spacing is determined by n_f and the angle of the interfering light. Here, we used straight waveguides, so the fringe spacing would be larger than for counter-propagating light (which is exploited in chapter 5), however, due to a high n_f, the speckle pattern has diffraction-limited components. To confirm the presence of sub-diffraction-limited speckle patterns, the MMI pattern was imaged using dSTORM. The surface of the waveguide was stained and the dSTORM measurement was performed while keeping the pattern stationary. The result is seen in Fig. 4.8. Measuring FWHM in the MMI pattern show excitation light with a sub-diffraction-limited size down towards 140 nm.

The data for chip-based fluctuation nanoscopy consists of a series of images using temporal MMI fluctuations as the excitation light. For each image, the object (e.g. a cell) is constant, but the excitation light pattern changes as shown in Fig. 4.9. For fluctuating intensity data, several reconstruction algorithms could potentially be used (e.g SOFI, ESI or MUSICAL). Our choice on ESI was merely based on the availability of a Fiji plugin, without the need to acquire a mathematical understanding of the method. This method was originally not a part of the project but was performed when we understood the possibility.

To compare the different methods, ESI analysis was used on the same stack of images used to acquire a diffraction-limited image. Furthermore, by increasing the excitation light intensity and using dSTORM imaging buffer, in the same experiment, the dSTORM image was acquired. This allowed for a one-to-one comparison of chip-based diffraction-limited imaging with ESI and dSTORM.

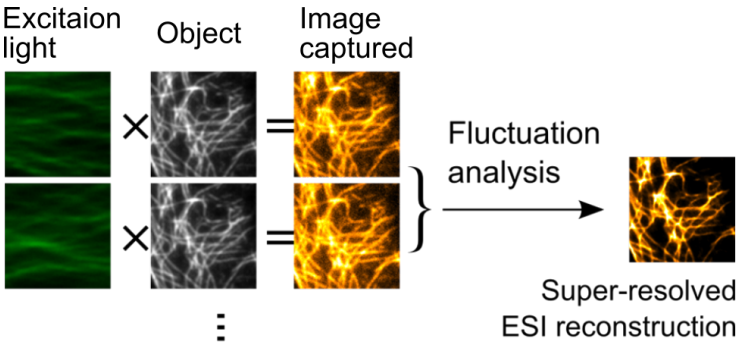

Figure 4.9: In chip-based ESI, a series of images are acquired where for each image the excitation light is a MMI pattern. The MMI pattern is shifted between each image, while the sample remains the same. The fluctuation analysis is performed in Fiji, which yields the super-resolved ESI image.

This can be seen in Fig. 4.10 where the three different images are presented together. A line-profile compares the achieved resolution, with structures down towards 100 nm are resolved using ESI, and confirmed with dSTORM. For a more thorough justification of the achieved resolution using chip-based ESI, see supplementary figure 10 and supplementary note 1 in paper 3.

4.2.3 Summary of papers

The outcome of the work covering chip-based dSTORM was two papers.

Paper 3 covers the first realization of dSTORM on-chip, where the main work went into showing the proof of principle. The main results demonstrate dSTORM imaging over an extraordinary large field of view, with the possibility of having multiple colors. Here, a FOV of around 0.5 x 0.5 mm^2 was acquired with a resolution of around 140 nm. This is around 100 times larger FOV than that of conventional objective-based systems. Furthermore, multicolor dSTORM imaging was shown, showcasing the easiness of wavelength multiplexing using waveguides. In an objective-based system, the TIRF angle (critical angle) must be changed when switching wavelengths, not necessary using our system. Also, multi-modality imaging, combining diffraction-limited, ESI and dSTORM was shown. ESI imaging is a compromise between temporal resolution and spatial resolution in optical nanoscopy. One ESI image was acquired over around 5 seconds, using 500 frames of data, with a spatial resolution approaching 100 nm.

Paper 4 further improves the resolution enhancement possible for a large FOV chip-based dSTORM. To overcome techniques such as SIM, which can

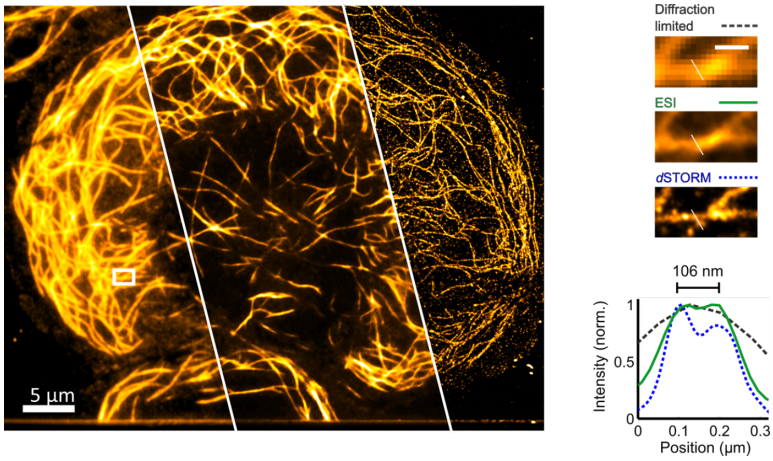

Figure 4.10: Multi-modality chip-based nanoscopy is shown. The diffraction-limited image is shown from the left. Using a few hundreds of frames with MMI fluctuation data, the ESI reconstruction was possible as seen in the middle image. During the same experiment the sample was brought into a blinking state by increasing the laser power and a dSTORM image could be achieved (right panel). This gives a one-to-one comparison of the resolution enhancement possible using ESI, where 106 nm resolution was measured in the images, confirmed with the dSTORM image (which has 50 nm resolution).

image large FOV by stitching at a high temporal resolution, the resolution should be pushed below 100 nm for our method. In this paper we show 75 nm resolution over 0.5 x 0.5 mm^2 area, using an objective lens having 25x magnification with N.A of 0.8. We further measured some key parameters for successful dSTORM imaging in wide waveguides, such as switching efficiency for wide waveguides and modulation depth of residual mode-patterns for different waveguide widths.

4.2.4 Outlook

With these publications, we have established the first proof-of-concept for super-resolution imaging on a chip. A natural next step would be to improve the technique to work more stably. Overall, the evanescent field intensity that was achieved during this work, is on the low side of what could be expected to work for dSTORM. Referencing to the supplementary table in paper 3, dSTORM imaging of Alexa-647 was achieved for intensities as low as 0.1 kW/cm^2. To further optimize the technique it would be beneficial to have at least around 10 times the power available.

4.3 Paper 3: Chip-based wide field-of-view nanoscopy

Published in Nature Photonics, 2017.

Authors: Øystein I. Helle*, Robin Diekmann*, Cristina I. Øie, Peter McCourt, Thomas R. Huser, Mark Schüttpelz and Balpreet S. Ahluwalia.

*Shared first-authorship/Authors of equal contribution

Author contributions: B.S.A. and M.S. conceived the project. All authors designed the research. C.I.Ø. isolated the cells and stained and prepared the biological samples. R.D. and Ø.I.H. built the set-up, prepared the non-biological samples, performed the experiments, performed the simulations, reconstructed the images, analyzed the data and created the figures. R.D., Ø.I.H., M.S. and B.S.A. mainly wrote the paper. All authors reviewed the manuscript.

4.4 Paper 4: Nanoscopy on-a-chip: super-resolution imaging on the millimeter scale

Published in Optics Express, 2019.

Authors: Øystein I. Helle, David C. Coucheron,Jean-Claude Tinguely, Cristina I. Øie and Balpreet S. Ahluwalia.

Author contributions: Ø.I.H. built the setup, did the experiments, did the data analysis and wrote the paper. D.A.C. assisted some of the experiments and analysis. C.I.Ø. prepared the biological samples J.C.T. made the chip mask. B.S.A. supervised the project. All authors reviewed the paper.

Research Article | Vol. 27, No. 5 | 4 Mar 2019 | OPTICS EXPRESS 6700
Optics EXPRESS

Nanoscopy on-a-chip: super-resolution imaging on the millimeter scale

ØYSTEIN I. HELLE, DAVID A. COUCHERON, JEAN-CLAUDE TINGUELY, CRISTINA I. ØIE, AND BALPREET S. AHLUWALIA*

UiT-The Arctic University of Norway, Klokkargårdsbakken 35, 9037 Tromsø, Norway
*balpreet.singh.ahluwalia@uit.no

Abstract: Optical nanoscopy techniques can image intracellular structures with high specificity at sub-diffraction limited resolution, bridging the resolution gap between optical microscopy and electron microscopy. So far conventional nanoscopy lacks the ability to generate high throughput data, as the imaged region is small. Photonic chip-based nanoscopy has demonstrated the potential for imaging large areas, but at a lateral resolution of 130 nm. However, all the existing super-resolution methods provide a resolution of 100 nm or better. In this work, chip-based nanoscopy is demonstrated with a resolution of 75 nm over an extraordinarily large area of 0.5 mm x 0.5 mm, using a low magnification and high N.A. objective lens. Furthermore, the performance of chip-based nanoscopy is benchmarked by studying the localization precision and illumination homogeneity for different waveguide widths. The advent of large field-of-view chip-based nanoscopy opens up new routes in diagnostics where high throughput is needed for the detection of non-diffuse disease, or rare events such as the early detection of cancer.

1. Introduction

For a long time, the spatial resolution in optical microscopy was believed to be bound by the diffraction limit. The famous resolution equation [1], shows that the resolving power of the microscope is a simple function of numerical aperture (N.A.) and the wavelength of light, effectively limiting the lateral resolution to around 200-300 nm for visible wavelengths. However, from the early 90s up until now a range of techniques developed that aim to produce images with spatial resolution way beyond that of the diffraction limit. This field is commonly known as super-resolution optical microscopy or optical nanoscopy, and has given biologists tools to observe living intracellular structures with unprecedented high resolution. Lately, improvements in the nanoscopy methods have pushed the spatial resolution towards the ultimate limit i.e. the physical size of the fluorescent labels [2]. For conventional immunolabeling at room temperature using antibody-binding of fluorophores, this typically means a few tens of nanometers.

While nanoscopy has pushed the optical resolution, the improvement does not come for free. One of the major payoffs is the reduced size of the field of view (FOV) with images typically being on the size of 10 μm x 10 μm to 50 μm x 50 μm. This severely limits the throughput of the current super-resolution techniques since only parts of a cell, or up to 1-2 cells can be imaged simultaneously. Most of the nanoscopy methods aim to separate the fluorescence molecules in time by manipulating the photo-physics of the fluorescent dye molecules, achieving a spatial resolution down to around 10-30 nm. These techniques include scanning methods such as stimulated emission depletion (STED) [3], and single-molecule localization microscopy (SMLM) methods such as (direct) stochastic optical reconstruction microscopy (d)STORM) [4, 5] and (fluorescence) photoactivated localization microscopy ((f)PALM) [6,7]. Methods like stochastical optical fluctuation intensity microscopy (SOFI) [8], entropy-based super resolution imaging (ESI) [9] and multiple signal classification algorithm (MUSICAL) [10] lessen the demand on the control of the photophysics of single-molecules by working with signals from multiple fluorophores and using clever reconstruction algorithms to achieve an improved resolution. One

#345909 https://doi.org/10.1364/OE.27.006700
Journal © 2019 Received 25 Sep 2018; revised 9 Dec 2018; accepted 29 Dec 2018; published 22 Feb 2019

Optics EXPRESS

of the most used methods for live cell imaging is structured illumination microscopy (SIM) [11], which use light pattern illumination to encode high frequency content (unresolved) in low frequency signals, yielding around 100 nm lateral resolution. SIM has gained popularity by its live cell compatibility, minimal photo-toxicity, ease of use, and compatibility with most bright fluorophores.

The next breakthrough in optical nanoscopy would represent high throughput imaging. This refers to techniques that can extend the amount of data acquired, by imaging at super-resolution over large areas/volumes fast. The limited throughput of present day nanoscopy methods hinders the collection of sufficient information for drawing statistically relevant conclusions from biological systems. When looking at extending the field of view of optical nanoscopy the easiest would be to employ SIM and create a stitched image consisting of many SIM images side by side. SIM is inherently fast, since it only use 9 /15 images to create one super resolved SIM image in 2D/3D, and a stitched image can be created in a reasonable amount of time, but with spatial resolution limited to around 100 nm. To get the resolution below 100 nm it is thus necessary to increase the FOV of one of the other nanoscopy techniques. The intrinsic scanning nature of STED makes these techniques slow for large areas (such as 500 μm x 500 μm). On the other hand, SMLM being a wide field method, the entire FOV can be acquired simultaneously which is desirable when moving to large area imaging. SMLM methods are typically not very fast (tens of minutes), since thousands of images needs to be acquired to generate a super-resolved image. However, using advanced reconstruction algorithms including compressive sensing [12], SMLM with high-temporal resolution (i.e. in seconds), has been demonstrated.

To increase the FOV for SMLM images it is desirable to use a low magnification objective lens to cover large areas without scanning. For a given optical set-up, the imaged area acquired for a 20X objective lens will be approximately 10X larger than that of a 60X objective lens. In a conventional SMLM setup, excitation light is sent through a high numerical aperture (N.A.) objective lens, and the emitted fluorescence is detected with the same objective. Using a low magnification and low N.A. objective lens in SMLM will create two problems. Firstly, a low magnification/N.A. objective will have a large depth of field, which scales inversely to N.A. squared. This results in the collection of light signals from rather large volumes, giving increased background signal. This will eventually reduce the localization precision and the optical resolution for SMLM, which relies on 2D Gaussian fits over individual blinking events. Presently this problem is solved by using a high magnification/N.A. total internal reflection fluorescence (TIRF) objective lens. A TIRF lens creates an evanescent field illuminating only a thin section of the sample, typically up to 100-150 nm from the surface and thus generating illumination capable of achieving an excellent signal to noise ratio. However, a low magnification/N.A. TIRF objective lens is not commonly available.

Secondly, the illumination for SMLM needs to be uniform. SMLM relies on sparse blinking of the fluorophores, which for the case of *d*STORM is achieved by photo-switching in the presence of a reducing buffer. An uneven illumination will thus provide un-even switching rates generating poor images. The objective lens generates excitation light with a Gaussian profile, where only the most central part of the FOV is useful for SMLM imaging. A few approaches have improved upon this problem [13, 14], but both methods are still collecting with the same high N.A. objective lens, effectively limiting the FOV.

To alleviate the above mentioned problems, it is evident that the separation of the illumination and collection light paths for SMLM will be beneficial. Recently [15], it was shown that by using a photonic chip to illuminate the specimen one could use low magnification objectives to acquire *d*STORM images over an area of 500 μm x 500 μm, 100X larger area than the conventional approach, with lateral resolution of 130 nm.

However, in the previous work the resolution demonstrated by chip-based *d*STORM was limited to around 130 nm and thus could not surpass the diffraction barrier of 100 nm. With a

Optics EXPRESS

resolution of 130 nm chip-based *d*STORM lacked the impact over SIM which can acquire slightly better resolution (100-120 nm) over the same area by scanning and stitching in less time than chip based *d*STORM. In this paper we show that chip-based *d*STORM can be used to acquire images with an optical resolution of 70-75 nm over an extra-ordinary large FOV (500 μm x 500 μm), and thus breaking the diffraction barrier of 100 nm for high throughput optical nanoscopy. Here, we have also investigated crucial parameters to benchmark the performance of chip-based nanoscopy such as localization precision as a function of waveguide width and input power; and the uniformity of the illumination generated by the chip as a function of waveguide width.

2. Principle of chip-based fluorescence imaging

In conventional microscopy/nanoscopy the sample is prepared on a glass-slide/coverslip. Chip-based microscopy replace this arrangement with a photonic integrated circuit (PIC) and the sample is prepared directly on the PICs top surface, as depicted in Fig. 1(a). The PIC chip is made on a Silicon substrate with a buffer layer of Silicon Dioxide (SiO_2) followed by a thin top layer of Silicon Nitride (Si_3N_4). By shaping the geometry, i.e creating side-walls, the layer functions as as an efficient waveguide for propagating excitation light to the specimen. Laser-light is coupled into the waveguide by focusing a beam of light on to the end-facet using an objective lens. The light propagates inside the waveguide by total internal reflection, however a small part the field leaks out in the form of an evanescent wave. The specimen is fluorescently labeled and the fluorophores are excited via the evanescent field stretching around 150 nm in to the sample as shown i Fig. 1(b). This means that only the part of the specimen located within these 150 nm will be illuminated. The evanescent field penetration depth is fully determined by the wavelength, and the local refractive index at the waveguide-sample boundary. The sample can be mounted following the same protocols as for the glass-slide/coverslip arrangement, and the PIC has also shown to be bio-compatible supporting live cells experiments [16].

For efficient photo-switching of the fluorophores, the evanescent field intensity directly at the surface must be strong (ideally 1-10 kW/cm^2), which is achieved by the use of a high refractive index material, in this work Si_3N_4 having n$\approx$ 2.0, for 660 nm excitation laser light. The high-refractive index material together with a shallow cross-section (waveguide thickness of 150 nm) confines the light tightly inside the waveguide, but with up to 5-10% of the guided power available in the evanescent field. The high refractive index contrast also ensure that the penetration depth of the evanescent field is shallow, yielding good optical sectioning.

Using a high-refractive index waveguide such as Si_3N_4 at visible wavelengths, higher order modes are supported by the strip waveguide geometry starting from waveguide widths of 1.5 μm. These modes travel in discrete paths generating non-uniform illumination patterns. As the dimensions increase above a few micrometers, more modes starts to interfere with each other, creating a highly chaotic illumination pattern, referred to as multi-mode interference (MMI) patterns. The resulting evanescent field illumination is thus also contaminated with non-uniform MMI patterns, resulting in images of poor quality, disturbed by stripe patterns. The MMI patterns can be scrambled, and thus create a uniform image by shifting the mode patterns in time, and then take the average of several sub-sets of MMI patterns. There are two possibilities to achieve this, either rapid scanning the input beam using a galvo mirror, or slow scanning the input beam by moving the coupling objective lens using a motorized/piezo stage. The galvo mirror can scan quicker than the camera exposure time so every frame captured will show uniformity. The other approach scans slowly, using the average of a few hundred frames to create a uniform image. In the case of *d*STORM several thousand frames are captured by default so any of the two methods can be used. In this paper we chose to slow-scan the input beam by moving the coupling objective with a piezo stage as discussed in [15].

Unlike the TIRF objective lens, the generation of the evanescent field by an optical waveguide is decoupled from the imaging objective lens. As a consequence, the evanescent field is available

Optics EXPRESS

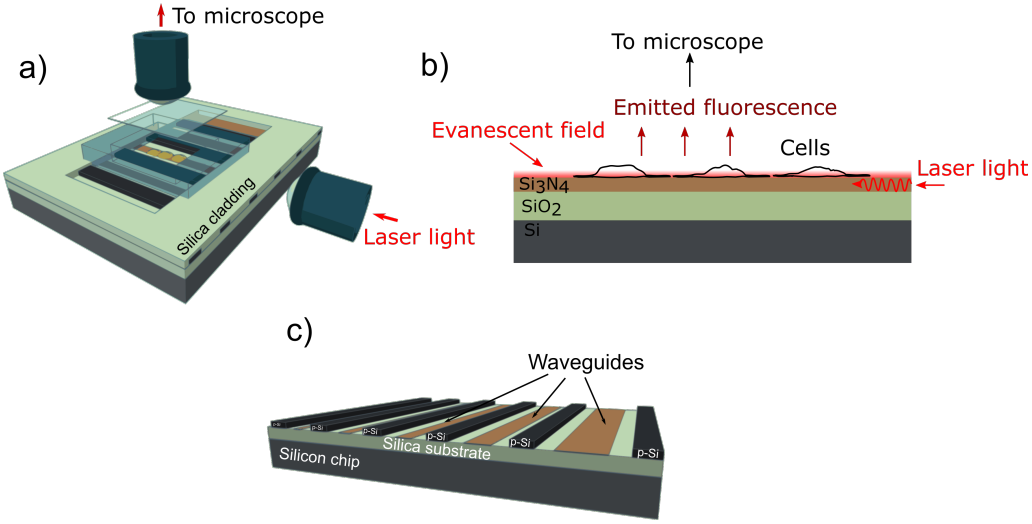

Fig. 1. a) Laser light is coupled into a PIC via an objective lens, and light is guided towards the specimen in optical waveguides. On top of the chip there is a PDMS microchamber to contain the image buffer. b) In the center of the chip there is an opening in the protective cladding where the specimen is mounted to come in contact with the evanescent field. The fluorescent signal is captured by an upright microscope. c) The PIC has lateral dimension of around 3 cm x 3 cm. A layer of SiO_2 give a strong refractive index contrast against the Si_3N_4 waveguide. In between the guiding material are layers of Poly-Silicon that blocks light from passing in to neighboring waveguides.

over large areas, only limited by the waveguide dimension. Furthermore, it allows a free choice of the objective lens used to collect the emitted fluorescence. In this way, a low N.A. objective lens can be used to acquire a large FOV without sacrificing the excellent optical sectioning provided by the chip-based illumination.

3. Materials and methods

3.1. Waveguide fabrication

The waveguides were made by first sputtering a 2 μm thick layer of SiO_2 onto a silicon wafer. The 150 nm thick guiding layer of Si_3N_4 was then added by low-pressure chemical vapor deposition at 800°C, before the waveguide structure was outlined by photo-lithography. The strip waveguide structures were then realized by ion etching all the way down to the silica cladding. Another layer of poly-silicon was realized to function as a light absorbing layer in between neighboring waveguides to stop unguided light from leaking to other waveguides. This can be seen as the black layer in Fig. 1(c). A 1.5 μm thick layer of SiO_2 was used to create a protective top cladding, and reactive ion etching was used to open up the cladding at the imaging area, where cells can be seeded directly on top of the waveguide core accessing the evanescent field. For fluorescence imaging of biological samples, the dimensions typically must be larger than the cells under investigation. Here, waveguide widths between 50 μm and 1 mm were used. A PDMS micro-chamber was used to contain the aqueous image buffer during the measurements. The thickness of the chamber was approximately 130 μm, well below the working distance of the objective lens used for the collection.

Optics EXPRESS

3.2. Experimental setup

The setup was based around an Olympus modular upright microscope fitted with a water cooled sCMOS camera (Hamamatsu ORCA flash). Images were acquired using two different objective lens (Olympus UplanSApo x60/1.2 w and Zeiss LD LCI Plan-Apochromat x25/0.8). The Zeiss multi-immersion objective lens was used to gather the large FOV images. The Zeiss objective lens was used with the olympus tube lens, such that the effective magnification of the setup changed, leaving around 27 x effective magnification. The chip was secured by a vacuum air-lock to further minimize sample drift. Laser was coupled into the chip using a x50/0.8 objective lens. The laser used for *d*STORM is a Cobolt Flamenco 660 nm with up to 500 mW output power. The microscope was mounted on motorized stages enabling lateral movement for observation of different regions on the chip. The data was acquired using a computer and the localization data was analyzed using Fiji open source image processing software and the localization data analysis plugin ThunderStorm [17]. The camera exposure time was set to 25 ms for all *d*STORM experiments.

3.3. Sample preparation

A fluorescently labeled surface was created by incubating a solution of 50nM Alexa647 molecules in 0.05% Poly-L-Lysine for 10 minutes at room temperature (RT). The solution was aspirated and the surface rinsed gently three times with dH20. *d*STORM buffer was prepared following [18]. The buffer contains an enzymatic scavenger system containing Catalase (Sigma #C100) and Glucose Oxidase(Sigma #G2133) together with 100 mM Mercaptoethylamine (MEA, Sigma #M6500). The addition of 2mM Cyclotetraene (COT, Sigma #138924) has shown to help with blinking performance of Alexa647 on waveguides. Cells were harvested from male Sprawgly rat, with body weights between 150-300 g. Liver sinusoidal endothelial scavenger cells were isolated using the method from [19], and kept alive in RPMI 1640. To help with attaching the cells to the waveguides chips, the surface was coated with fibronectin (50 μg/ml) for 10 minutes at RT. The cell suspension was incubated on the surface of the chips for 1 hour at 37°C and 5% O_2. The surface was rinsed with fresh RPMI 1640, to remove debris and the chips were incubated for 2 more hours to allow spreading of the cytoplasm. Fixation of the cells were performed using 4% Paraformaldehyde for 30 min. The tubulin was stained using primary antibody β-tubulin(Sigma Aldrich) at 1:400 in PBS for 1h at RT. The secondary antibody was goat anti-mouse Alexa Fluor 647 at 1:400 in PBS, incubated for 1H at RT. The cells were washed three times with PBS before the image buffer was applied and the chambers sealed with a coverglass.

4. Results

For high throughput chip-based nanoscopy, wide waveguides are essential to illuminate large areas. The dimensions of the waveguides must be made such that the evanescent field intensity is sufficiently strong, enabling photo-switching of fluorophores on top of the waveguide surface. In order to establish the appropriate waveguide dimensions for large FOV imaging we investigate the impact of waveguide width and input power for a *d*STORM on-chip measurement. This was achieved by measuring localizations coming from a single-molecule layer deposited on top of the waveguide surface, as a function of waveguide widths and at different input powers. A *d*STORM experiment was carried out on the surface over a fixed area, and repeated for different waveguide widths. Waveguides of different widths were located next to each other on the same chip as indicated in Fig. 1(a). In Fig. 2 the number of localizations acquired using 1000 frames of data is plotted against the input power for 4 different waveguide widths. The number of localizations detected for each waveguide width follow the same trend for waveguide widths up to 400 μm, while for the 600 μm wide waveguide the curve takes on another shape. This shows that waveguides of widths 200-400 μm generate an evanescent field suitable to efficiently

Optics EXPRESS

photo-switch the fluorophores with an input power of 25 mW. While, for the 600 μm waveguide, 100 mW input power is needed to get the maximum number of localized emitters for a similar imaging area.

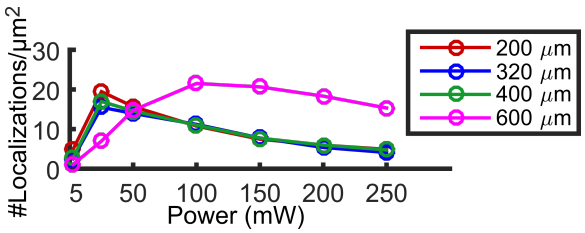

Fig. 2. Localizations as a function of power and width – The average number of localizations over a fixed area for different waveguide widths and input powers. We see that for waveguides 200 - 400 μm wide around 25 mW at the input of the waveguide is enough to get optimum blinking, while for 600 μm waveguide we must increase the power to 100mW.

To systematically investigate the achievable uniformity of chip-based illumination, we measured the intensity profiles acquired by staining the waveguide surface with a dense thin layer of fluorophores (Alexa 647 in Poly-L-Lysine) and diffraction limited imaging by using mode averaging. In Fig. 3(a) the MMI pattern is shown without using mode averaging, while in Fig. 3(b) the same area is imaged after mode averaging. The line-profile in Fig. 3(b) indicate the position from where the modulation depths for different waveguide widths are calculated. The measured modulation depth for waveguide widths stretching between 120 μm up to 1000 μm are shown in Fig. 3(c) using 500 frames of data, with Fig. 3(d) showing the line-profile from Fig. 3(b) as an example. When calculating the modulation depth, the edge artifacts observed in Fig. 3(d) are neglected. Interestingly, it was observed that the modulation depth for these dimensions are rather stable in terms of being viable for *d*STORM imaging, with around 17 % for the 120 μm and up to 27 % for 1000 μm wide waveguides.

We demonstrate the method by imaging liver sinusoidal endothelial cells (LSECs) stained for the micro-tubules network. The *d*STORM localization list was filtered to only keep the localizations with the best statistics, like brightness and shape, ensuring that few overlapping emitters introduce errors for the fitting algorithm. The number of images used to compile the reconstructed image was around 25000 selected from a stack of 65000 images acquired. The image shown in Fig. 4(a) show that by using the 25x 0.8 N.A. objective lens an extremely large area of almost 500 μm x 500 μm with a resolution down to 70-75 nm can be imaged. The large area illuminated by the waveguide allow 200-300 cells to be imaged simultaneously. The zoom in Fig. 4(b) show the comparison to the diffraction limited image visualizing a 6-fold resolution enhancement of the 25x 0.8 N.A objective lens. In Fig. 4(c) the zoom also indicates the position of the lineplot in Fig. 4(d) which show a clear separation of tubulin filaments located 78 nm apart. In Fig. 4(e), this resolution is confirmed using Fourier ring correlation [20], which suggest a lower threshold for the resolution over the entire image to be around 72 nm. Furthermore, we see that the average localization precision in the image, as measured by the reconstruction software is peaking around 23 nm (Fig. 4(f)), indicating a lower limit for the resolution of around 65 nm.

It can be noticed from Fig. 4(a) that a slight decay in the number of localized molecules towards the edges of the image, which is caused by the limited field flatness of the imaging objective lens. To study the influence of field flatness of the imaging objective lens, we investigated the achieved localization precision as a function of position in the field of view. As it can be seen from Fig. 3(c), the waveguides can set up an evanescent field where the intensity modulation depth is around 25 % for large fields of view. However, when producing really large high-resolution images we are still limited by the collection optics. Microscope objectives with high numerical aperture

Optics EXPRESS

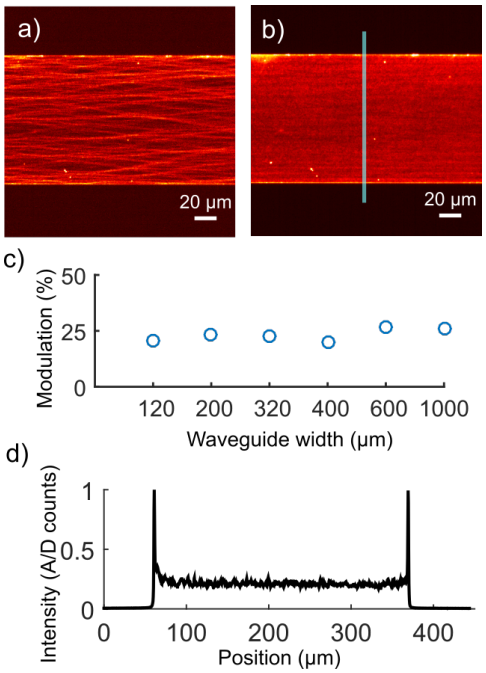

Fig. 3. Modulation depth as function of waveguide width – a) Illumination MMI pattern without mode averaging. b) After mode averaging the resulting illumination is close to uniform. c) The modulation depth is plotted for different waveguide widths, and only small changes is observed when the width increases. d) The line-profile indicated in b). When calculating the modulation depth the edge artifacts are ignored.

and low magnification are not very common, and the ones that do exists typically have to pay the price for these unusual characteristics in terms of field flatness. Most microscope objectives expressing these characteristics give a nice focus only in the middle of the FOV. Fig. 5 shows the localizations from the image in Fig. 4(a) grouped in bins of 10 μm along x (horizontally) but with the full field-of-view along y (vertically). The number of localization detected for each bin is displayed, visualizing how the number of localizations decrease when moving away from the center. The likelihood of acquiring a good localization is decreasing when the emitter is laying in the periphery of the FOV, which means that either we need to accept a decrease in resolution (keeping less good localizations), or we need to increase the acquisition time to allow enough localizations to be captured to fully resolve the structures at acceptable resolution.

5. Discussion and conclusion

Super-resolution microscopy has so far come at the cost of throughput. Currently, commercial setups provide unprecedented resolution but the size of the field of view is small, with images typically covering only parts of a cell. This is a consequence of conventional setups being bound to a high N.A. and high magnification objective lens for both the illumination and the collection. To make use of optical nanoscopy to study statistical biological nanometer sized phenomenon on large length scales, the need to increase the throughput of the methods is apparent. In this study we used planar optical waveguides as a mean to illuminate fluorescently labeled specimen located on top of the waveguide surface via intrinsic evanescent fields. This method of exciting fluorescence via planar waveguides allows for TIRF optical nanoscopy with the additional feature of a free choice of the imaging objective lens, allowing scalable super-resolution microscopy

Optics EXPRESS

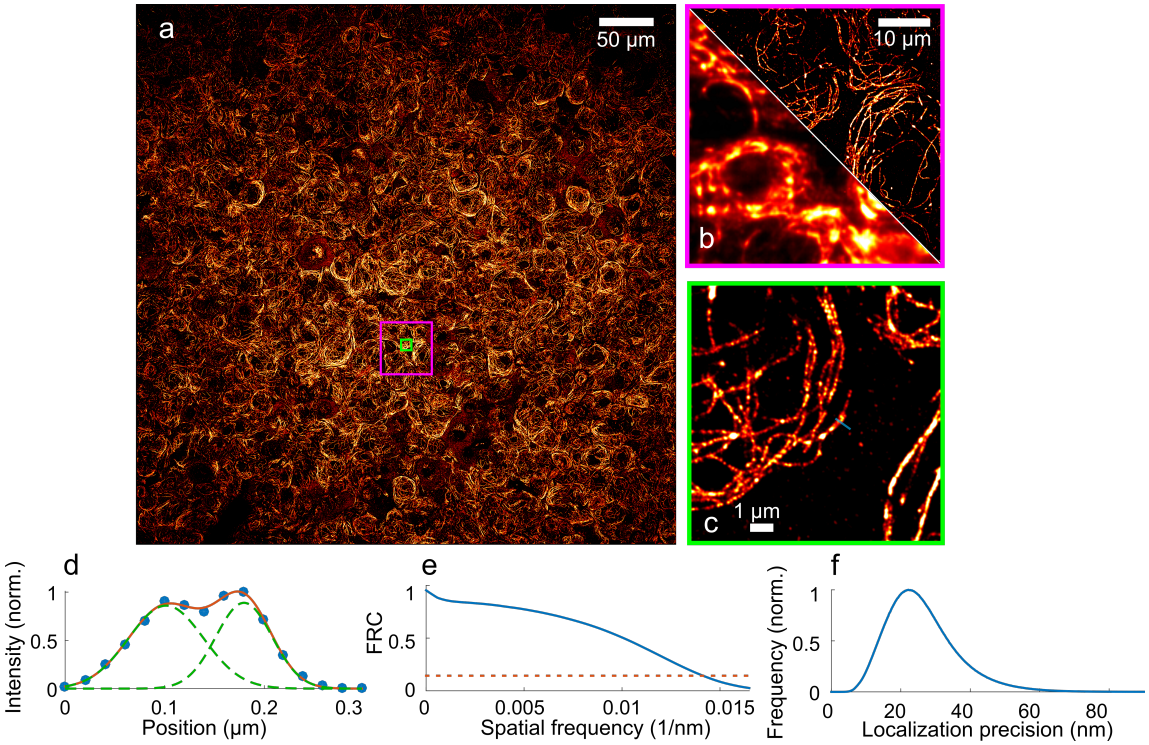

Fig. 4. a) Large field of view *d*STORM image of Alexa 647 stained tubulin in rat L SECs. The image has a resolution of around 70-75 nm with 200-300 cells being imaged simultaneously. b) Zoomed image from a) with comparison to the diffraction limited image. c) Zoomed image marked in green from a) with the position of the lineplot shown in d) marked. d) The lineplot show tubulin filaments clearly separated by a distance of 78 nm. e) Fourier ring correlation indicated a resolution of around 72 nm. f) The localization precision measured by the reconstruction software further backs a resolution between 70-75 nm.

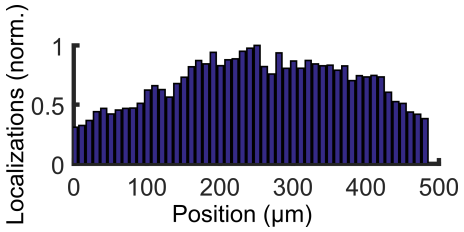

Fig. 5. Localizations from Fig. 4 as function of width across the field of view. Each data point includes all localizations within a bin width of 10μm horizontally separated . We see that the number of properly localized molecules decrease moving away from the center of the objective lens.

Optics EXPRESS

with a compromise between FOV size and resolution.

Compared to the standard coverglass/glass slide arrangement, the PIC chips are more expensive to make. However, when mass produced using CMOS fabrication processes and in a foundry the price per chip can be reduced significantly. The price range of a few dollars per millimeter square can easily be achieved during industrialized production. As the price for silicon wafers scales with the chip area, hosting a small chip (e.g. 2 x 2 mm^2) inside a plastic holder could be an alternative for easy handling of the chip.

The previously published results [15] using the chip-based approach greatly enhanced the size of the field of view available for nanoscopy imaging, but with the resolution not exceeding more than 130 nm. In this work, we show that the method is capable of generating images with 70-75 nm resolution, by carefully selecting the objective lens used in the image acquisition. The increased resolution surpasses the possible 100 nm resolution achievable using SIM. Other previously reported techniques [13, 14] on increased FOV SMLM have achieved a more uniform excitation light spanning over a larger area, but they are still limited by the high N.A. objective lens for acquiring the emitted fluorescence, effectively limiting the FOV to around 200 μm x 200 μm at best.

Furthermore, we investigated how the blinking of fluorophores on waveguides react to different parameters such as waveguide width and laser intensity. As seen from Fig. 2, the switching rates was at its best at 25 mW input power using a single molecule surface with widths of 200-400 μm but a 4 times increase in power was needed to get equally good blinking from a 600 μm waveguide. The surface intensity scales with the width of the waveguide, justifying the need for more input power at 600 μm width, but other factors like coupling efficiency could also impact the curves of Fig. 2. It has been shown that Alexa 647 exhibits faster switching kinetics at high powers [21]. The drop in the number of localizations found above 25 mW (for 200-400 μm) and 100 mW (for 600 μm) could indicate that the fluorophores are blinking much faster than the exposure time of the camera giving increased background. It might also be that the increased intensity is pushing more fluorophores in to more long lived dark-states or to a permanent off-state by photo-bleaching. In either case, laser powers above 25 mW is too strong for efficient SMLM on waveguides using the *d*STORM method, and that the surface intensity is higher than earlier estimates [15], where it was shown that an input laser power of 500 mW yielded up to 10kW/cm^2 evanescent field i ntensity. From experimental data using cells we have experienced that the intensity needed to efficiently photo-switch Alexa 647 must be scaled up a few times to achieve adequate blinking in cells. This is probably due to fluorophores sitting tens of nanometers or more away from surface in case of cells, while the illumination is exponentially decaying away from the surface.

The modulation depth of the resulting illumination pattern after mode averaging was studied. In *d*STORM imaging the modulation depth plays a role in terms of the pattern being viable for use with the *d*STORM technique. As long as there is sufficient intensity to effectively photo-switch the fluorophores, the modulation has little impact. However if intensity reduces in some regions to such an extent that the photo-switching is affected, this can create a problem. For waveguides of 120 μm a modulation depth of 17% which corresponds well with earlier investigations, and for wider waveguides we see that the number increase to 25-30%. When looking at the *d*STORM image of Fig. 4(a) we see that this plays little role in the end result. However, the temporal resolution might be reduced if the modulation is decreased, in that more fluorophores in general will be in the desired on/off state at each instance. To reduce the modulation index for wide waveguides the scan range could be increased to scan over the entire input width, contrary to 20μm as achieved here. The waveguide could also start at a lower width, and taper out to wide dimension to reduce the need for larger scan range.

The chip-based platform also supports different on-chip optical modalities such as Raman spectroscopy on chip [22], on-chip micro-particle manipulation [23], interferometric microparticle

sensing [24] and gas sensing [25], where several of these techniques can be combined creating advanced lab-on-a-chip multimodality platforms. In this work, we have investigated the relationship between waveguide widths and some parameters related to extending the FOV in super-resolution microscopy imaging. By using the waveguide-chip we have by-passed the need of a conventional objective lens to generate the excitation light, however we still reply on using an objective lens to collect the fluorescence s ignal. The impact of chip-based nanoscopy will be further enhanced if we can replace the objective lens with a micro-lens array to collect the fluorescence s ignal. Such a system will not only be highly compact [26] but will also benefit from the extra-ordinary large illumination area as the waveguide can excite fluorescence along its entire length. Furthermore, the resolution of chip-based SMLM is determined by the SNR of the detected single-molecule emissions. By using brighter emitters the resolution can be further improved, e.g using DNA-paint probes [27], where a fluorophore in the ideal case emits all of its photons in one localization event, thus improving the localization precision.

Large field of view nanoscopy will be useful in diagnostic pathology [28]. For non-diffusive diseases, large areas need to be scanned looking for rare events like cancer cells. Pathology mainly focus on thin tissue sections either 4 μm paraffin embedded samples or 100-200 nm cryo-preserved tissue samples. Thin tissue sections are perfectly matched for the large area TIRF illumination produced by the chip-based imaging technology and will be explored in future work.

Funding

European Research Council, project number 336716.

Acknowledgments

This work has made use of the Spanish ICTS Network MICRONANOFABS partially supported by MEINCOM.

References

1. J. Goodman, *Introduction to Fourier Optics* (Roberts & Company, 2005), pp. 156–160.
2. S. Weisenburger, D. Boening, B. Schomburg, K. Giller, S. Becker, C. Griesinger, and V. Sandoghdar, "Cryogenic optical localization provides 3d protein structure data with angstrom resolution," Nat. Methods **14**, 141–144 (2017).
3. S. W. Hell and J. Wichmann, "Breaking the diffraction resolution limit by stimulated emission: stimulated-emission-depletion fluorescence microscopy," Opt. Lett. **19**, 780–782 (1994).
4. M. Heilemann, S. van de Linde, M. Schüttpelz, R. Kasper, B. Seefeldt, A. Mukherjee, P. Tinnefeld, and M. Sauer, "Subdiffraction-resolution fluorescence imaging with conventional fluorescent probes," Angew. Chem. Int. **47**, 6172–6176 (2008).
5. M. J. Rust, M. Bates, and X. Zhuang, "Sub-diffraction-limit imaging by stochastic optical reconstruction microscopy (storm)," Nat. Methods **3**, 793–796 (2006).
6. S. T. Hess, T. P. K. Girirajan, and M. D. Mason, "Ultra-high resolution imaging by fluorescence photoactivation localization microscopy," Biophys. J. **91**, 4258–4272 (2006).
7. E. Betzig, G. H. Patterson, R. Sougrat, O. W. Lindwasser, S. Olenych, J. S. Bonifacino, M. W. Davidson, J. Lippincott-Schwartz, and H. F. Hess, "Imaging intracellular fluorescent proteins at nanometer resolution," Science **313**, 1642–1645 (2006).
8. T. Dertinger, R. Colyer, G. Iyer, S. Weiss, and J. Enderlein, "Fast, background-free, 3d super-resolution optical fluctuation imaging (sofi)," Proc. Natl. Acad. Sci. U.S.A **106**, 22287–22292 (2009).
9. I. Yahiatene, S. Hennig, M. Müller, and T. Huser, "Entropy-based super-resolution imaging (esi): From disorder to fine detail," ACS Photonics **2**, 1049–1056 (2015).
10. K. Agarwal and R. Macháň, "Multiple signal classification algorithm for super-resolution fluorescence microscopy," Nat. Commun. **7**, 13752 (2016).
11. M. G. Gustafsson, "Surpassing the lateral resolution limit by a factor of two using structured illumination microscopy," J. Microsc. **198**, 82–87 (2000).
12. L. Zhu, W. Zhang, D. Elnatan, and B. Huang, "Faster storm using compressed sensing," Nat. Methods **9**, 721–723 (2012).
13. J. Deschamps, A. Rowald, and J. Ries, "Efficient homogeneous illumination and optical sectioning for quantitative single-molecule localization microscopy," Opt. Express **24**, 28080–28090 (2016).

Optics EXPRESS

14. A. Beghin, A. Kechkar, C. Butler, F. Levet, M. Cabillic, O. Rossier, G. Giannone, R. Galland, D. Choquet, and J.-B. Sibarita, "Localization-based super-resolution imaging meets high-content screening," Nat. Methods **14**, 1184–1190 (2017).
15. R. Diekmann, Ø. I. Helle, C. I. Øie, P. McCourt, T. R. Huser, M. Schüttpelz, and B. S. Ahluwalia, "Chip-based wide field-of-view nanoscopy," Nat. Photonics **11**, 322–328 (2017).
16. J.-C. Tinguely, Ø. I. Helle, and B. S. Ahluwalia, "Silicon nitride waveguide platform for fluorescence microscopy of living cells," Opt. Express **25**, 27678–27690 (2017).
17. M. Ovesný, P. Křížek, J. Borkovec, Z. Švindrych, and G. M. Hagen, "Thunderstorm: a comprehensive imagej plug-in for palm and storm data analysis and super-resolution imaging," Bioinformatics **30**, 2389–2390 (2014).
18. S. van de Linde, A. Löschberger, T. Klein, M. Heidbreder, S. Wolter, M. Heilemann, and M. Sauer, "Direct stochastic optical reconstruction microscopy with standard fluorescent probes," Nat. Protoc. **6**, 991–1009 (2011).
19. B. Smedsrød and H. Pertoft, "Preparation of pure hepatocytes and reticuloendothelial cells in high yield from a single rat liver by means of percoll centrifugation and selective adherence," J. Leukoc. Biol. **38**, 213–230 (1985).
20. N. Banterle, K. H. Bui, E. A. Lemke, and M. Beck, "Fourier ring correlation as a resolution criterion for super-resolution microscopy," J. Struct. Biol. **183**, 363–367 (2013).
21. Y. Lin, J. J. Long, F. Huang, W. C. Duim, S. Kirschbaum, Y. Zhang, L. K. Schroeder, A. A. Rebane, M. G. M. Velasco, A. Virrueta, D. W. Moonan, J. Jiao, S. Y. Hernandez, Y. Zhang, and J. Bewersdorf, "Quantifying and optimizing single-molecule switching nanoscopy at high speeds," PloS one **10**, e0128135–e0128135 (2015).
22. P. C. Wuytens, A. G. Skirtach, and R. Baets, "On-chip surface-enhanced raman spectroscopy using nanosphere-lithography patterned antennas on silicon nitride waveguides," Opt. Express **25**, 12926–12934 (2017).
23. Ø. I. Helle, B. S. Ahluwalia, and O. G. Hellesø, "Optical transport, lifting and trapping of micro-particles by planar waveguides," Opt. Express **23**, 6601–6612 (2015).
24. F. T. Dullo and O. G. Hellesø, "On-chip phase measurement for microparticles trapped on a waveguide," Lab Chip **15**, 3918–3924 (2015).
25. F. T. Dullo, S. Lindecrantz, J. Jágerská, J. H. Hansen, M. Engqvist, S. A. Solbø, and O. G. Hellesø, "Sensitive on-chip methane detection with a cryptophane-a cladded mach-zehnder interferometer," Opt. Express **23**, 31564–31573 (2015).
26. A. Orth and K. Crozier, "Gigapixel fluorescence microscopy with a water immersion microlens array," Opt. Express **21**, 2361–2368 (2013).
27. J. Schnitzbauer, M. T. Strauss, T. Schlichthaerle, F. Schueder, and R. Jungmann, "Super-resolution microscopy with dna-paint," Nat. Protoc. **12**, 1198–1228 (2017).
28. F. Herrmannsdörfer, B. Flottmann, S. Nanguneri, V. Venkataramani, H. Horstmann, T. Kuner, and M. Heilemann, *3D dSTORM Imaging of Fixed Brain Tissue* (Springer New York, 2017), pp. 169–184.

5

Structured illumination microscopy on-a-chip

In chapter 3, the chip-based platform was demonstrated for fluorescence diffraction-limited imaging and in chapter 4 this was extended towards super-resolution imaging on-chip following the SMLM approach. While SMLM such as dSTORM give high spatial resolution enhancement, these techniques are intrinsically slow due to the separation of fluorescent molecules in time. Owing to this, the SMLM techniques are most successfully implemented in fixed samples. On the other hand, SIM can be used in both fixed and living samples due to the high temporal resolution, however, it is a more complicated technique to implement due to the need for the generation and control of the structured illumination. This chapter describes the development of CSIM and shows the first proof-of-principle.

5.1 Introduction

The SIM technique was described in 2.3.5, but a summary will follow for brevity. SIM needs 9/15 images to generate a 2D/3D image with increased resolution. The trick here is to use a sinusoidal excitation pattern, which results in the formation of Moirè fringes observed in the fluorescence response of the sample. The Moire fringes is a result of frequency mixing, due to the multiplication

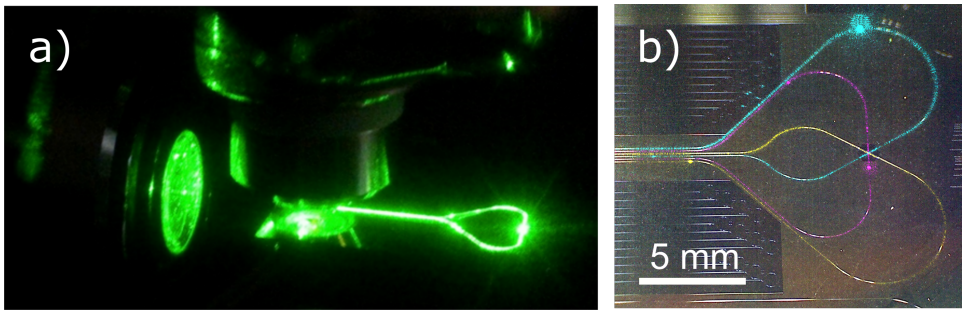

Figure 5.1: (a) Light is guided in a straight waveguide on-chip. The straight waveguide splits in a y-branch forming a loop creating interference suitable to be used as the sinusoidal SIM pattern (image courtesy J.C. Tinguely). (b) Using three identical structures at different orientations represents 3 angles of the SIM pattern, thus isotropic SIM resolution can be achieved.

of the object function with the excitation light function as shown in (2.9), where the frequencies held in the observed Moirè pattern have a theoretical within two times the N.A of the imaging objective lens (2.12). To extract the earlier un-resolved content, three phase-shifts of the sinusoidal excitation light is needed for each orientation of the pattern. The SIM pattern must be rotated three times to achieve isotropic resolution enhancement for 2D SIM. Using three phase-shifts for each of the three orientations yields 9 images in 2D SIM, making the method very fast and suitable for live-cell imaging. However, the resolution enhancement is limited to around 100-130 nm, a consequence of projecting the SIM pattern via the objective lens. Contrary to this, if the excitation light is not projected through the objective lens, the dependency of N.A will be greatly reduced and the SIM technique can be pushed below the earlier stated resolution limit (2.12).

In the conventional implementation of SIM, the patterned excitation light is created and controlled using free-space optomechanical components such as spatial light modulators, phase retarders, and polarization optics. All of which adds to the complexity and bulkiness of the setup, and makes it prone to miss-alignment. The chip-based implementation of SIM offers integration of the optical necessities using Y-junctions, on-chip phase modulation and interference (Fig. 5.1). Also, multiplexing of the channels (wavelengths), and the possibility to provide rapid phase stepping holds the potential for multi-color live-cell CSIM imaging. Furthermore, the fiber-compatibility of the PIC makes it possible to connect the chip with off-the-shelf high-speed telecom devices.

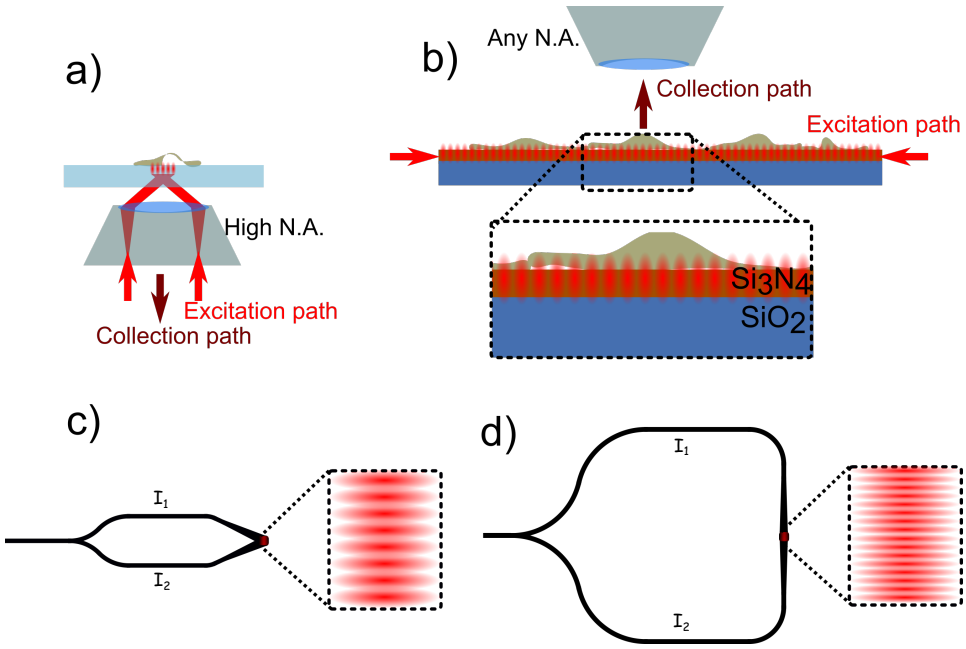

Figure 5.2: (a) In a conventional SIM setup, the SIM pattern is generated via the objective lens, and the signal is captured with the same objective lens. (b) In cSIM the pattern is generated using standing waves in the waveguide, available via the evanescent field. The signal is collected via an objective lens, independent of the SIM pattern. The resolution enhancement available for CSIM is determined by the fringe spacing, which can be controlled using interference at a low angle (c) for medium resolution enhancement, and counter-propagating interference (d) for the best possible resolution enhancement.

5.2 Chip-based SIM

While conventional SIM implementations rely on one objective lens to both excite the specimen and collect the fluorescence (Fig. 5.2(a)), CSIM creates interference in the waveguide and the interference pattern is used as excitation light for SIM (Fig. 5.2(b)). Here, light is guided in separate waveguides on the chip, where after the two waveguides are brought together and a standing wave pattern is formed in the evanescent field due to interference. The idea of using interference has earlier been harnessed for sensing purposes as in [68]. By using waveguides to create a standing wave interference pattern for SIM, the frequency of the pattern will no longer depend on N.A, but rather on the effective refractive index n_f (2.13) (i.e a material property), the angle of interference θ and the wavelength λ (as conventional SIM also do).

5.2.1 The resolution of CSIM can overcome conventional methods

In the waveguide implementation of SIM, light is split in two arms with intensity I_1 and I_2 (Fig. 5.2(c,d)) to create interference, the resulting intensity distribution can be described (in 1D) by:

$$I(x) = I_1 + I_2 + 2\sqrt{I_1 I_2}\cos\left(\frac{1}{\Lambda}x + \Delta\phi\right), \tag{5.1}$$

where ϕ is the phase of the interference pattern, and the fringe period Λ is given by:

$$\Lambda = \frac{\lambda}{2n_f \sin(\frac{\theta}{2})}, \tag{5.2}$$

where θ is the angle between the two waveguides that are creating the interference, λ is the free space wavelength and n_f is the effective refractive index (2.13).

The possible resolution enhancement of CSIM can be found if we continue the discussion from section 2.3.6. The OTF determines the frequencies accepted by the microscope, i.e the resolution. We can use the abbe limit (2.4) as the highest frequency that can be observed, i.e

$$k_{diff.lim} = \frac{2NA}{\lambda}.$$

By using conventional SIM, the OTF is extended to a maximum of twice the abbe limit, i.e

$$k_{sim} = \frac{4NA}{\lambda},$$

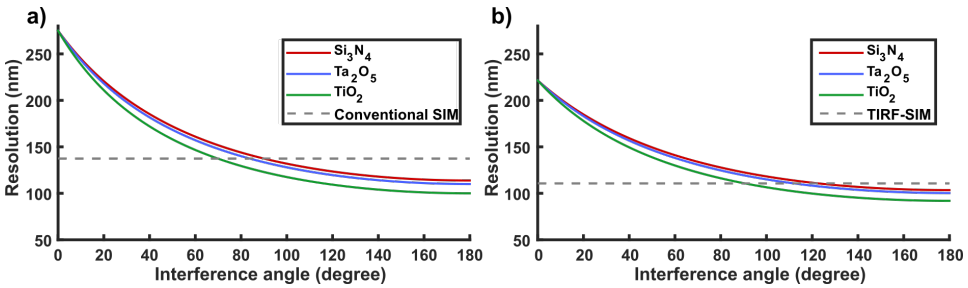

Figure 5.3: The resolution of CSIM is plotted for the different materials Si_3N_4, Ta_2O_5 and TiO_2, with estimated parameters $n_f = 1.7, 1.8$ and 2.1, respectively. The excitation wavelength is 660 nm. (a) Shows the case for N.A=1.2, which is what we have used in this version of CSIM, while (b) shows the case of using TIRF objective lens having N.A=1.49.

since the SIM pattern is generated via the objective lens and thus is itself diffraction-limited.

By using waveguide interference, the fringe spacing is determined by (5.2). In this case the SIM resolution can be stated as:

$$k_{csim} = \frac{2NA}{\lambda} + \frac{2n_f sin(\frac{\theta}{2})}{\lambda} = \frac{2(NA + n_f \sin(\frac{\theta}{2}))}{\lambda}, \tag{5.3}$$

whereby the introduction of the waveguide to generate a standing wave, the resolution enhancement is shifted from N.A. to n_f. By using high index materials, n_f can be larger than N.A., and thus produce SIM images with increased resolution over the conventional approach (2.12) (i.e $k_{cSIM} > k_{sim}$).

Figure 5.3(a) shows the effect of using different waveguide materials for CSIM. The wavelength was $\lambda = 660$ nm and N.A.=1.2, the same parameters used for the CSIM experiments. The dotted line represents conventional objective-based SIM. The resolution of CSIM overcomes conventional SIM for interference angles above 60-100 degrees, depending on the waveguide material. Figure 5.3(b) show the comparison of CSIM with TIRF-SIM, which yields the best resolution SIM, due to N.A.=1.49. Also here CSIM has increased resolution over the conventional method.

All the experiments in this thesis using CSIM were performed using Si_3N_4 with 660 nm excitation light, which yields $n_f \approx 1.7$, for 4 nm rib waveguides, with 150 nm core thickness.

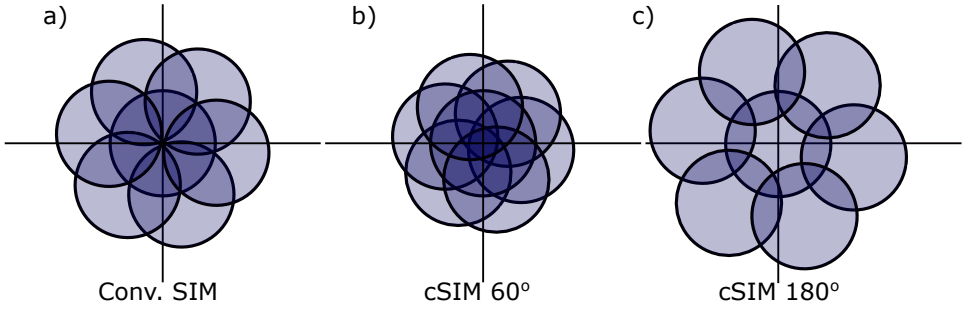

Figure 5.4: Resolution enhancement of SIM in Fourier domain for (a) conventional SIM, (b) CSIM at 60° interference and (c) CSIM at 180° interference. The wavelength is 660 nm and N.A.=1.2. The resolution enhancement of using 60° interference is about 15 % less than the conventional approach, while using 180° interference yields around 20 % better resolution, for these parameters.

5.2.2 Controllable resolution enhancement

The resolution enhancement of CSIM can be controlled by the fringe spacing given by the interference angle, as seen in (5.3). Using waveguides that interfere at a low angle, the resolution of the method is less than for interference at large angles as can be seen from Fig.5.3. For the best possible resolution, the waveguides should be interfering at 180°. Figure 5.4 shows how the resolution is expanded in frequency space as a result of using different SIM methods. It can be seen that the CSIM approach using 60° interference (Fig. 5.4(b)) yields around 15 % less resolution than the conventional approach (Fig. 5.4(a)), while by using 180° interference angle (Fig. 5.4(c)) yields around 20 % improvement over the conventional method.

5.2.3 Phase-shifting strategies for CSIM

As discussed in section 2.3.5, the SIM patterns phase must be shifted so that three images of different phases can be acquired for each of the three pattern rotations. This implies that $\Delta\phi$ in (5.1) should have a new value for each image. Ideally, the phase should be shifted by equal amounts between each image, i.e $\frac{2\pi}{3}$, to reduce the chance of reconstruction artifacts.

Techniques for phase-shifting the standing wave interference pattern were investigated using three different approaches and waveguide geometries. Here the three methods are discussed using CSIM structures that can extend the resolution along one direction only, and with 180° interference angle, in order to make the figures (Fig. 5.5) easier to interpret.

Option 1: Off-chip phase modulation

The first option is to use two independent waveguides, each with its own input beam. By changing the phase of one input beam a relative phase shift can be achieved. For this, the waveguide layout shown in Fig. 5.5(a) was used. Here, light is coupled on to a 50:50 fiber-split on the optical table and the two fibers are coupled on to the waveguide structure. The structure thus consists of two input waveguides that form a loop and creates the interference pattern. To change the phase of the interference pattern, one of the fiber was pinched between two fingers, which invoke a phase change that can be described by:

$$\Delta\phi = \phi_1 - \phi_2 \ = \frac{2\pi}{\lambda}\left(L_1\frac{dn_{f_1}}{dT} - n_{f_2}L\right), \tag{5.4}$$

where L_1 is the interaction length of the pinch. $\frac{dn_{f_1}}{dT}$ is the change in refractive index in the active (pinched) arm, due to the heat transfer from the pinch. There might be additional vibrations/deformations causing phase-change due to the force put on the fiber. $n_{f_2}L$ is related to the passive arm, and does not change. The thermo-optic coefficient ($\frac{dn}{dT}$) relates heat-change to the change in refractive index.

This method was used as a proof of concept (figure 3 in paper 5), but it lacks speed and repeatability needed for a full implementation of CSIM. Additionally, since the light is split outside the chip, environmental factors played a role in the stability of the phase.

Option 2: On-chip phase modulation

By using three interference structures merging at the region of interest (ROI) (Fig. 5.5(b), and by letting the three structures have different path lengths, the phase of the interference pattern could be discretely stepped following:

$$\phi_i = \frac{2\pi l_i n_f}{\lambda}, \tag{5.5}$$

where l_i are the lengths of the three ($i = 1, 2, 3$) waveguide loops. The effective refractive index n_f of the two arms on each waveguide is the same (no openings in the cladding).

The phase change is thus induced by having different lengths l_i. Since each of the three structures in Fig. 5.5(b) have different l_i, there will be three values of

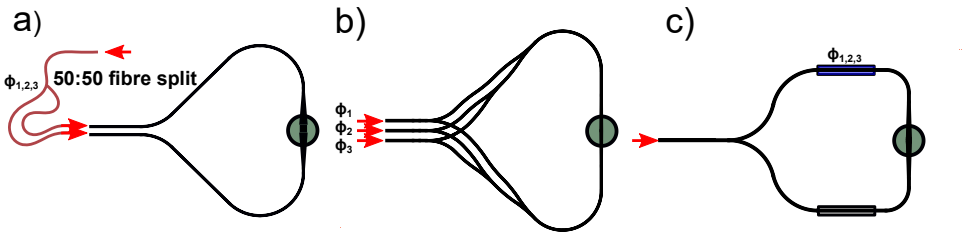

Figure 5.5: (a) Light is split outside the chip using a 50:50 fiber split. The two fibers were coupled on to the chip to yield interference. The phase was controlled by locally heating one of the fiber arms. (b) Alternatively, the light was split on the chip creating a phase-stable interference pattern. By choosing different waveguides at the coupling facet, the phase of the pattern was change by having different optical path lengths in the three waveguide loops. (c) On-chip thermo-optical phase stepping was achieved by heating a polymer in contact with the waveguide core located on one of the two arms.

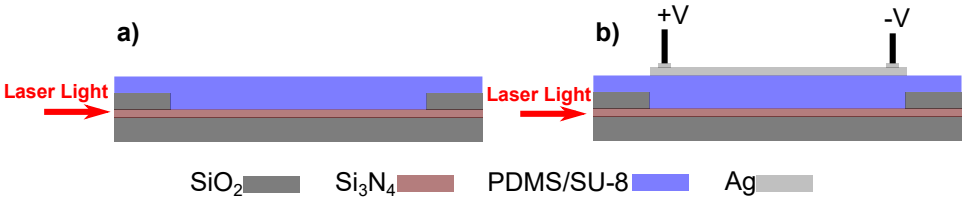

Figure 5.6: For thermo-optical phase modulation, each loop arm has an opening in the cladding material exposing the waveguide. (a) On one arm, a polymer is applied to the surface. (b) On the other arm, the polymer has an electrical conducting silver circuit on top, working as a resistor which heats the polymer underneath. The result is a change in the refractive index causing a phase change of the sim pattern.

$\Delta\phi$. For this structure, the phase difference $\Delta\phi$ is pre-determined and cannot be changed.

Option 3: On-chip thermo-optical phase modulation

Figure 5.5(c) shows a simple loop structure where both arms have openings in the cladding. In the opening, a layer of either PDMS or the photo-resist SU-8 was deposited, and on top of this, a conductive layer of silver is placed on one of the arms (Fig. 5.6). When a voltage is applied to the silver layer, the resistance to the current heats the PDMS/Su-8 underneath and invokes a change in n_f on the active arm the waveguide loop structure, while the other arm remains passive. The phase change of the CSIM pattern thus follows (5.4) where L_1 is the length of the cladding opening, and $n_{f_2}L$ is related to the phase of the passive arm, which does not change. The chip was mounted on a heat sink to reduce the impact of heat accumulating in the silicon chip.

5.3 Results and discussion

CSIM imaging was demonstrated using the waveguide structures depicted in Fig. 5.7. The proof-of-concept image (figure 3 in paper 5) was generated using phase changing option 1, with 60° interference between the waveguides (Fig .5.7(a)). This gave a standing wave pattern with a fringe spacing of around 400 nm, which is within the observable range using N.A.=1.2 objective lens. Choosing this fringe spacing gave a measurable resolution in the image down towards 200 nm, around 35-40 % improvement over the diffraction limit. However, the phase of the CSIM pattern was experienced to be fluctuating with the room environment. It is thus more desirable to use a common path waveguide structure, where the light is split on the chip under the protective cladding material, which give a phase-stable interference pattern (supplementary figure 5 in paper 5).

Thermo-optics for CSIM

Using thermo-optical phase modulation (option 3 above), a 2D CSIM structure takes the form depicted in Fig. 5.7(b). Here, the common-path idea is used, ideally giving a stable phase of the interference pattern. Unfortunately, when designing this structure, we did not anticipate the bulkiness of the wire connections needed to connect the voltage supply to the heating elements. This led to the collision of the microscope objective lens (used for acquiring the image) with the wire connection sites, hindering the simultaneous use of the three waveguide structures. We made attempts of fixing this by testing different options to mount the wires to the chip, but finally, we were forced to retract the wire sites to the periphery of the chip. The sputtered silver elements thus increased in size to reach the connection sites, which again led to destructive heating of the chip. We experienced large thermal fluctuations both in the laser input coupling and the focus of the collection optics, which we could attribute to the thermal expansion of the silicon chip. The silicon chip was 0.5 mm thick with a thermal expansion coefficient $0.27x^{-6}(\mu m/m)/^{\circ}C$. However, even though thermo-optics phase modulation was not fully optimized, CSIM imaging could still be demonstrated (supplementary figure 8 of paper 5).

The choice of the active layer was made based on the availability within the group. We first tested PDMS, which has a relatively easy deposition process and can be removed completely from the chip surface if needed. The thermo-optical coefficient of PDMS is $\frac{dn}{dt} = -4.5x10^{-4}/^{\circ}C$ [69]. Supplementary figure 6 show that we could do a π-change using PDMS with a few milliamperes of current. This result was achieved with the silver resistors positioned perfectly above the cladding opening (as depicted in Fig. 5.6(b)), which was not doable for all the three arms simultaneously due to the space limitations. Additionally,

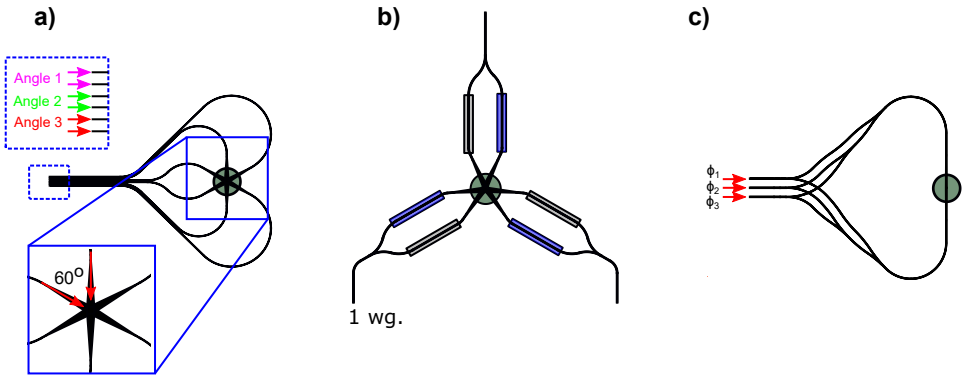

Figure 5.7: Three different CSIM designs were used in this work. (a) Using off-chip phase change (option 1) with 60° interference angle (figure 3 in paper 5). (b) On-chip thermo-electric phase change (option 3) with 50 ° interference angle. (a) and (b) can provide three orientations of the CSIM pattern. (c) On-chip path-length stepping (option 2) with 180° interference angle. This structure gives CSIM resolution enhancement along 1 direction (figure 4 in paper 5).

the resistance in the silver heating elements was fluctuating a lot and the circuit would break completely. The difference in thermal expansion coefficient between PDMS and silver is large, and possibly causing the silver layer to crack. We also had problems maintain the wire connections on the PDMS layer, due to the low adhesion of the silver epoxy against the PDMS.

Su-8 is a polymer photo-resist which is transparent at visible wavelengths. The thermo-optic coefficient is $\frac{dn}{dt} = -1.1x10^{-4}/°C$ [70]. Using Su-8, the problems of cracking the sputtered silver resistors reduced, and the chip could be used many times. However, large current was needed to yield any phase change causing thermal drift by heating of the chip. We believe that this problem is related to non-localized heating due to the shifted wire connection sites. This might induce heat exchange via the silicon wafer, affecting the passive arm.

CSIM overcomes the resolution barrier of SIM

Using the phase-shifting strategy outlined as option 2, and the CSIM waveguide structure depicted in Fig. 5.7(c), CSIM with increased resolution over conventional SIM was demonstrated (figure 4 in paper 5). Here, counter-propagating waveguides yield the smallest fringe spacing as stated in (5.2), and the resolution can overcome the conventional method as seen in Fig. 5.3 and Fig. 5.4.

The fringe period that was achieved using this structure was around 195 nm

(for 660 nm excitation), so the fringes were not visible to the microscope due to the diffraction limit. We verified the presence of the standing wave by directly imaging it using dSTORM on the fluorescently labeled waveguide surface. Furthermore, by changing between the three different phase steps, we could get an estimate for the phase change given by the three input waveguides. This was later beneficial in the reconstitution of the image. The image resolution measured in the CSIM reconstruction was around 117 nm, which is around 2.3x over the diffraction limit.

5.3.1 Outlook

The work on CSIM is still ongoing. Although we have shown the proof-of-principle, the technology is far from finalized. The goal is to perform video-rate imaging using CSIM. In this sense, phase-changing option 1 is not viable for obvious reasons.

In future work, we will explore option 2 an option 3. To alleviate the space-demands for wire terminals, the next designs will incorporate more space between the ROI and resistors. Furthermore, to alleviate problems of non-localized heating, only one of the arm on each waveguide structure will have an opening in the cladding, making this arm experience a different therm-optic coefficient. Another planned design will be without openings in the cladding. This implies sputtering a layer of silver directly on the silica cladding. The thermo-optic coefficient of silica is $\frac{dn}{dt} = +15x10^{-6}/°C$, a small number but perhaps already enough to shift the phase. If this works, it will make the fabrication of the phase-shifter much easier.

Phase change option 2 (Fig. 5.5(b)) gave a fixed phase difference between the three arms. This is positive in the sense that fast switching of phases can be achieved using an external optical switch, without the need for mounting anything on the chip. It is negative in the sense that the phase change is predetermined in the fabrication process. To acquire a 120° phase difference between the arms is difficult since small imperfections would change n_f. To combat the last issue, we plan a structure that will allow tuning of the phase differences by small openings in the arms.

Lastly, the potential to image large FOV is not exploited in this implementation of CSIM. One of the major selling points for chip-based techniques is that the excitation light is independent of the microscope objective lens. To fully appreciate this we should ideally expand the waveguide mode over a larger area. Using adiabatic tapering this is possible but at the cost of chip space, since long taper lengths are needed. Another approach is to use narrow, single-mode rib waveguides without tapering. If the ribs are stopped at a pre-determined

location the mode will continue to propagate in the slab, while experiencing divergence. The initial test on this gave around 100 x 100 μm^2 of interference area, contrary to 25 x 25 μm^2 showed in this thesis.

5.4 Paper 5: Structured illumination microscopy using a photonic chip

Submitted to Nature Photonics, August 2019

Authors: Øystein I. Helle, Firehun T. Dullo, Marcel Lahrberg, Jean-Claude Tinguely and Balpreet S. Ahluwalia.

Author contributions: B.S.A conceived the idea and supervised the project. Ø.I.H build the setup, did the experiments, analyzed the data and wrote the majority of the paper. M.L. did the numerical simulations, F.S.D and J.C.T. made the chip masks. All authors contributed to the waveguide designs. All authors reviewed the paper.

Structured illumination microscopy using a photonic chip

Øystein Ivar Helle[1], Firehun Tsige Dullo[1], Marcel Lahrberg[1], Jean-Claude Tinguely[1] and Balpreet Singh Ahluwalia[1]

1 Department of Physics and Technology, UiT-The Arctic University of Norway, 9037 Tromsø, Norway.

Correspondence should be addressed to BSA (balpreet.singh.ahluwalia@uit.no)

Structured illumination microscopy (SIM) enables live cell, 3D super-resolution imaging of sub-cellular structures at high speeds. Present day, SIM uses free-space optical systems to generate pre-determined excitation light patterns and reconstruction algorithms to enhance the spatial resolution by up to a factor of two. These arrangements are prone to miss-alignment, often with high initial and maintenance costs, and with the final resolution-enhancement being limited by the numerical aperture of the collection optics. Here, we present a photonic-chip based total internal reflection fluorescence (TIRF) *c*SIM that greatly reduces the complexity of the optical setup needed to acquire TIRF-SIM images. This is achieved by taking out the entire light generation and delivery from the microscope and transferring it to an integrated photonic-chip. Thus, the conventional glass slide is replaced by a planar photonic chip that both holds and illuminates the specimen. A photonic chip consisting of an array of opposing optical waveguides are used to create standing wave interference patterns in different angles, which illuminates the sample via evanescent fields. The phase of the interference pattern is controlled by the use of either on-chip thermo-optical modulation or by off-chip phase modulation of the interfering beams, leaving the footprint of the light illumination path for the *c*SIM system to around 4x4 cm^2. The photonic chips are fabricated using dielectric materials which enables light guidance and illumination of arbitrary large areas. Furthermore, by harnessing high refractive index waveguide materials, such as silicon nitride, 2.3x resolution enhancement was obtained using cSIM, which is beyond the 2x resolution enhancement of conventional SIM. *c*-SIM represents a simple, stable and affordable approach, which could enable widespread penetration of the technique and might also open avenues for high throughput optical super-resolution microscopy.

The spatial resolution of optical microscopy is bound by diffraction effectively limiting the achievable resolution to around 250 nm laterally, and 500 nm axially[1, 2]. The advent of super-resolution fluorescence microscopy, commonly known as nanoscopy, has proven the ability to trick the diffraction limit extending the lateral resolution of the microscope down towards just a few nanometer[3]. Among the existing optical nanoscopy methodologies[4-9], structured

illumination microscopy (SIM)[10, 11] works for most bright fluorophores. Instead of illuminating a sample with a uniform field, in SIM, a sinusoidal excitation pattern illuminates the sample, and the fluorescence emission is captured on a camera. The sinusoidal excitation light is typically generated using interference of two or three beams at the sample plane. The illumination and object functions combine at the sample plane via a multiplication, which in frequency space represents a convolution, mixing the spatial frequencies of the two functions. In this manner, high frequency, un-resolved, content is made available within the passband of the objective lens due to a frequency down-conversion with the resulting fluorescence emission observed as a Moiré fringe pattern. To extract the high frequency content from the Moiré pattern, three or five phase-shifts of the structured illumination is needed for improving the resolution along one axis. For isotropic resolution, the process must be repeated for 3 orientations (angles) of the excitation pattern, for a total of 9 (15) images in case of a 2D (3D) SIM reconstruction. Since SIM only needs 9 (15 for 3D) images to create a super-resolution image over wide-field of view, this method is inherently fast, making it the most popular method for live cell optical nanoscopy.

The development of high-resolution methods like excitation depletion techniques[4, 5] and single-molecule localization microscopy (SMLM)[6-9], yielding resolution down to a few tens of nanometers, has opened new possibilities for discovery within life sciences[12]. However, to find real statistical meaning, the increase in throughput of super-resolution imaging methods would represent the next leap within nanoscopy. SIM already have the temporal ascendancy over the other methods, and with its ease of use, label compatibility and low photo-toxicity the method points in the direction of real high-throughput nanoscopy. To fully harness the utility of fast SIM imaging technique, the achievable spatial resolution, throughput of the method and the system complexity of SIM would need improvement. In conventional SIM, the illumination and collection light paths are coupled (**Fig 1a**), which limits the resolution and hinders the use of low N.A objectives to be used for large area imaging. Furthermore, the generation of the necessary standing wave patterns are usually done with free-space optics, with components to control and maintain the pattern orientation, phase and polarization state. The resulting SIM microscopes are thus both bulky, expensive, and prone to misalignment needing highly qualified personnel which further adds to maintenance costs. The resolution of SIM can be improved by using speckle-illumination[13-15] and blind-SIM[16-18] reconstruction approaches but it comes with a cost of low-temporal resolution due to the need of large number of images (100s). The speckle illumination methods takes away the main concept of “structured” illumination which helps in minimizing the number of frames needed (9-15) by illuminating the sample with pre-determined and highly structured illumination pattern. Thus, efforts to enhance the resolution of SIM keeping structured illumination is worth pursuing.

SIM on a chip. In this work we propose a method that will allow a standard optical microscope to acquire total internal reflection fluorescence (TIRF) SIM[19-21] images using a mass-producible, photonic chip, with better resolution and possibly increased field-of-view (FOV) over conventional SIM. Chip-based fluorescence microscopy relies on total internal reflection of the excitation light inside planar waveguides on a chip[22-25 26, 27], with a part of the excitation light available as an evanescent field exponentially decaying from the surface of the waveguide. In chip-based SIM (*c*SIM), a low-cost upright microscope can gather super-resolved images of the specimen placed directly on top of a planar waveguide surface (**Fig. 1b**). The waveguide is made from a dielectric material with high index contrast (HIC) (such as silicon nitride, Si3N4). By using the interference of spatially coherent light inside single-mode waveguides, standing wave interference fringes are generated on top of the waveguide surface (**Fig. 1, Supplementary note 1, Supplementary Fig. 1**), which are used to excite fluorescence in the labelled sample. An array of single mode planar waveguides, for example six as shown in **Fig. 1c** enables three rotational angles at the overlapping imaging area. By maneuvering the phase of the standing wave of the respective waveguide arm, the necessary data for a 2D TIRF-SIM reconstruction, i.e. 9 images (3 angles and 3 phases steps) can be acquired. At the imaging location, the single mode waveguides are adiabatically tapered[27, 28] to a large area (400 um^2 in the present study).

The proposed *c*SIM methodology opens up the possibility of pushing the resolution enhancement of the SIM technique beyond 2X, and enables scalable resolution over a scalable large field of view. This can be seen if we first consider the fringe period f_s generated by interference in a waveguide as given by

$$f_s = \frac{\lambda_{ex}}{2n_f \sin\frac{\theta}{2}}$$

where λ_{ex} is the excitation wavelength, n_f is the effective refractive index of the guided mode and θ is the angle of interference. Generating the SIM pattern with a planar waveguide thus contributes n_f in to the achievable resolution Δ_{xy} of the method, so the equation describing the theoretical best resolution for *c*SIM takes the form of

$$\Delta_{xy} = \frac{\lambda_{ex}}{2(N.A. + n_f \sin\frac{\theta}{2})}$$

where N.A. is the numerical aperture of the imaging objective lens. If n_f is larger than the N.A. , the resolution of the method exceeds the resolution of conventional SIM, which would have 4N.A. in the denominator (**Supplementary note 2, Supplementary figure 2**). In *c*SIM, the resolution enhancement can be scaled by changing the fringe spacing of the interference pattern using different pairs of waveguides interfering at different angles (**Fig. 1d,**

Supplementary figure 3, Supplementary note 3). A small interference angle between two waveguides produces a large fringe period and thus a low-resolution enhancement, while opposing pair of waveguides (180° between them) yield a very small fringe period and thus a high-resolution enhancement (**Fig. 1d-f**). Moreover, by using waveguides made of HIC material, (n_f=1.7-2.1) the fringe spacing of the standing wave pattern can be made much smaller than what can be achieved by a high N.A. oil immersion objective lens (N.A.=1.49) in conventional SIM. For Si_3N_4 (n=2) waveguides interfering at 180°, the theoretical resolution enhancement possible for *c*SIM (**Supplementary note 2, Supplementary figure 2**) is around 2.4x above the Abbe resolution limit using an N.A. of 1.2. This can be further increased by the use of other HIC dielectric materials with even higher refractive index such as tantalum pentoxide (n=2.1) or titanium dioxide (n=2.6).

In conventional SIM, a high N.A./magnification objective lens is desirable for high-resolution imaging (to generate small fringe pattern); while a low magnification/N.A. objective lens is required for increasing the FOV and the throughput. Thus, the present solution limits either the resolution or the FOV. In case of *c*SIM, since the contribution of n_f in Eq.2 is independent of the objective lens the method can be extrapolated to work with low N.A. and low magnification objectives (**Supplementary note 3, Supplementary Figure 4**). The shift in frequency space is dictated by n_f but the passband of the objective lens is still governed by N.A, thus the frequency shift would remain the same but more interference angles would be needed to fill any gaps in frequency space (**Fig. 1h-j, Supplementary Figure 4**). In this sense, the output of the method would show the same resolution enhancement as the high N.A case, but with the FOV supported by the lower N.A. imaging objective lens. Noticeably, generating the illumination fringes onto the sample via waveguides also alleviates the problem of refractive index oil mismatching as often arises in objective based SIM.

RESULTS

Since the method relies on interference, the laser light must be split in two paths. This can be done either off-chip splitting the light in a 50:50 fibre split and by using two waveguides simultaneously (**Fig. 2a**), or on-chip using a waveguide y-branch (**Fig. 2b,c**). The on-chip light spilt is less prone to any phase vibration originating from outside the chip and thus produces less phase-noise as opposed to the off-chip fibre split (**Supplementary Figure 5**). A key parameter of any SIM imaging method is the accurate control of the illumination patterns phase. For *c*SIM, three routes are proposed. Firstly, for the design proposed in **Fig. 2a**, off-chip phase shifts can be achieved by local heating of one arm of the fibre split. Alternatively, by using three discrete waveguides y-branches illuminating the same imaging area, but each with a different optical path length creates a relative phase shift between the three waveguides

(**Fig. 2b**). Finally, using on-chip thermo-optics phase shifter concept[29] (**Fig. 2c, Supplementary Figure 6**) a pre-determined phase shift can be imparted. This describes resolution enhancement along one axis (**Fig 2 a-c**), however to achieve isotropic resolution the structures need to be copied and rotated to have three equally spaced orientations of the *c*SIM pattern (**Fig. 2d-h**).

For light splitting off-chip (**Fig.2a**), the fringe spacing can be scaled by coupling in to different waveguides on the same structure (**Fig. 2d**) to create interference at different angles. For light splitting on-chip (**Fig. 2b,c**) separate structures can be used for *c*SIM imaging to achieve interference at different angles (**Fig.2e-h**). The method was experimentally verified by imaging a sample of 100nm fluorescent beads using the *c*SIM structure depicted in **Fig. 2d**, having interference angle of 60°. Here, excitation wavelength of 660 nm was used which for this structure give a fringe spacing around 400 nm. The light was sequentially guided from different rotational angles towards the central area where the *c*SIM interference pattern is overlapping for all orientations (**Fig.3a-c**). The presence of the standing wave with phase shifts was directly observed using a fluorescent dye layer (**Fig. 3d**). The standing wave fringe spacing and orientation was further confirmed by the power spectrum showing a distinct peak at the standing wave frequency (**Fig.3e-g**) with the orientation of the peaks in **Fig. 3e-g** corresponding to **Fig. 3a-c**, respectively. By comparing the diffraction limited images (**Fig. 3h,j**) with the cSIM reconstruction (**Fig. 3i,k**) the resolution enhancement is clearly visible. By drawing a line-profile (**Fig. 3l**) across the intensity distribution marked with a green box in **Fig. 3k**, what appears as a continuous distribution in the diffraction limited image (**Fig.3j**) is clearly observed as two beads in the *c*SIM reconstruction (**Fig. 3k**). The line-profile shows that the two beads are separated by 206 nm, note that this is obtained using an imaging objective lens of N.A. 1.2.

Similarly, thermo-optical phase change using the chip designs shown in **Fig 2h**. was demonstrated. A sputtered silver circuit acting as a resistor locally heated a polymer on top of tone of the arms leading towards the interference region (**Supplementary Figure 7**). The resulting change in the effective refractive index yields a phase change in the standing wave interference pattern. Using this method, the phase can be accurately controlled using small increments in the voltage supplied to the silver circuit (**Supplementary Figure 6**). The rise and fall times to achieve a π shift in the phase of the interference pattern was found to be on the microsecond range, which would allow fast live *c*SIM imaging. We confirmed this method by imaging a 100 nm bead sample and the results are shown in **Supplementary Figure 8**.

Furthermore, we demonstrate that *c*SIM can surpass the resolution enhancement of conventional linear SIM, achieved using opposing pairs of waveguides (interfering at 180 °).

This will generate interference fringes with smaller spacing than what is presently possible using a high N.A. objective lens (e.g. 1.49 N.A.) in conventional TIRF-SIM, and the interference pattern will have a fringe spacing beyond the diffraction limit. Such chip design would enable a resolution enhancement beyond a factor of 2x (as in case of linear SIM). Using the Si_3N_4 waveguide platform and an imaging objective lens of 1.2 N.A. a theoretical resolution enhancement of 2.4x (Supplementary note 1) is possible. 1D counter-propagating waveguides (**Fig. 2b**) was used to investigate this idea. As the fringe pattern were smaller than the diffraction limit of the imaging objective lens, they could not be observed directly. To verify the presence of a sub-diffraction limited standing wave pattern, the surface of the chip was stained using a fluorescent dye and brought in to a blinking state following *d*STORM imaging protocols[30]. This allows a super-resolution image of the evanescent field intensity distribution to be formed, visualizing the standing wave (**Fig. 4a-c, Supplementary Figure 9**). This method both verifies that there is a standing wave present, and importantly confirms the phase stability of the pattern since a *d*STORM measurement consists of thousands of frames over tens of minutes and any phase drift during imaging would have averaged the image making visualization of fringes impossible. A fluorescent bead sample was imaged using both diffraction limited (**Fig. 4 d,f**) and *c*SIM (**Fig. 4e,g**) showing a clear resolution enhancement along one direction. Beads are separable by line-profiles down to around 117 nm **(Fig.4h**), corresponding to 2.3x resolution enhancements while using imaging objective lens of 1.2 N.A. and 660 nm.

DISCUSSION AND CONCLUSION

In this work we have demonstrated a new concept of performing SIM imaging. The main idea is to harness photonic integrated circuits (PICs) to generate the illumination patterns required in SIM instead of using the conventional approach of the objective lens. We outline several advantages of this novel proposed route. Firstly, the photonic chip enables easy generation of user-defined, highly-stable on-chip illumination patterns without needing any free-space optical components. Secondly, by using a photonic-chip the effective refractive index of the guided mode dictates how tightly the light is confined inside the waveguide, allowing for sub-diffraction limited illumination patterns to be formed; as opposed to the high-N.A. objective lens which is diffraction limited. Thirdly, photonic chips made of dielectric materials can generate uniform illumination over arbitrary large areas which is determined by the dimensions (width and length) of the waveguides[25, 26]. This is in contrast to objective lens based illumination that suffers from field-flatness and that generates a illumination pattern with a Gaussian profile over a limited FOV, determined by its magnification. Finally, our proposed *c*SIM is inherently compact and since it is an integrated technology, replying on PICs it will open the avenues for parallelization, automation, high-throughput and miniaturization.

In our proposed method, the entire illumination light path, i.e. light delivery, pattern generation and beam steering are provided using a photonic chip, which can be easily retrofitted allowing any standard microscope **(Supplementary Figure 10**) to acquire super-resolution SIM images (**Fig. 3h-k, 4f-g, Supplementary Figure 8**) Moreover, the proposed setup, together with on-chip light splitting and phase modulation (**Supplementary Figure 5, Fig. 4a-c**) is inherently very stable with minimum bulk optical elements and therefore free from miss-alignment issues. Besides, being compact, we have shown that *c*SIM has the potential to surpass the resolution enhancement provided by conventional objective-based SIM. The interference fringes in *c*SIM are formed at the sample plane using planar waveguides, and are thus not influenced by the imaging objective as is the case when crating the pattern using objective lenses itself. With counter-propagating waveguides made from a HIC dielectric material, the fringe spacing of *c*SIM will be smaller than what can be generated using the high N.A oil-immersion objective lens commonly used, which led to *c*SIM imaging with up to 2.3x resolution enhancement (**Fig. 1, Fig. 4, Supplementary note 1, Supplementary Fig. 9**).

Using simulations we have demonstrated that the chip-based method opens the opportunity of using a low N.A./ magnification objective lens which provides a larger FOV while still maintaining the resolution improvement provided by the waveguide generated illumination pattern (**Supplementary figure 4**). This represent an improvement over conventional SIM, where a use of a low. N.A. objective lens to image large FOV will significantly reduce the supported optical resolution (**Supplementary note 1, Supplementary figure 10**).

Compared to previous approaches where the formation of illumination fringes were shown using surface plasmon interference and localized plasmons[31, 32] with a metal interface, here we demonstrate the advantages of using PICs made of dielectric material. PICs enables easy integration of several optical functions and components such as on-chip splitters, multiplexers, couplers, lens, etc. Moreover, dielectric materials can propagate and delivery light to much longer distances (centimeters, **Fig. 1 c**) as compared to plasmons based on metals. Although, in the present *c*SIM design the imaging area was limited to about 400 um^2, this is not an inherent limitation and the imaging area can easily be expanded using wider adiabatically tapered single mode waveguides[33]. Once the light is coupled, the PICs enables easy manipulation of the light on the chip, opening avenues for user-defined illumination pattern and phase stepping strategies as outlined in **Fig. 1c-d and Fig. 2**. Using PICs we proposed different waveguide designs where light splitting and phase stepping were implemented both off-board (**Fig. 2a,d**) and on-board (**Fig 2. b,c,e-h**) the chip. To maintain stable and repeatable phase steps, the on-chip methods are preferred due to the inherently low phase noise achieved when splitting the light on-chip with waveguides covered by a protective silica top-cladding

(**Supplementary figure 5**). While all the methods for phase-stepping finally worked **(Fig. 3, Fig. 4, Supplementary figure 8**), the methods holding the potential for high-speed imaging are using thermo-optics (**Fig. 2c,f,h**), or on-chip path-length stepping (**Fig. 2b,e,g**). Both of these methods can be made to switch phase very fast, using a voltage supply or fibre-optical switch, respectively. Thus, the final temporal resolution of the method would be dominated by the camera exposure time typically needed for wide-field fluorescence microscopy, which will allow live-speed imaging.

The present implementation of *c*SIM is done using opaque silicon substrates and with an upright microscope equipped with a water immersion objective lens (x60/N.A.1.2). Future, development of *c*SIM will be done using thin transparent substrates. This will enable using an inverted optical microscope configuration equipped with a high-N.A. oil immersion objective lens (e.g. 1.4 instead of 1.2 used in the present study). This will further extend the resolution of *c*SIM, while in the same time keeping the scalability of the method without affecting the benefits of the inverted microscope configuration. Also, in future work, development of 2D SIM with 2.4X resolution enhancement will be studied by designing suitable waveguide geometries.

The chip-based illumination strategy is an lucrative route, although the focus of this work is to report chip-based SIM, it can be foreseen that PICs provides new research directions of performing complex light beam shaping for other nanoscopy methodologies such as stimulated emission depletion microscopy[5, 34] or light sheet microscopy[35]. Intricate waveguide geometries are capable of generating a range of exotic intensity distributions by harnessing multimode light guiding and interference for altogether new illumination strategies within optical microscopy and nanoscopy. Due to the widespread use of microfabrication techniques within mainstream CMOS technology, the fabrication facilities for PICs are already existing, making mass production of photonics chips feasible, with the potential cost per chip could be reduced to just a few Euros.

The relatively new field of on-chip optical nanoscopy could also benefit with the development of on-chip integration of light sources[36] and frequency combs[37], further miniaturizing the optical set-up. Although, on-chip illumination strategy enables excitation over large areas, the light collection is still presently limited by the imaging objective lens. In the future, the marriage of on-chip illumination with micro-lens arrays[38] for light collection could potentially open the avenues for extra-ordinary high-throughput, where illumination and collection both can be done parallel over large areas, completely removing the dependency on a bulky objective lens.

ACKNOWLEDGMENTS

The authors thank Olav G. Hellesø for his inputs on designs and Rainer Heintzmann and Sourov Das, for help with the SIM reconstruction algorithms and design of fibre-optical phase modulator, respectively. This work was supported by the European Research Council (grant no. 336716 to B.S.A.).

COMPETING FINANCIAL INTERESTS

B.S.A. applied for patent GB1705660.7 on SIM-on-chip. The other authors declare no competing financial interest.

AUTHOR CONTRIBUTIONS

B.S.A. conceived the idea and supervised the project. Ø.I.H. built the setup, performed the experiments and analysed the data. J.C.T and F.S.T designed the waveguide mask. All authors contributed towards chip designs. Ø.I.H., F.T.D. and J.C.T characterized the waveguides. F.T.D. and Ø.I.H. fabricated the on-chip thermo-optics for phase modulation. M.L. performed all the simulation of cSIM. Ø.I.H. and B.S.A. mainly wrote the manuscript and all authors commented to the manuscript.

Figure 1 – The concept. (a) Conventional SIM relies on a high N.A. objective lens to both generate the sinusoidal excitation pattern, and to collect the emitted fluorescence. (b) cSIM harness a standing wave interference pattern generated in a planar waveguide to excite fluorescence in samples located directly on top of an integrated photonic chip via evanescent fields. The emitted fluorescence is captured from the top using a microscope. This decouples the excitation and collection light paths compared with the conventional case. (c) The chip used for cSIM have integrated waveguides which interferers at different rotational angles. Here, light inside the different waveguides are shown in pseudo-color. (d) Interference at a low angle between waveguides creates an interference pattern with low fringe spacing, while interference using counter-propagating guided modes yields the smallest fringe spacing. The latter giving better cSIM resolution. (e) The resolution of a microscope is represented in frequency space with the cut-off frequency (Abbe limit) shown with the solid circle. The dotted circle represents the maximum shift of the OTF possible in conventional SIM yielding 2x resolution enhancement. (f) In cSIM different interference angles shifts the OTF according to the fringe spacing of the interference pattern, here shown for Si_3N_4 waveguide material where 100° and 180° interference gives increased resolution over conventional SIM. g) Using materials of even higher refractive index it is possible to scale the resolution even further, here shown with Si_3N_4 ($n\approx2.0$), Ta_2O_5 ($n\approx2.05$) and TiO_2 ($n\approx2.3$). (h) Using a low N.A. objective lens in conventional SIM gives a shift of the OTF corresponding to the N.A., yielding low resolution. (i) In cSIM the excitation and collection light paths are separated, so the shift of the OTF will unaffected by the low N.A, however more interference angles will need to be used to fill the frequency space.

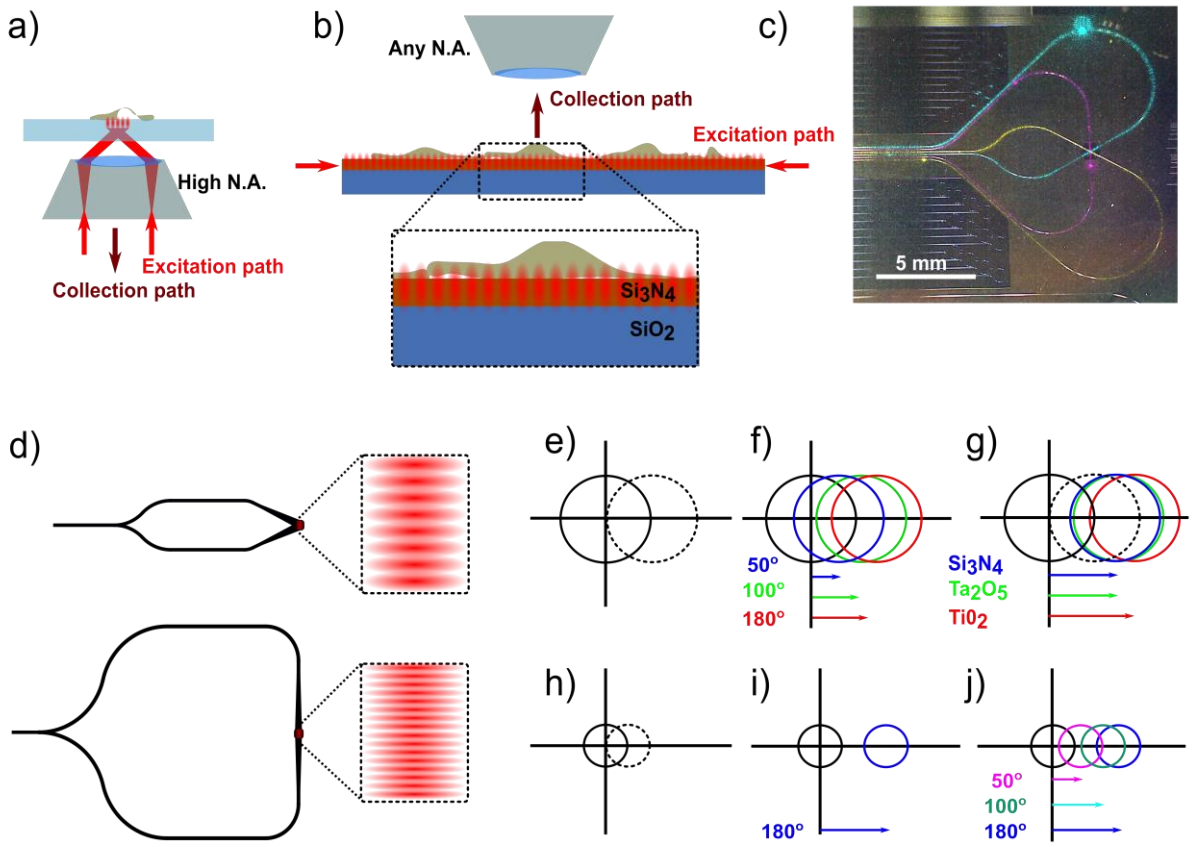
a)
High N.A.
Excitation path
Collection path
b)
Any N.A.
Collection path
Excitation path
Si3N4
SiO2
c)
5 mm
d)
e)
f)
50°
100°
180°
g)
Si3N4
Ta2O5
Ti02
h)
i)
180°
j)
50°
100°
180°

Figure 2 – Waveguide designs for cSIM. (a) Two input waveguides are used to create interference in the image region (marked with a circle). Here, light is split on the optical table using a 50:50 fibre split. This structure will create a 1D cSIM image. For the 2D case the structure needs to be rotated for a total of three rotational angles of the cSIM pattern to get isotropic resolution as shown in (d). Using the structure in (d) different interference angles can be used for scalable resolution, depending on which waveguides are active. b) Light splitting on-chip yields a more phase-stable interference pattern. For this 1D cSIM structure the phase stepping is achieved by coupling light on to three different waveguides merging at the same image area, each with different optical path lengths. To get isotropic resolution the structure must be rotated as shown in (e) for 180° interference, and (g) for 60° interference. c) Using thermos-optics the phase of the interference pattern can be controlled by applying a voltage to a resistive circuit causing heat on of the waveguide arms. A polymer located on the waveguide arm, in contact with the waveguide, will thermally expand giving a change in refractive index which cause the phase change. (f, h) The structure must be rotated to yield isotropic resolution.

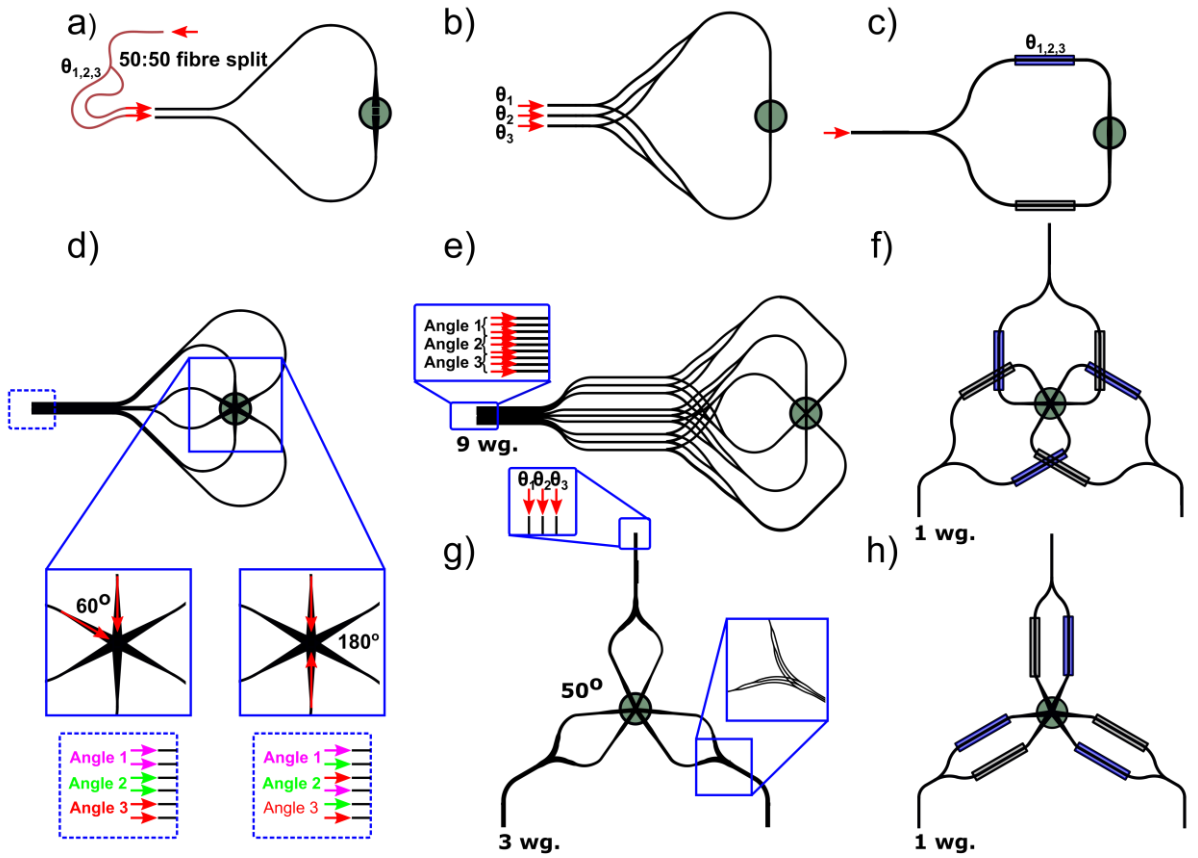

Figure 3 – cSIM imaging. (a) Light is guided in two arms of the waveguide cSIM structure creating interference at 60° where the waveguides meet. (b, c) Different waveguides creates interference with the same fringe spacing at different rotational angles, for isotropic resolution enhancement. d) The cSIM standing wave is directly imaged using a fluorescent dye layer and the line plot show the three phase steps needed for cSIM (20° interference is used for increased contrast). (e-f) The power spectrum, generated by the reconstruction software shows a peak corresponding to the detected standing wave modulation frequency with the orientation corresponding to the orientations standing wave generated in (a-c) respectively. h) Show a diffraction limited, filtered image of a 100 nm fluorescent bead sample while (i) shown the cSIM reconstruction of the same region. A cluster of beads saturates in the centre of the image. (j-k) Show the zoomed images indicated with a white box in (i) with the green box indicating the position of the line-profile shown in (l). Here, two beads located 206 nm apart is resolved using cSIM, but not in the diffraction limited image. The excitation/emission wavelengths used are 660nm/690nm.

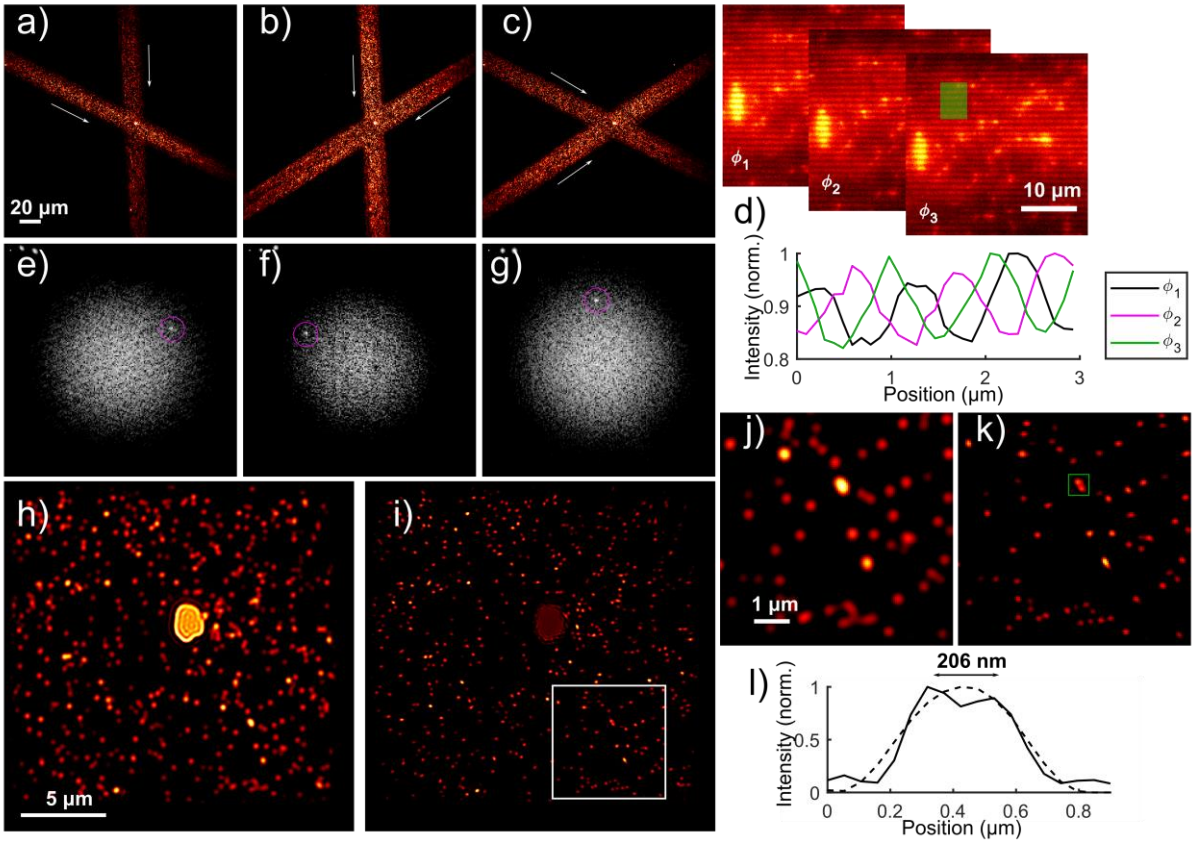
a)
b)
c)
20 μm
d)
ϕ_1
ϕ_2
ϕ_3
10 μm
Intensity (norm.)
1
0.9
0.8
0
1
2
3
Position (μm)
e)
f)
g)
h)
i)
5 μm
j)
k)
1 μm
l)
206 nm
Intensity (norm.)
1
0.5
0
0
0.2
0.4
0.6
0.8
Position (μm)

Figure 4 – cSIM with increased resolution. (a) Counter-propagating light set up a sub-diffraction limit interference pattern not visible using a fluorescence dye layer. (b) The presence of the standing wave is confirmed using *d*STORM imaging of the fluorescent dye layer, visualizing the standing wave having a fringe spacing around 195 nm (c). (d, e) The same 1D structure was used for cSIM, with diffraction limited and 1D cSIM images shown respectively. (f, g) show the zoom indicated with a white box in (d), with a line profile (h) demonstrating two beads separated by 117nm which corresponds to 2.3x resolution enhancement using cSIM. Excitation and emission wavelengths are 660 nm/690 nm.

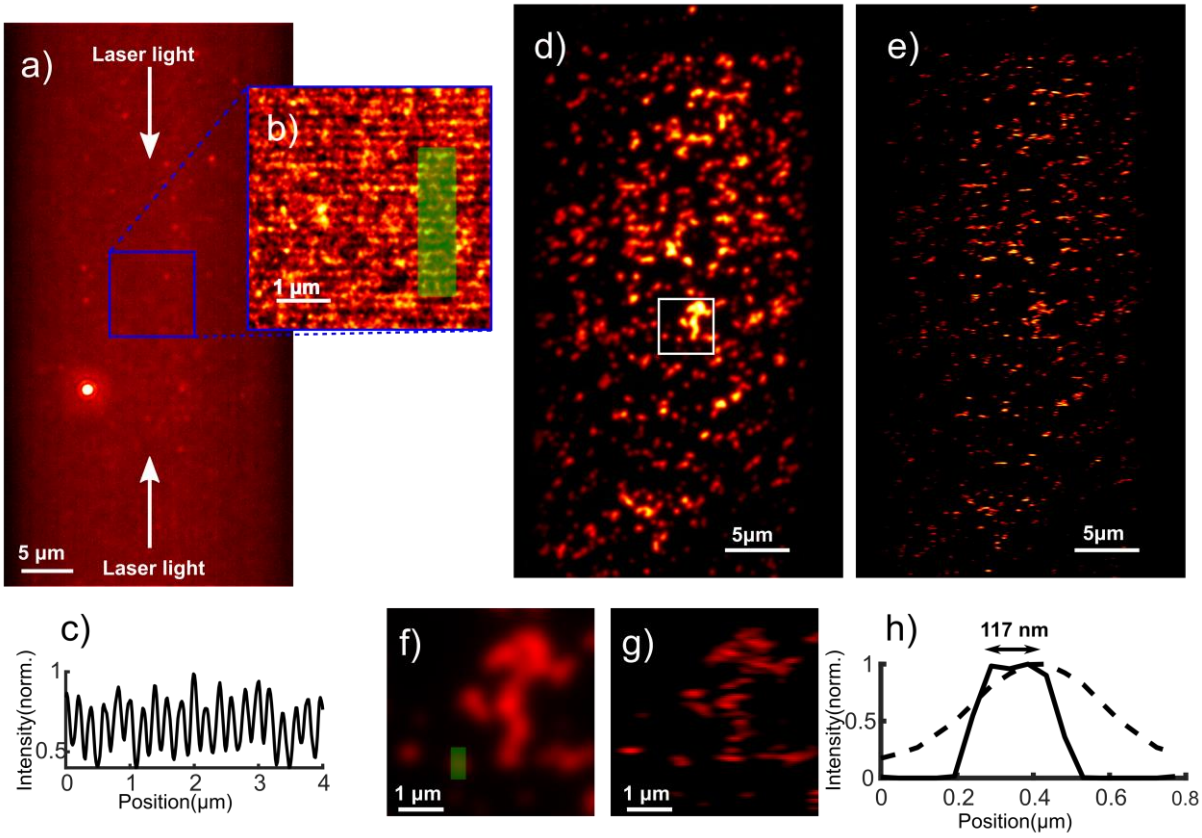

REFERENCES

1 Goodman JW. *Introduction to Fourier Optics*. W. H. Freeman, 2005.

2 Pawley J. *Handbook of Biological Confocal Microscopy*. Springer US, 2010.

3 Eggeling C, Willig KI, Sahl SJ, Hell SW. Lens-based fluorescence nanoscopy. *Quarterly Reviews of Biophysics* 2015, **48**(2)**:** 178-243.

4 Hell SW, Wichmann J. Breaking the diffraction resolution limit by stimulated emission: stimulated-emission-depletion fluorescence microscopy. *Opt Lett* 1994, **19**(11)**:** 780-782.

5 Willig KI, Rizzoli SO, Westphal V, Jahn R, Hell SW. STED microscopy reveals that synaptotagmin remains clustered after synaptic vesicle exocytosis. *Nature* 2006, **440**(7086)**:** 935-939.

6 Rust MJ, Bates M, Zhuang X. Sub-diffraction-limit imaging by stochastic optical reconstruction microscopy (STORM). *Nature Methods* 2006, **3:** 793.

7 Heilemann M, van de Linde S, Schuttpelz M, Kasper R, Seefeldt B, Mukherjee A*, et al.* Subdiffraction-resolution fluorescence imaging with conventional fluorescent probes. *Angewandte Chemie (International ed in English)* 2008, **47**(33)**:** 6172-6176.

8 Betzig E, Patterson GH, Sougrat R, Lindwasser OW, Olenych S, Bonifacino JS*, et al.* Imaging intracellular fluorescent proteins at nanometer resolution. *Science (New York, NY)* 2006, **313**(5793)**:** 1642-1645.

9 Hess ST, Girirajan TPK, Mason MD. Ultra-High Resolution Imaging by Fluorescence Photoactivation Localization Microscopy. *Biophys J* 2006, **91**(11)**:** 4258-4272.

10 Gustafsson MG. Surpassing the lateral resolution limit by a factor of two using structured illumination microscopy. *Journal of microscopy* 2000, **198**(Pt 2)**:** 82-87.

11 Heintzmann R, Cremer CG. *Laterally modulated excitation microscopy: improvement of resolution by using a diffraction grating*, vol. 3568. SPIE, 1999.

12 Sahl SJ, Hell SW, Jakobs S. Fluorescence nanoscopy in cell biology. *Nature Reviews Molecular Cell Biology* 2017, **18:** 685.

13 Kim M, Park C, Rodriguez C, Park Y, Cho Y-H. Superresolution imaging with optical fluctuation using speckle patterns illumination. *Sci Rep-Uk* 2015, **5:** 16525.

14 Guo K, Zhang Z, Jiang S, Liao J, Zhong J, Eldar YC*, et al.* 13-fold resolution gain through turbid layer via translated unknown speckle illumination. *Biomed Opt Express* 2018, **9**(1)**:** 260-275.

15 Yeh L-H, Chowdhury S, Repina NA, Waller L. Speckle-structured illumination for 3D phase and fluorescence computational microscopy. *Biomed Opt Express* 2019, **10**(7)**:** 3635-3653.

16 Mudry E, Belkebir K, Girard J, Savatier J, Le Moal E, Nicoletti C*, et al.* Structured illumination microscopy using unknown speckle patterns. *Nat Photonics* 2012, **6:** 312.

17 Ayuk R, Giovannini H, Jost A, Mudry E, Girard J, Mangeat T*, et al.* Structured illumination fluorescence microscopy with distorted excitations using a filtered blind-SIMalgorithm. *Opt Lett* 2013, **38**(22)**:** 4723-4726.

18 Jost A, Tolstik E, Feldmann P, Wicker K, Sentenac A, Heintzmann R. Optical Sectioning and High Resolution in Single-Slice Structured Illumination Microscopy by Thick Slice Blind-SIM Reconstruction. *Plos One* 2015, **10**(7)**:** e0132174.

19 Cragg GE, So PTC. Lateral resolution enhancement with standing evanescent waves. *Opt Lett* 2000, **25**(1)**:** 46-48.

20 Chung E, Kim D, So PT. Extended resolution wide-field optical imaging: objective-launched standing-wave total internal reflection fluorescence microscopy. *Opt Lett* 2006, **31**(7)**:** 945-947.
21 Kner P, Chhun BB, Griffis ER, Winoto L, Gustafsson MGL. Super-resolution video microscopy of live cells by structured illumination. *Nature Methods* 2009, **6:** 339.
22 Grandin HM, Stadler B, Textor M, Voros J. Waveguide excitation fluorescence microscopy: A new tool for sensing and imaging the biointerface. *Biosensors & Bioelectronics* 2006, **21**(8)**:** 1476-1482.
23 Agnarsson B, Ingthorsson S, Gudjonsson T, Leosson K. Evanescent-wave fluorescence microscopy using symmetric planar waveguides. *Opt Express* 2009, **17**(7)**:** 5075-5082.
24 Agnarsson B, Jonsdottir AB, Arnfinnsdottir NB, Leosson K. On-chip modulation of evanescent illumination and live-cell imaging with polymer waveguides. *Opt Express* 2011, **19**(23)**:** 22929-22935.
25 Diekmann R, Helle OI, Oie CI, McCourt P, Huser TR, Schuttpelz M*, et al.* Chip-based wide field-of-view nanoscopy. *Nat Photonics* 2017, **11**(5)**:** 322-+.
26 Helle ØI, Coucheron DA, Tinguely J-C, Øie CI, Ahluwalia BS. Nanoscopy on-a-chip: super-resolution imaging on the millimeter scale. *Opt Express* 2019, **27**(5)**:** 6700-6710.
27 Tinguely J-C, Helle ØI, Ahluwalia BS. Silicon nitride waveguide platform for fluorescence microscopy of living cells. *Opt Express* 2017, **25**(22)**:** 27678-27690.
28 Fu Y, Ye T, Tang W, Chu T. Efficient adiabatic silicon-on-insulator waveguide taper. *Photon Res* 2014, **2**(3)**:** A41-A44.
29 Harris NC, Ma Y, Mower J, Baehr-Jones T, Englund D, Hochberg M*, et al.* Efficient, compact and low loss thermo-optic phase shifter in silicon. *Opt Express* 2014, **22**(9)**:** 10487-10493.
30 van de Linde S, Löschberger A, Klein T, Heidbreder M, Wolter S, Heilemann M*, et al.* Direct stochastic optical reconstruction microscopy with standard fluorescent probes. *Nature protocols* 2011, **6:** 991.
31 Wei F, Liu Z. Plasmonic Structured Illumination Microscopy. *Nano Letters* 2010, **10**(7)**:** 2531-2536.
32 Wei F, Lu D, Shen H, Wan W, Ponsetto JL, Huang E*, et al.* Wide Field Super-Resolution Surface Imaging through Plasmonic Structured Illumination Microscopy. *Nano Letters* 2014, **14**(8)**:** 4634-4639.
33 Archetti A, Glushkov E, Sieben C, Stroganov A, Radenovic A, Manley S. Waveguide-PAINT offers an open platform for large field-of-view super-resolution imaging. *Nature Communications* 2019, **10**(1)**:** 1267.
34 Schneider J, Zahn J, Maglione M, Sigrist SJ, Marquard J, Chojnacki J*, et al.* Ultrafast, temporally stochastic STED nanoscopy of millisecond dynamics. *Nature Methods* 2015, **12:** 827.
35 Santi PA. Light Sheet Fluorescence Microscopy: A Review. *Journal of Histochemistry & Cytochemistry* 2011, **59**(2)**:** 129-138.
36 Otterstrom NT, Behunin RO, Kittlaus EA, Wang Z, Rakich PT. A silicon Brillouin laser. *Science (New York, NY)* 2018, **360**(6393)**:** 1113-1116.
37 Gaeta AL, Lipson M, Kippenberg TJ. Photonic-chip-based frequency combs. *Nat Photonics* 2019, **13**(3)**:** 158-169.
38 Orth A, Crozier K. Gigapixel fluorescence microscopy with a water immersion microlens array. *Opt Express* 2013, **21**(2)**:** 2361-2368.

39 Prieto F, Sepúlveda B, Calle A, Llobera A, Domínguez C, Abad A*, et al.* An integrated optical interferometric nanodevice based on silicon technology for biosensor applications. *Nanotechnology* 2003, **14**(8)**:** 907.

40 Müller M, Mönkemöller V, Hennig S, Hübner W, Huser T. Open-source image reconstruction of super-resolution structured illumination microscopy data in ImageJ. *Nature Communications* 2016, **7:** 10980.

41 Ovesný M, Křížek P, Borkovec J, Švindrych Z, Hagen GM. ThunderSTORM: a comprehensive ImageJ plug-in for PALM and STORM data analysis and super-resolution imaging. *Bioinformatics* 2014, **30**(16)**:** 2389-2390.

METHODS

Chip Design.

The key parameters in SIM are interference fringe spacing, phase modulation and fringe contrast. For chip-based SIM the dimensions of the active region is also crucial, to ensure that biological specimens are evenly illuminated by the structured illumination. The lateral size of cells are often from 10 µm and upwards.

The waveguide platform has been developed using the high-refractive index material Si3N4. High-index contrast materials enable tight confinement of the light inside the waveguide which entails compact bend radius. This allows for ultra-compact and dense waveguide structures with small footprint benefiting from high intensity in the evanescent field. In the visible range, strong evanescent fields can be achieved by designing waveguides with core thickness between 100-200 nm. For a 150 nm thick core material; single mode condition, adiabatic taper condition and bending losses were previously investigated[27]. It was found that 150 nm thick waveguide core give a strong evanescent field intensity without sacrificing much on the coupling efficiency. For this work single mode condition (**Supplementary figure 11(a)**) is necessary to generate uniform fringe pattern, which can be formed by interfering fundamental mode light guided inside the waveguide. The presence of any residual higher order modes will generate a mode-beat pattern, which is undesirable. Thus, shallow rib waveguides were preferred over strip waveguides. For a shallow rib, fundamental mode guiding can be achieved using waveguide widths (1-1.5 µm wide) (**Supplementary figure 11(b)**) within the reach of fabrication using standard photo-lithography techniques. Waveguides with 4 nm rib height (total height of 150 nm) and around 1-1.5 µm width was adiabatic tapered out to 25 µm or 50 µm with a tapering length of 2 mm or 4 mm, respectively. A significantly low bending loss for a shallow rib waveguides was achieved for a bend radius of 2 mm and more. The optimization of the designed parameters can be found in previous literature[27].

Chip fabrication.

The production of waveguide chips was performed at the Insitute of Microelectronics Barcelona (IMB-CNM, Spain). First, an oxide layer of ca. 2 µm was thermally grown on a silicon slab, followed by low-pressure chemical vapor deposition (LPCVD) of 150 nm Si_3N_4 at 800°. Conventional photo-lithography imprinted the waveguide geometries on a layer of photo-resist. 4 nm rib waveguides were realized using reactive-ion-etching (RIE). In order to prevent cross-talk of light into adjacent waveguide structures, an absorption layer consisting of 200 nm SiO_2 (deposited by plasma-enhanced chemical vapor deposition (PECVD)) followed by 100 nm poly-crystalline silicon (deposited by PECVD at 300°) was designed as a negative image of the first mask with 10 µm added to the waveguide width. RIE was used to etch until 100 nm of

SiO_2 remained, with wet etching (using hydrofluoric acid) removing the remaining material from the waveguide surface. Finally, a 1.5 µm SiO_2 layer (deposited by PECVD) built the cladding layer. The chip fabrication workflow is shown in **supplementary figure 12**. Imaging areas were patterned by a 3rd photo-lithography step. The window openings were realized using RIE until 100 nm SiO_2 was remaining, followed by wet etching to completely remove the oxide layer while preserving the Si_3N_4. Further details of the fabrication optimization and process can be found elsewhere[39].

Experimental setup.

A microscope modified from an Olympus modular microscope (BXFM) was mounted on a XY motorized translation stage. The microscope was fitted with a Hamamatsu Orca flash sCMOS camera. cSIM images were acquired using either Olympus x60/1.3SiO or Olympus x60/1.2W objective lenses. The waveguide chip was mounted on a micrometer xyz-stage using a vacuum chuck to hold the chip. Light was coupled on to the chip using a nine-fiber array adapter. The fibre array adapters are commercially available with fixed spacing (e.g. 127 µm). The waveguides were separated by the same space (127 µmm) as the fibre array, allowing for multiple waveguides to have light coupled at the same time (supplementary figure 7b). For off-chip cSIM (Fig.2a,d), an additional 50:50 fused fibre-split (OZ optics) was used to split the light. Thermo-optical phase stepping was achieved using a 6V voltage supply coupled to the resistive on-chip electro-optical heating elements. A schematic of the setup is shown in **supplementary figure 10**. The image data was analyzed using Fiji open source image processing software and FairSIM[40], an open source SIM reconstruction plugin. cSIM data from the 180° interference waveguides was analyzed with custom software.

Near-field mapping using dSTORM.

dSTORM near field mapping was performed by staining the waveguide surface with a layer of fluorescent molecules. A 1/1000 solution of CellMask deep red (Thermofisher, C10046) in phosphate buffered saline (PBS) was incubated for 20 minutes on the waveguide surface at room temperature. The solution was aspirated and a PDMS micro-chamber positioned on top of the chip was filled with dSTORM switching buffer consisting of an enzymatic oxygen scavenging system and 100 mM β-Mercaptoethylamine (MEA). The surface was excited with the 660 nm laser with sufficiently high power to achieve photo-switching. A stack of 100000 images was acquired at 30 ms exposure time and reconstructed using the Fiji plugin ThunderStorm[41].

Sample preparation.

The chip surface was coated with 0.5% Poly-l-lysine (PLL) solution, aspirated and dried with compressed Nitrogen. Depending on the desired distribution of fluorescent beads the chip would be plasma treated at a high setting for 30s, ensuring hydrophilic surface properties. A 0.5 µl drop of 100nm diameter fluorescent bead stock ((Tetraspeck, Thermofisher T7279) was put at the cSIM image region and allowed to dry completely. The chamber was filled with dH2O and the chip brought to the microscope for imaging.

REFERENCES FOR METHODS

21 Tinguely J-C, Helle ØI, Ahluwalia BS. Silicon nitride waveguide platform for fluorescence microscopy of living cells. *Opt Express* 2017, **25**(22)**:** 27678-27690.

32 Prieto F, Sepúlveda B, Calle A, Llobera A, Domínguez C, Abad A*, et al.* An integrated optical interferometric nanodevice based on silicon technology for biosensor applications. *Nanotechnology* 2003, **14**(8)**:** 907.

33 Müller M, Mönkemöller V, Hennig S, Hübner W, Huser T. Open-source image reconstruction of super-resolution structured illumination microscopy data in ImageJ. *Nature Communications* 2016, **7:** 10980.

34 Ovesný M, Křížek P, Borkovec J, Švindrych Z, Hagen GM. ThunderSTORM: a comprehensive ImageJ plug-in for PALM and STORM data analysis and super-resolution imaging. *Bioinformatics* 2014, **30**(16)**:** 2389-2390.

Structured illumination microscopy using a photonic chip

Supplementary Information

Øystein I. Helle Firehun T. Dullo Jean-Claude Tinguely
Marcel Lahrberg Balpreet S. Ahluwalia

March 2019

Supplementary note 1: Simulation of chip-based interference patterns

The cSIM interference patterns were simulated using finite element method in Comsol Multiphysics. Figure 1(a) shows two waveguides crossing at an angle of 50°. The red arrows indicate the directions of the straight waveguides along which the light propagates. Since the presented model is limited to a two-dimensional representation of the actual waveguide, the effective refractive indices along the third dimension have been calculated approximating those regions as planar waveguides [1]. Given the fundamental transversal electric (TE) mode being exited in each waveguide, the resulting intensity distribution shows the intended sinusoidal structure as well as a Gaussian envelope due to the shape of the waveguide modes. The mode index in the simulated Si_3N_4 structures is found to be $n = 1.7552$ at a vacuum wavelength of $\lambda = 660\,\mathrm{nm}$. In the presented model only the fundamental modes of the waveguides are excited. As it is indicated in Fig. 1(a), in order to estimate the periodicity of the intensity pattern, a sinusoidal function of the form $I(x) = \exp\left(-\left(\frac{x}{a}\right)^2\right)\sin^2(bx)$ has been fitted; the pattern spacing is found to be 445 nm.

Figure 1(b) shows respective simulation results for counter-propagating waveguides, i.e. interfering at an angle of 180°. As for the case of an interference angle of 50°, the intensity distribution was fitted as $I(x) = \sin^2(ax)$ and a period of 188 nm is found.

Although the pattern spacing can be calculated from the effective mode index without running a full numerical simulation of the structure, here the simulation results are used to illustrate the expected intensity distribution over the whole waveguide geometry.

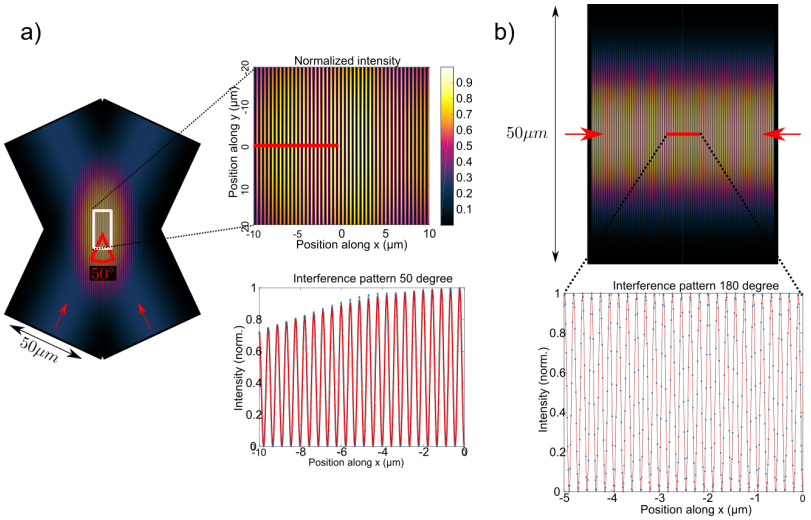

Figure 1: Numerical simulations of the proposed waveguide geometries to generate the illumination patterns for cSIM. The configurations of two waveguides crossing at an angle of 50° (a) generates a pattern with a periodicity of 445 nm. The couterpropagating waveguides (b) create a pattern with a period of 188 nm.

Supplementary note 2: Resolution of cSIM

The microscope objective is inherently a low pass filter, stopping frequency content above a certain value k_0, often refered to as the diffraction limited. Structure illumination microscopy relies on a sinusoidal excitation light to excite fluorescence in the sample. For a sample having frequency $\mathbf{k}$, the multiplication of structured illumination and sample yields a moirè pattern with observable frequencies $|\mathbf{k} - \mathbf{k_1}|$, if these are within the passband of the OTF (k_0) [2]. So as long as $\mathbf{k}$ lies within a circle of radius k_0 centered around $\mathbf{k_1}$, it will be indirectly observed in the moirè fringes. By going through the SIM reconstruction using phase stepping the achievable resolution of the reconstructed image is then $k_0 + k_1$. In this sense, it is desirable to have a large k_1, but since k_1 is formed using lenses, the method is also limited by diffraction, with the highest possible value of k_1 being k_0. Finally this would yield a maximum resolution enhancement of $2k_0$. By generating the structured illumination using waveguides the formation of k_1 is no longer depending on lenses, and is thus not diffraction limited but instead relies on the effective refractive index of the waveguide materials, as outlined below.

The resolution of cSIM is governed by the fringe-spacing of the standing wave interference pattern in addition to the N.A. of the collection optics. By interfering waveguides with changing angles θ the fringe spacing f_s can be changed as

$$f_s = \frac{\lambda_{ex}}{2n_{eff}\sin\theta/2}, \tag{1}$$

where n_{eff} is the effective refractive index of the guided mode. Generating the SIM pattern with a planar waveguide thus contributes n_{eff} in to the achievable resolution Δ_{xy} of the method, so the equation describing the theoretical best resolution for cSIM takes the form of

$$\Delta_{xy} = \frac{\lambda_{ex}}{2(N.A. + n_{eff}\sin\theta/2)}, \tag{2}$$

where N.A. is the numerical aperture of the imaging objective lens. Since n_{eff} is larger than N.A. the resolution of the method can exceed that of conventional SIM, which would have $4N.A.$ in the denominator.

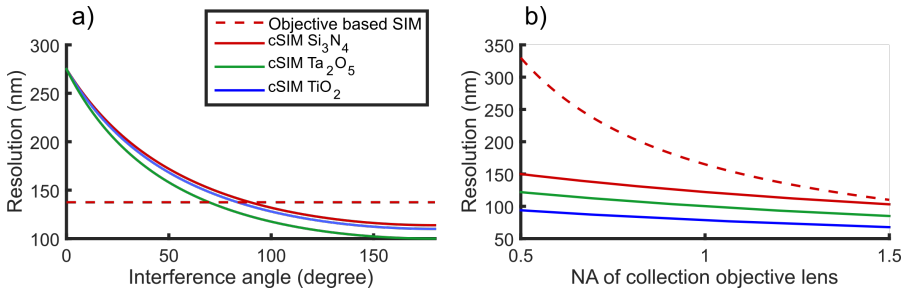

Figure 2: Graphical interpretation of eq. 2 for three different materials is shown. a) The angle of interference is dominating the achievable resoltuion for cSIM, which for interference angles between 70-100° surpass the resolution of conventional objective based SIM, using N.A.=1.2. b) The maximum achievable resolution for different N.A. objective lens, and thus different field of view size is shown for both cSIM (using 180° interference) and objective based SIM. The potential for cSIM to yield high resolution over large fields of view can be harnessed by acquiring several images with different interference angles as shown in Fig.4.

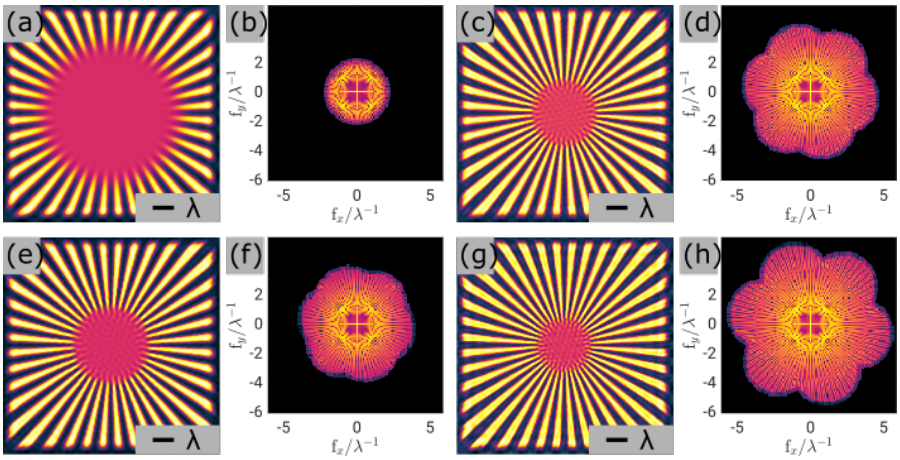

Figure 3: Simulation of SIM using the Siemens star sample. Spatial and freqency images are shown sequentially. a,b) Diffraction limited image. c,d) Conventional SIM image, e,f) cSIM using 60 degree interference angle. g,h cSIM using 180 degree intefernce angle)

Supplementary note 3: Simulation of chip-based SIM

The effect of structured illumination using planar waveguides is presented in Figs. 3 and 4 for two different imaging objective lenses using the Siemens star sample.

In Fig. 3, imaging using an objective lens with N.A. = 1.2 is simulated. Figure 3(a) shows the spatial result using plain illumination, and Fig. 3(b) shows the logarithmic values of the Fourier spectrum. It is visible in the figure that the highest frequency is limited to $2\text{N.A.}/\lambda = 2.4\lambda^{-1}$. Fig. 3 (c) and (d) show the effect of SIM imaging using the conventional objective based approch, having a spatial frequency of the SIM pattern at the OTF cutoff frequency $2\text{N.A.}/\lambda$, yielding a 2x resolution enhancement. For a sample that is illuminated with a sinusoidal stripe pattern using planar waveguides with an effective refractive index of $n_{\text{eff}} = 1.7$ at an angle between the waveguides of 60° the expected SIM result is shown in Fig. 3(e)-3(f). Increasing the interference angle to 180° increases the modulation frequency of the illumination pattern and thus the expected resolution improvement as shown in Figs. 3(g)-3(h).

In a similar fashion cSIM imaging is simulated in Fig. 4 for an objective lens with N.A. = 0.6. Figures 4(a)-4(b) show the result from using plain illumination. It shows a clear reduction in resolution as compared to the result using an imaging objective with a N.A. = 1.2 as in Figs. 3(a)-3(b).

Using an illumination pattern generated by waveguides with an interfering angle of 30° will improve the resolution as presented in Figs. 4(c)-4(d). For cSIM using patterns generated with interference angles of 120° and 180° it is possible to obtain sample information of high spatial frequency as illustrated in Figs.

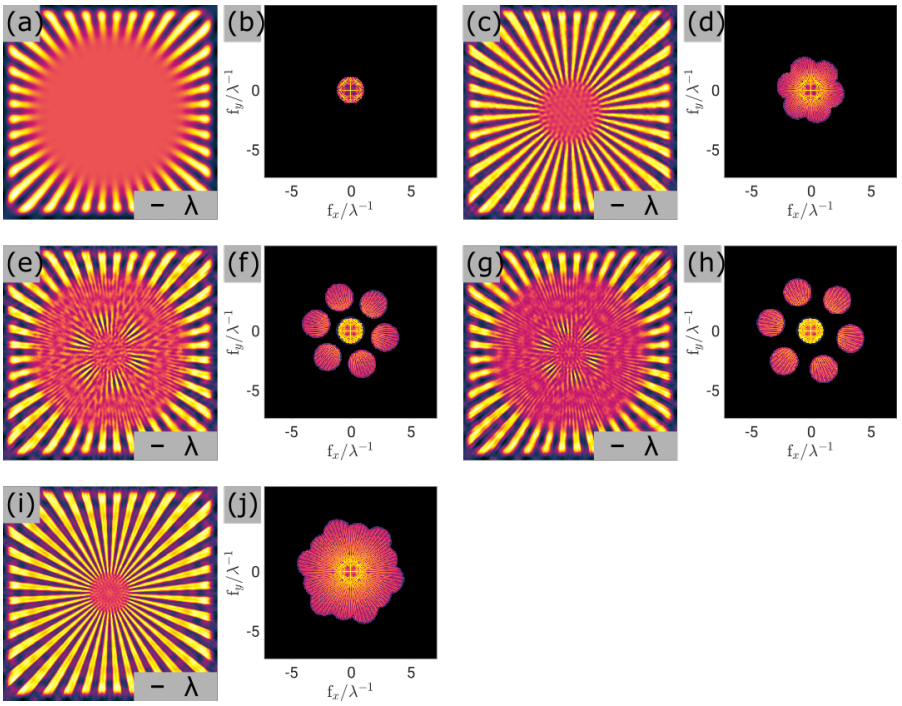

Figure 4: The resolution improvement using chip based SIM is simulated for an imaging objective with $N.A. = 0.6$. (a) and (b) show the result of conventional deconvolution imaging at the indicated wavelength λ and the representation in Fourier space respectively. (c) and (d) show the SIM results for patterns generated at an waveguide interference angle of 60°. (e)-(f) and (g)-(h) show the SIM result using interference patterns generated at angles of 120° and 180° respectively. In (i) and (j) the SIM reconstructions using all interference angles (60°; 120°; 180°) are shown.

4(e)-4(f) and Fig. 4(g)-4(h) respectively. Since the Fourier space is not filled evenly in this approach, a combined use of illumination patterns generated at interference angles of 60°, 120° and 180° as shown in Figs. 4(i)-4(j) will improve the resolution without the loss of frequency bands. Thus, cSIM supports the use of low magnification/N.A. objective lens to enable super-resolution imaging over large field of view (FOV), while the maximum attainable resolution will be supported by the illumination provided by the waveguide as demonstrated in Figs. 4(i)-4(j). In conventional SIM, the illumination and the collection light paths are coupled, thus a use of low. N.A. objective lens to image large FOV will significantly reduce the supported optical resolution.

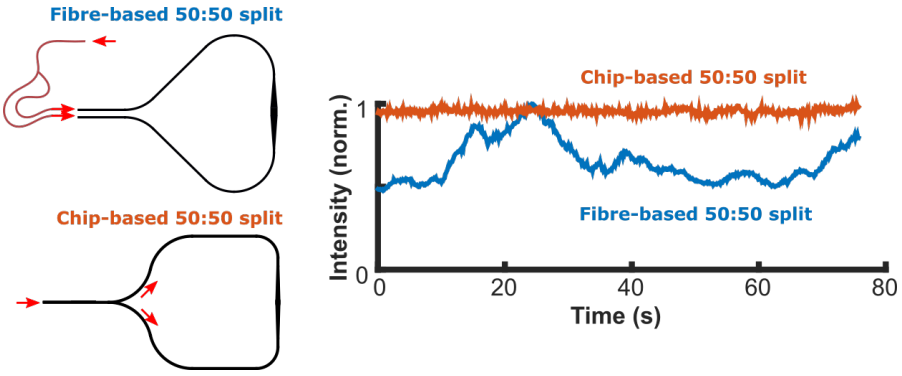

Figure 5: The phase stability of the standing wave SIM interference pattern is shown indirectly by tracking the fluorescence from a bead over time. By splitting the light on the optical table using a 50:50 fibre split the phase of the standing wave is drifting in time, seen with the blue curve. When splitting the light on-chip, the phase is obeserved to be stable over time (red curve).

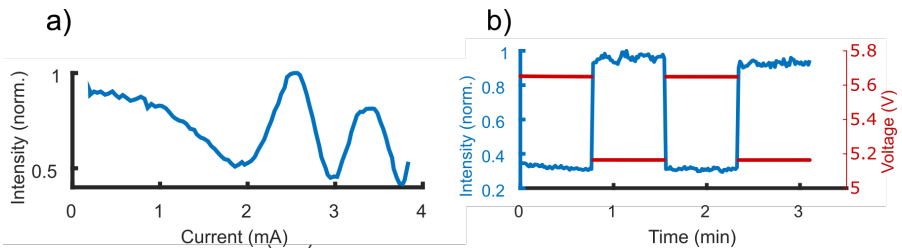

Figure 6: a) By applying current to the thermo-optical element the phase of the SIM interference pattern was changed. A fluorescent bead was tracked while changing the current, thus shifting the SIM pattern phase. b) By selecting the voltages corresponding to a π change in the SIM pattern, the phase was stepped between 0 and π over 3 minutes to demonstrate the reproducibility of the phase stepping method.

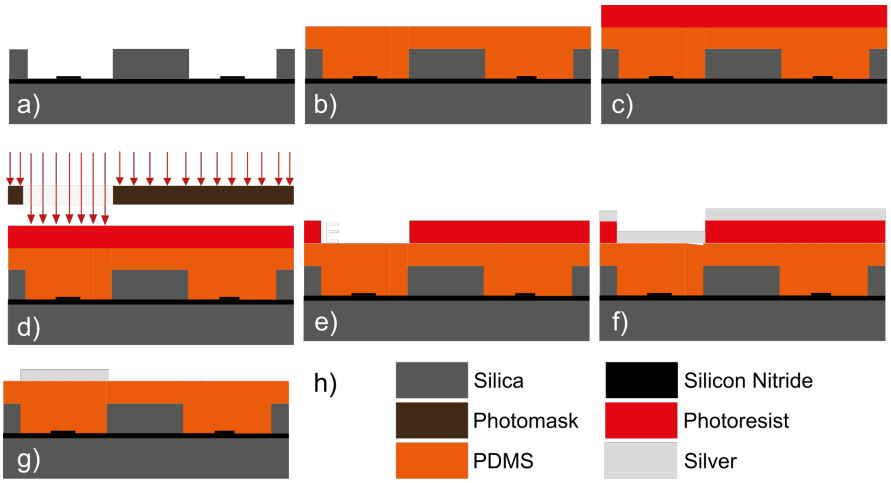

Figure 7: Fabrication of thermo-optic heating element. (a) Both arms of the cSIM structure incorporates opening in the cladding. (b) A cladding layer made from either PDMS or Su-8 covers the entire chip, followed by a photo-resist (c). (d) One of the openings is exposed and the photo-resist was removed. (e) A layer of Ag is sputtered on the entire chip, before the photo-resist is removed leaving only silver on one of the arms.

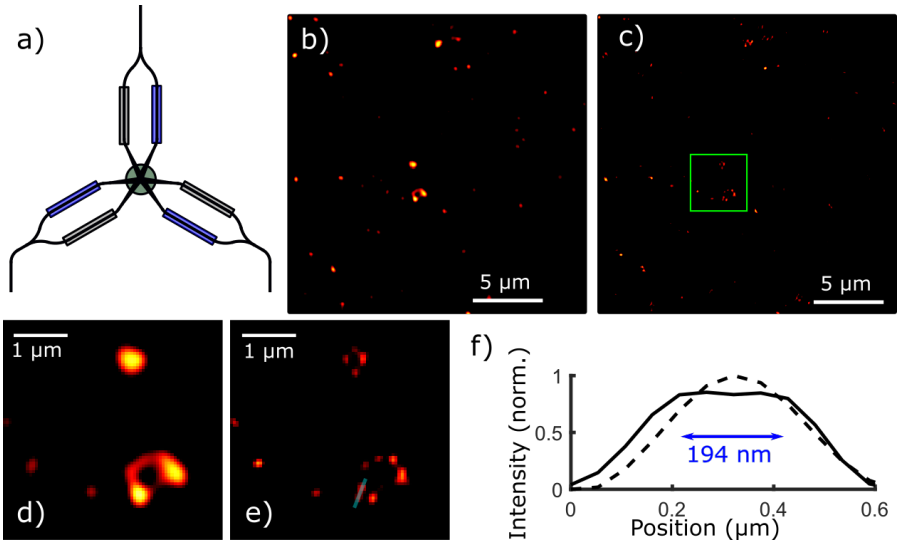

Figure 8: a) cSIM using thermo-optics phase modulation with 50° interference angle. b) Show the diffraction limited image of 100nm fluorescence beads under plain 660nm illumination yielding a diffraction limited image. c) Using the structure shown in a), the cSIM reconstruction shows a clear resolution enhancement. d) and e) shows the zoom indicated with a green box in c). f) Show a line-profile over an intensity distribution comparing the diffraction limited (dotted line) and cSIM reconstruction (solid line). The cSIM image shows two beads separated by 194nm, which is not resolved in the diffraction limited image.

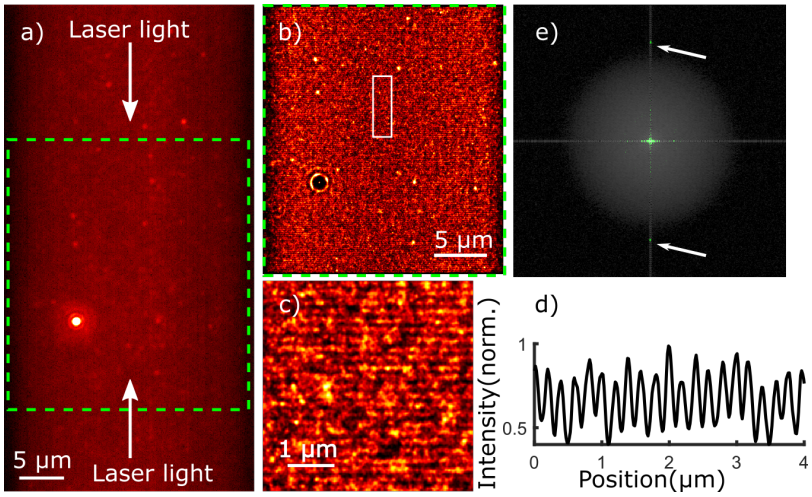

Figure 9: The waveguide surface was stained with a fluorescent dye. a) The standing wave interference pattern is not visible under diffraction limited imaging. b) By using *d*STORM imaging the sub-diffraction limited standing wave pattern was visualized, as better seen in the zoomed image (c). d) A line-profile shows the modulation with a fringe spacing of around 195 nm. d) The power-spectrum of the diffraction limited image (a) and the *d*STORM reconstruction (b) is overlaid, with the green peaks showing the frequency peak of the standing wave at its position outside the span of the OTF.

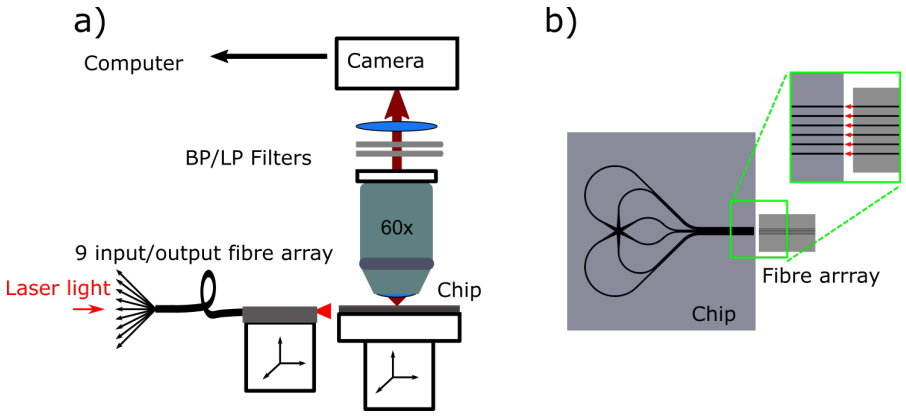

Figure 10: Experimental setup. a) An upright microscope detects the emitted fluorescence. The waveguide chip is held by a vacuum chuck while light is coupled on to the chip via a nine-fibre array adapter. Both sample and coupling stages have xyz movement. b) The fibre array adapter holds 9 optical fibers with equidistant spacing (127 μm), which corresponds to the waveguide spacing on the chip. Each of the 9 optical fibers can be individually activated, according to the chip designs being used.

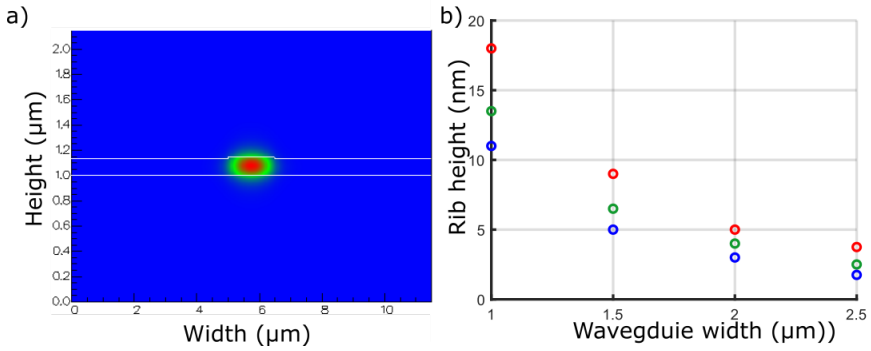

Figure 11: a) Simulation showing the fundamental transverse electric (TE) mode guided in waveguide core, with parts of the light outside the top surface as an evanescent field. b) Simulated threshold rib height values for single mode operation for different waveguide widths and wavelengths (660 nm, 561 nm and 488 nm are shown in the appropriate colors.)

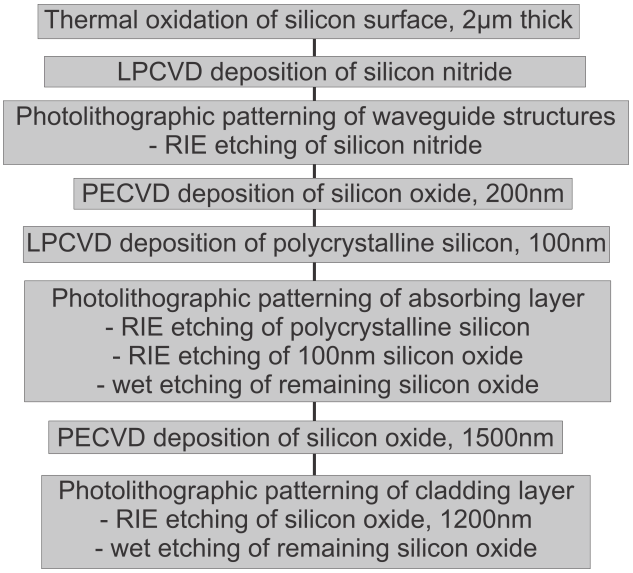

Figure 12: Flow-chart showing the fabrication steps performed in the production of cSIM waveguide chips

References

[1] K. Okamoto, *Fundamentals of Optical Waveguides*, pp. 16–19. 2006.

[2] M. G. L. Gustafsson, "Nonlinear structured-illumination microscopy: Wide-field fluorescence imaging with theoretically unlimited resolution," *Proceedings of the National Academy of Sciences of the United States of America*, vol. 102, no. 37, pp. 13081–13086, 2005.

6

Conclusions

In this thesis, chip-based fluorescence imaging was explored. Planar waveguide chips were used to guide the light towards the specimen, which was mounted on the chip surface. Fluorescence excitation of the samples was achieved using the evanescent field, which is exponentially decaying up to around 100 nm (for 660 nm wavelength). Since the illuminated area is determined by the waveguide layout, and the illumination is independent of the imaging objective lens, large FOV TIRF imaging could be explored. In chapter 4, SMLM imaging was investigated using dSTORM, where the FOV of the super-resolved image was around 100 times larger than the conventional approach (papers 3 and 4). Here, the gain in FOV was followed by a reduction of the resolution enhancement compared to conventional methods due to the N.A. of the objective lens. Furthermore, in chapter 5 and paper 5, CSIM imaging was demonstrated. Using PIC chips for SIM, the resolution enhancement can overcome that of conventional SIM due to high spatial frequency fringes formed using high index materials and counter-propagating waveguides.

By replacing the sample glass/coverglass with a PIC a basic microscope can be retrofitted into an optical nanoscope. In this work, we used an upright microscope, but in future implementations, inverted setups will be explored. By going inverted, the aim would be to create transparent waveguide chips to allow a larger range of N.A. objectives to be used. Another possible outcome is the reduced optical path that the fluorescence signal must travel before entering the collection objective lens. In the current upright setup, we used a sample well filled with aqueous imaging buffers. The emitted fluorescence happens

at the chip surface, and for upright collection, the photons must propagate first through the sample itself (e.g a cell) and then through the buffer before reaching the coverglass and objective lens. Most objectives are corrected for the coverglass, but not for the increased depth of the sample well. We solved the last issue by using objectives with a correction collar to correct for aberrations caused by the image buffer. Another thing to consider, particularly for SMLM is whether or not there will be multiple scattering due to the refractive index mismatch of sample and buffers, which would favor the inverted setup. We did have problems repeating experiments on different cell lines than LSEC, but this could very well be due to the perfect match between LSEC and TIRF. These cells have most of their structures located within the evanescent field, and thus produce a nice image.

In this work, we have mostly focused on proof-of-concept results for the on-chip versions of SMLM and SIM. By the release of these results, we hope to open a new direction of advanced light shaping for optical nanoscopy techniques. By harnessing interference and multimode waveguides new illumination routes for improving other already existing techniques like STED or light-sheet microscopy can be explored, and with the added possibility of finding all together new methods. PIC chips can potentially be mass-produced since large scale CMOS foundries already possess the necessary fabrication facilities needed. From a commercialization point-of-view, large scale production of chips could potentially lead to disposable photonic chips which can be easily retrofitted on to standard bench-top microscopes. Furthermore, by the advent of other on-chip technologies such as optical trapping [71], on-chip lasers [72] and frequency combs [73], combined with micro-fluidics, fully functioning, multi-modality lab-on-chip can be developed.

Bibliography

[1] D. E. Wolf. The optics of microscope image formation. *Methods Cell Biol*, 114:11–42, 2013.

[2] Rayleigh. Xxxi. investigations in optics, with special reference to the spectroscope. *The London, Edinburgh, and Dublin Philosophical Magazine and Journal of Science*, 8(49):261–274, 1879.

[3] E. Abbe. Beiträge zur theorie des mikroskops und der mikroskopischen wahrnehmung. *Archiv für mikroskopische Anatomie*, 9(1):413–418, 1873.

[4] E. Hecht. *Optics*. Addison-Wesley, 2002.

[5] Stefan W. Hell and Jan Wichmann. Breaking the diffraction resolution limit by stimulated emission: stimulated-emission-depletion fluorescence microscopy. *Optics Letters*, 19(11):780–782, 1994.

[6] E. Betzig. Proposed method for molecular optical imaging. *Optics Letters*, 20(3):237–239, 1995.

[7] W. E. Moerner and L. Kador. Optical detection and spectroscopy of single molecules in a solid. *Physical Review Letters*, 62(21):2535–2538, 1989.

[8] Thomas A. Klar, Stefan Jakobs, Marcus Dyba, Alexander Egner, and Stefan W. Hell. Fluorescence microscopy with diffraction resolution barrier broken by stimulated emission. *Proceedings of the National Academy of Sciences*, 97(15):8206–8210, 2000.

[9] R. M. Dickson, A. B. Cubitt, R. Y. Tsien, and W. E. Moerner. On/off blinking and switching behaviour of single molecules of green fluorescent protein. *Nature*, 388(6640):355–8, 1997.

[10] E. Betzig, G. H. Patterson, R. Sougrat, O. W. Lindwasser, S. Olenych, J. S. Bonifacino, M. W. Davidson, J. Lippincott-Schwartz, and H. F. Hess. Imaging intracellular fluorescent proteins at nanometer resolution. *Science*,

313(5793):1642–5, 2006.

[11] Jale Schneider, Jasmin Zahn, Marta Maglione, Stephan J. Sigrist, Jonas Marquard, Jakub Chojnacki, Hans-Georg Kräusslich, Steffen J. Sahl, Johann Engelhardt, and Stefan W. Hell. Ultrafast, temporally stochastic sted nanoscopy of millisecond dynamics. *Nature Methods*, 12:827, 2015.

[12] Gael Moneron, Rebecca Medda, Birka Hein, Arnold Giske, Volker Westphal, and Stefan W. Hell. Fast sted microscopy with continuous wave fiber lasers. *Optics Express*, 18(2):1302–1309, 2010.

[13] Andriy Chmyrov, Jan Keller, Tim Grotjohann, Michael Ratz, Elisa d'Este, Stefan Jakobs, Christian Eggeling, and Stefan W. Hell. Nanoscopy with more than 100,000 doughnuts. *Nature Methods*, 10:737, 2013.

[14] W. P. Ambrose and W. E. Moerner. Fluorescence spectroscopy and spectral diffusion of single impurity molecules in a crystal. *Nature*, 349(6306):225–227, 1991.

[15] Michael J. Rust, Mark Bates, and Xiaowei Zhuang. Sub-diffraction-limit imaging by stochastic optical reconstruction microscopy (storm). *Nature Methods*, 3:793, 2006.

[16] S. T. Hess, T. P. Girirajan, and M. D. Mason. Ultra-high resolution imaging by fluorescence photoactivation localization microscopy. *Biophys J*, 91(11):4258–72, 2006.

[17] Jonas Fölling, Mariano Bossi, Hannes Bock, Rebecca Medda, Christian A. Wurm, Birka Hein, Stefan Jakobs, Christian Eggeling, and Stefan W. Hell. Fluorescence nanoscopy by ground-state depletion and single-molecule return. *Nature Methods*, 5:943, 2008.

[18] S. W. Hell and M. Kroug. Ground-state-depletion fluorscence microscopy: A concept for breaking the diffraction resolution limit. *Applied Physics B*, 60(5):495–497, 1995.

[19] M. Heilemann, S. van de Linde, M. Schuttpelz, R. Kasper, B. Seefeldt, A. Mukherjee, P. Tinnefeld, and M. Sauer. Subdiffraction-resolution fluorescence imaging with conventional fluorescent probes. *Angew Chem Int Ed Engl*, 47(33):6172–6, 2008.

[20] Sebastian van de Linde, Anna Löschberger, Teresa Klein, Meike Heidbreder, Steve Wolter, Mike Heilemann, and Markus Sauer. Direct stochastic optical reconstruction microscopy with standard fluorescent probes.

Nature Protocols, 6:991, 2011.

[21] S. van de Linde, R. Kasper, M. Heilemann, and M. Sauer. Photoswitching microscopy with standard fluorophores. *Applied Physics B*, 93(4):725, 2008.

[22] David Baddeley, Isuru D. Jayasinghe, Christoph Cremer, Mark B. Cannell, and Christian Soeller. Light-induced dark states of organic fluochromes enable 30 nm resolution imaging in standard media. *Biophysical Journal*, 96(2):L22–L24, 2009.

[23] Mike Heilemann, Emmanuel Margeat, Robert Kasper, Markus Sauer, and Philip Tinnefeld. Carbocyanine dyes as efficient reversible single-molecule optical switch. *Journal of the American Chemical Society*, 127(11):3801–3806, 2005.

[24] Jianquan Xu, Hongqiang Ma, and Yang Liu. Stochastic optical reconstruction microscopy (storm). *Current protocols in cytometry*, 81:12.46.1–12.46.27, 2017.

[25] R. E. Thompson, D. R. Larson, and W. W. Webb. Precise nanometer localization analysis for individual fluorescent probes. *Biophys J*, 82(5):2775–83, 2002.

[26] Sebastian van de Linde. Single-molecule localization microscopy analysis with imagej. *Journal of Physics D: Applied Physics*, 52(20):203002, 2019.

[27] Martin Ovesný, Pavel Křížek, Josef Borkovec, Zdeněk Švindrych, and Guy M. Hagen. Thunderstorm: a comprehensive imagej plug-in for palm and storm data analysis and super-resolution imaging. *Bioinformatics*, 30(16):2389–2390, 2014.

[28] Graham T. Dempsey, Joshua C. Vaughan, Kok Hao Chen, Mark Bates, and Xiaowei Zhuang. Evaluation of fluorophores for optimal performance in localization-based super-resolution imaging. *Nature methods*, 8(12):1027–1036, 2011.

[29] Sang-Hee Shim, Chenglong Xia, Guisheng Zhong, Hazen P. Babcock, Joshua C. Vaughan, Bo Huang, Xun Wang, Cheng Xu, Guo-Qiang Bi, and Xiaowei Zhuang. Super-resolution fluorescence imaging of organelles in live cells with photoswitchable membrane probes. *Proceedings of the National Academy of Sciences*, 109(35):13978–13983, 2012.

[30] Wesley R. Legant, Lin Shao, Jonathan B. Grimm, Timothy A. Brown,

Daniel E. Milkie, Brian B. Avants, Luke D. Lavis, and Eric Betzig. High-density three-dimensional localization microscopy across large volumes. *Nature Methods*, 13:359, 2016.

[31] Joerg Schnitzbauer, Maximilian T. Strauss, Thomas Schlichthaerle, Florian Schueder, and Ralf Jungmann. Super-resolution microscopy with dna-paint. *Nature Protocols*, 12:1198, 2017.

[32] Makio Tokunaga, Naoko Imamoto, and Kumiko Sakata-Sogawa. Highly inclined thin illumination enables clear single-molecule imaging in cells. *Nature Methods*, 5:159, 2008.

[33] Lei Zhu, Wei Zhang, Daniel Elnatan, and Bo Huang. Faster storm using compressed sensing. *Nature methods*, 9(7):721–723, 2012.

[34] T. Dertinger, R. Colyer, G. Iyer, S. Weiss, and J. Enderlein. Fast, background-free, 3d super-resolution optical fluctuation imaging (sofi). *Proceedings of the National Academy of Sciences*, 106(52):22287–22292, 2009.

[35] Idir Yahiatene, Simon Hennig, Marcel Müller, and Thomas Huser. Entropy-based super-resolution imaging (esi): From disorder to fine detail. *ACS Photonics*, 2(8):1049–1056, 2015.

[36] Krishna Agarwal and Radek Macháň. Multiple signal classification algorithm for super-resolution fluorescence microscopy. *Nature Communications*, 7:13752, 2016.

[37] MinKwan Kim, ChungHyun Park, Christophe Rodriguez, YongKeun Park, and Yong-Hoon Cho. Superresolution imaging with optical fluctuation using speckle patterns illumination. *Scientific Reports*, 5:16525, 2015.

[38] M. G. Gustafsson. Surpassing the lateral resolution limit by a factor of two using structured illumination microscopy. *J Microsc*, 198(Pt 2):82–7, 2000.

[39] P. Kner, B. B. Chhun, E. R. Griffis, L. Winoto, and M. G. Gustafsson. Super-resolution video microscopy of live cells by structured illumination. *Nat Methods*, 6(5):339–42, 2009.

[40] Feifei Wei and Zhaowei Liu. Plasmonic structured illumination microscopy. *Nano Letters*, 10(7):2531–2536, 2010.

[41] Anna Bezryadina, Junxiang Zhao, Yang Xia, Yeon Ui Lee, Xiang Zhang, and Zhaowei Liu. Localized plasmonic structured illumination microscopy

with gaps in spatial frequencies. *Optics Letters*, 44(11):2915–2918, 2019.

[42] Mats G. L. Gustafsson. Nonlinear structured-illumination microscopy: Wide-field fluorescence imaging with theoretically unlimited resolution. *Proceedings of the National Academy of Sciences of the United States of America*, 102(37):13081–13086, 2005.

[43] R. Fiolka, M. Beck, and A. Stemmer. Structured illumination in total internal reflection fluorescence microscopy using a spatial light modulator. *Opt Lett*, 33(14):1629–31, 2008.

[44] Dong Li, Lin Shao, Bi-Chang Chen, Xi Zhang, Mingshu Zhang, Brian Moses, Daniel E. Milkie, Jordan R. Beach, John A. Hammer, Mithun Pasham, Tomas Kirchhausen, Michelle A. Baird, Michael W. Davidson, Pingyong Xu, and Eric Betzig. Extended-resolution structured illumination imaging of endocytic and cytoskeletal dynamics. *Science*, 349(6251):aab3500, 2015.

[45] D.L. Lee. *Electromagnetic principles of integrated optics*. Wiley, 1986.

[46] R.G. Hunsperger. *Integrated Optics: Theory and Technology*. Springer New York, 2009.

[47] B.E.A. Saleh and M.C. Teich. *Fundamentals of Photonics*. Wiley, 2007.

[48] K. N. Fish. Total internal reflection fluorescence (tirf) microscopy. *Curr Protoc Cytom*, Chapter 12:Unit12.18, 2009.

[49] E. H. Hellen and D. Axelrod. Kinetics of epidermal growth factor/receptor binding on cells measured by total internal reflection/fluorescence recovery after photobleaching. *J Fluoresc*, 1(2):113–28, 1991.

[50] R. M. Drenan, R. Nashmi, P. Imoukhuede, H. Just, S. McKinney, and H. A. Lester. Subcellular trafficking, pentameric assembly, and subunit stoichiometry of neuronal nicotinic acetylcholine receptors containing fluorescently labeled alpha6 and beta3 subunits. *Mol Pharmacol*, 73(1):27–41, 2008.

[51] D. Zenisek, J. A. Steyer, M. E. Feldman, and W. Almers. A membrane marker leaves synaptic vesicles in milliseconds after exocytosis in retinal bipolar cells. *Neuron*, 35(6):1085–97, 2002.

[52] E. Pryazhnikov and L. Khiroug. Sub-micromolar increase in [ca(2+)](i) triggers delayed exocytosis of atp in cultured astrocytes. *Glia*, 56(1):38–49, 2008.

[53] D. Axelrod. Cell-substrate contacts illuminated by total internal reflection fluorescence. *J Cell Biol*, 89(1):141–5, 1981.

[54] H. M. Grandin, B. Stadler, M. Textor, and J. Voros. Waveguide excitation fluorescence microscopy: A new tool for sensing and imaging the biointerface. *Biosensors & Bioelectronics*, 21(8):1476–1482, 2006.

[55] B. Agnarsson, S. Ingthorsson, T. Gudjonsson, and K. Leosson. Evanescent-wave fluorescence microscopy using symmetric planar waveguides. *Optics Express*, 17(7):5075–5082, 2009.

[56] Bjorn Agnarsson, Jennifer Halldorsson, Nina Arnfinnsdottir, Saevar Ingthorsson, Thorarinn Gudjonsson, and Kristjan Leosson. Fabrication of planar polymer waveguides for evanescent-wave sensing in aqueous environments. *Microelectronic Engineering*, 87(1):56–61, 2010.

[57] Björn Agnarsson, Asta B. Jonsdottir, Nina B. Arnfinnsdottir, and Kristjan Leosson. On-chip modulation of evanescent illumination and live-cell imaging with polymer waveguides. *Optics Express*, 19(23):22929–22935, 2011.

[58] Srinivasan Ramachandran, Daniel A. Cohen, Arjan P. Quist, and Ratnesh Lal. High performance, led powered, waveguide based total internal reflection microscopy. *Scientific Reports*, 3:2133, 2013.

[59] B. S. Ahluwalia, A. Z. Subramanian, O. G. Hellesø, N. M. B. Perney, N. P. Sessions, and J. S. Wilkinson. Fabrication of submicrometer high refractive index tantalum pentoxide waveguides for optical propulsion of microparticles. *IEEE Photonics Technology Letters*, 21(19):1408–1410, 2009.

[60] F. Prieto, B. Sep lveda, A. Calle, A. Llobera, C. Dom nguez, A. Abad, A. Montoya, and L. M. Lechuga. An integrated optical interferometric nanodevice based on silicon technology for biosensor applications. *Nanotechnology*, 14(8):907–912, 2003.

[61] Anna Archetti, Evgenii Glushkov, Christian Sieben, Anton Stroganov, Aleksandra Radenovic, and Suliana Manley. Waveguide-paint offers an open platform for large field-of-view super-resolution imaging. *Nature Communications*, 10(1):1267, 2019.

[62] Kyle M. Douglass, Christian Sieben, Anna Archetti, Ambroise Lambert, and Suliana Manley. Super-resolution imaging of multiple cells by optimized flat-field epi-illumination. *Nature Photonics*, 10:705, 2016.

[63] Joran Deschamps, Andreas Rowald, and Jonas Ries. Efficient homogeneous illumination and optical sectioning for quantitative single-molecule localization microscopy. *Optics Express*, 24(24):28080–28090, 2016.

[64] K. K. Sørensen, J. Simon-Santamaria, R. S. McCuskey, and B. Smedsrod. Liver sinusoidal endothelial cells. *Compr Physiol*, 5(4):1751–74, 2015.

[65] Kyle L. Ellefsen, Joseph L. Dynes, and Ian Parker. Spinning-spot shadowless tirf microscopy. *PLOS ONE*, 10(8):e0136055, 2015.

[66] Anne Burgert, Sebastian Letschert, Sören Doose, and Markus Sauer. Artifacts in single-molecule localization microscopy. *Histochemistry and Cell Biology*, 144(2):123–131, 2015.

[67] Niccolò Banterle, Khanh Huy Bui, Edward A. Lemke, and Martin Beck. Fourier ring correlation as a resolution criterion for super-resolution microscopy. *Journal of Structural Biology*, 183(3):363–367, 2013.

[68] Firehun Tsige Dullo, Susan Lindecrantz, Jana Jágerská, Jørn H. Hansen, Magnus Engqvist, Stian Andre Solbø, and Olav Gaute Hellesø. Sensitive on-chip methane detection with a cryptophane-a cladded mach-zehnder interferometer. *Optics Express*, 23(24):31564–31573, 2015.

[69] Christos Markos, Kyriakos Vlachos, and George Kakarantzas. Bending loss and thermo-optic effect of a hybrid pdms/silica photonic crystal fiber. *Optics Express*, 18(23):24344–24351, 2010.

[70] J. H. Schmid, P. Cheben, P. J. Bock, R. Halir, J. Lapointe, S. Janz, A. Delage, A. Densmore, J. Fedeli, T. J. Hall, B. Lamontagne, R. Ma, I. Molina-Fernandez, and D. Xu. Refractive index engineering with subwavelength gratings in silicon microphotonic waveguides. *IEEE Photonics Journal*, 3(3):597–607, 2011.

[71] Ø. I. Helle, B. S. Ahluwalia, and O. G. Hellesø. Optical transport, lifting and trapping of micro-particles by planar waveguides. *Optics Express*, 23(5):6601–6612, 2015.

[72] Nils T. Otterstrom, Ryan O. Behunin, Eric A. Kittlaus, Zheng Wang, and Peter T. Rakich. A silicon brillouin laser. *Science*, 360(6393):1113–1116, 2018.

[73] Alexander L. Gaeta, Michal Lipson, and Tobias J. Kippenberg. Photonic-chip-based frequency combs. *Nature Photonics*, 13(3):158–169, 2019.